

**Single cell landscape of innate and adaptive
immunity in metastatic melanoma treated with
immunotherapy**

by

Ruiwen Fu

S.B., Computer Science and Molecular Biology, Massachusetts Institute
of Technology (2021)

Submitted to the Department of Electrical Engineering and Computer
Science

in partial fulfillment of the requirements for the degree of
Master of Engineering in Computer Science and Molecular Biology
at the

MASSACHUSETTS INSTITUTE OF TECHNOLOGY

May 2022

© Massachusetts Institute of Technology 2022. All rights reserved.

Author
Department of Electrical Engineering and Computer Science
May 6, 2022

Certified by.....
Manolis Kellis
Professor
Thesis Supervisor

Certified by.....
Jiekun Yang
Postdoctoral Fellow
Thesis Supervisor

Accepted by
Katrina LaCurts
Chair, Master of Engineering Thesis Committee

Single cell landscape of innate and adaptive immunity in metastatic melanoma treated with immunotherapy

by

Ruiwen Fu

Submitted to the Department of Electrical Engineering and Computer Science
on May 6, 2022, in partial fulfillment of the
requirements for the degree of
Master of Engineering in Computer Science and Molecular Biology

Abstract

Immune checkpoint inhibitors (ICIs) have revolutionized the care for cancer and extended survival for many patients. While ICIs have shown astonishing clinical benefits, less than 50% of patients experience a durable response. To find better biomarkers for ICI response and understand the diverse cellular players in the tumor, we performed a multi-omic study on a metastatic melanoma cohort with RNA sequencing (39 samples), single cell RNA sequencing (222,351 cells; 39 samples), and single nucleus transposase-accessible chromatin sequencing (45,478 cells; 15 samples). We identified marker genes and functional modules associated with ICI response (e.g. cell-adhesion) and resistance (e.g. oxidative phosphorylation). Through single cell study of ICI resistant tumors, we revealed how cell-adhesion and ribosomal activity changes in the adaptive immunity could reflect tumor-level therapeutic failure. We further characterized the T cell diversity in the tumors and discovered an early activated state and a terminally exhausted T cell state with therapeutic potential. Among the innate immune mediators of tumor microenvironment, we detected a mature dendritic cell state as a powerful predictor of survival and extensively studied its differentiation trajectory, transcriptome signatures, and epigenome landscape. With functional roles in strengthening cancer immunity, many of the molecular and cellular mediators found in this study are relevant to the efficacy of all ICI regimens, and could potentially be extended to targeted inhibitors or other immunotherapies.

Thesis Supervisor: Manolis Kellis
Title: Professor

Thesis Supervisor: Jiekun Yang
Title: Postdoctoral Fellow

Acknowledgments

This study would not have been possible without the guidance and support from many.

I am most indebted to my mentor, Dr. Jiekun Yang, for your irreplaceable guidance and endless encouragement throughout my study. Your insights were invaluable in contriving the research questions and methodology, and I cannot express enough gratitude for the chance to work with you. To my thesis advisor, Prof. Manolis Kellis, I am so grateful for your visionary commentaries, for the opportunity to be part of this amazing lab, and for financial sponsorship of my study.

I would like to offer sincere thanks to my collaborators, Dr. David Liu for constant expert feedback on interpreting results and Dr. Genevieve Boland for providing the clinical samples used in this study. I gratefully recognize Dr. Li-Lun Ho and Dr. Kiki Galani for their effort in data generation and experimental preparation. I also had the pleasure to work with many other members of the Kellis Lab and the Liu Lab, in particular Dr. Ben Lengerich and Emily Robinschek, who have given me helpful comments at meetings. I would like to extend my thanks to Dr. Tom Watkins for his advice on the writing of this thesis.

In addition, I wish to show appreciation to my family, who have never once stopped believing in me and always assured me that all will work out in the end. I am also obliged to mention my friends and housemates for their moral support on my worst days and the house cats and orchids for providing much-needed amusement.

Lastly, I cannot go without expressing the most sincere gratitude to my editor Daniel Stein. You have been my pillar of strength throughout the pandemic and colored my life outside of the darkness of research.

Contents

1	Introduction	15
1.1	Problem statement	15
1.2	Background	16
1.2.1	Etiology and Epidemiology of Melanoma	16
1.2.2	Development of cancer and targeted inhibitors	16
1.2.3	The tumor microenvironment	17
1.2.4	Cancer immunity cycle	19
1.2.5	Immune checkpoint inhibitors reinvigorate T cell effector functions	20
1.2.6	Other immunotherapy approaches for melanoma	23
1.2.7	Sequencing technologies assist cancer research	24
1.3	Study cohort	25
1.4	Study goals	26
2	Molecular and cellular markers of ICI response and resistance	29
2.1	Background	29
2.2	Research approach	30
2.3	Results and Discussions	30
2.3.1	Clinical cohort characteristics	30
2.3.2	Transcriptomic features associated with ICI response and resistance	32
2.3.3	Predictive biomarkers of anti-PD-1 treatment response and resistance	34

2.4	Contributions and future steps	37
2.5	Methods	38
2.5.1	RNA-seq data generation and preprocessing	38
2.5.2	RNA-seq data batch effect correction	38
2.5.3	Identification of differentially expressed genes	39
2.5.4	Gene set enrichment analysis	40
2.5.5	Cell type deconvolution	41
3	Tumor microenvironment evolution during ICI treatment	43
3.1	Background	43
3.2	Research approach	45
3.3	Results and discussions	45
3.3.1	ICIs enhance immune functions in responders	45
3.3.2	ICIs affect ribosomal and metabolic activities in progressive disease	46
3.3.3	Immune infiltration in progressive disease unaffected by ICIs	47
3.3.4	ICIs affect CD8+ T cell activities in progressive disease	49
3.4	Contributions and limitations	52
3.5	Methods	53
3.5.1	Identification of differentially expressed genes and gene sets from RNA-seq	53
3.5.2	scRNA-seq data generation and preprocessing	54
3.5.3	scRNA-seq data dimensionality reduction, cell-type identification, and clustering	54
3.5.4	scRNA-seq integration	55
3.5.5	Identification of differentially expressed genes and gene sets from scRNA-seq	55
4	Diversity of T cells in the tumor microenvironment	57
4.1	Background	58
4.2	Research approach	59

4.3	Results and discussions	60
4.3.1	Diversity of tumor-infiltrating CD4+ T cells	60
4.3.2	Inference of CD4+ T cell differentiation trajectory	63
4.3.3	Tumor-infiltrating CD8+ T cells show universal exhaustion	64
4.3.4	Inference of CD8+ T cell exhaustion trajectory	69
4.3.5	Relating T cell composition to clinical information	71
4.4	Contributions	72
4.5	Limitations	73
4.6	Methods	74
4.6.1	Cell type assignment	74
4.6.2	Identification of cluster signature genes and pathways	74
4.6.3	Trajectory inference	75
4.6.4	Terminal state identification and fate probability estimation	78
5	Conventional dendritic cells bridge adaptive and innate cancer im-	
	munity	81
5.1	Background	82
5.2	Research approach	83
5.3	Results and discussions	84
5.3.1	scRNA-seq reveals cDC3 transcriptomic profile	84
5.3.2	cDC3 abundance predicts progression-free survival	86
5.3.3	Differentiation trajectory of cDC3 state	86
5.3.4	NF- κ B and KLF3 transcription factors regulate cDC3 state	88
5.3.5	cDC3 influences T cell homing and activation	89
5.3.6	snATAC-seq evaluates open chromatin regions and motifs en-	
	riched in cDC3	92
5.4	Contributions and future steps	93
5.5	Methods	95
5.5.1	Identification and scRNA characterization of cDC3s	95
5.5.2	Trajectory and fate-driver gene inference	95

5.5.3	Cell-cell-interaction prediction	95
5.5.4	Regulatory network inference with <i>SCENIC</i>	96
5.5.5	snATAC-seq data generation and preprocessing	96
5.5.6	Integration of snATAC-seq and scRNA-seq data	97
5.5.7	Differentially accessible peaks and motif enrichment analysis .	98
6	Conclusion	99
6.1	Summary of research contributions	99
6.2	Future directions	100
6.3	Concluding words	101
A	Supplementary figures	103

List of Figures

1-1	Clinical characteristics of metastatic melanoma cohort.	26
2-1	Clinical characteristics of RNA-seq cohort.	31
2-2	Expression of checkpoint molecule genes in PD and R samples measured by RNA-seq.	32
2-3	Volcano plot of differentially expressed genes between ICIs treated PD and R samples.	33
2-4	Differentially expressed gene sets between ICI-treated PD and R samples.	34
2-5	Differentially expressed genes between pre-anti-PD-1 treated PD and R samples.	35
2-6	Selected differentially expressed gene sets enriched in pre-anti-PD-1 treated R samples.	36
2-7	Cell type deconvolution of RNA-seq data comparing pre-anti-PD-1 treated PD and R samples.	37
3-1	Differentially enriched gene sets in pre- and on-ICI responders.	46
3-2	Differentially enriched gene sets in pre- and on-treatment progression diseases.	47
3-3	Changes in deconvolved tumor composition during ICI treatment.	48
3-4	Clinical characteristics of pre- and on-ICI therapy progressive disease scRNA-seq samples.	48
3-5	Immune infiltration measured by scRNA-seq.	49
3-6	Volcano plot of differentially expressed genes in pre- and on-ICIs CD8+ T cells.	50

3-7	Selected differentially expressed gene sets in pre- and on-ICIs CD8+ T cells.	51
3-8	Molecular features of pre- and on-ICI CD8+ T cells.	52
4-1	Clinical characteristics of scRNA-seq cohort.	60
4-2	Identification of CD4+ T cell subsets.	61
4-3	Heatmap of top differentially expressed genes across CD4+ T cell subpopulations.	62
4-4	Diffusion map of CD4+ T cells.	63
4-5	Pseudotime inference of CD4+ T cells.	64
4-6	Identification of CD4+ T cell macrostates by <i>CytoTrace</i>	65
4-7	CD4+ T cell trajectory inference through RNA velocity.	65
4-8	Identification of CD8+ T cell subsets.	66
4-9	Heatmap of top differentially expressed genes across CD8+ T cell subpopulations.	68
4-10	Pseudotime inference of CD8+ T cells.	69
4-11	Differentiation trajectory of CD8+ T cells.	70
4-12	T cell compositions across treatment states.	71
4-13	Association of progression-free survival and T cell compositions.	72
5-1	Identification of myeloid cell subsets.	84
5-2	Transcriptomic characterization of cDC3 in melanoma.	85
5-3	Developmental trajectory of cDC subpopulations inferred by <i>CytoTrace</i>	87
5-4	Association of progression-free survival and cDC3 frequency.	88
5-5	Scatter plot of cDC3 regulon specificity scores inferred by <i>SCENIC</i>	89
5-6	Scatter plot of cDC3 and T cell abundances in on-treatment melanoma.	90
5-7	cDC-T cell interactions predicted by <i>CellPhoneDB</i>	90
5-8	T cell-cDC interactions predicted by <i>CellPhoneDB</i>	91
5-9	Integration of snATAC-seq and scRNA-seq detected cDCs.	92
5-10	Chromatin accessibility profiles of cDC3 in melanoma.	93
5-11	Sequence logo plot of selected motifs enriched in cDC3.	94

A-1	Survival plot of response groups.	103
A-2	Quality control of 39 RNA-seq samples.	104
A-3	Heatmap of differentially expressed genes between ICIs treated PD and R samples.	105
A-3	Heatmap of differentially expressed genes between ICIs treated PD and R samples.	106
A-4	Enrichment map of differentially expressed functional modules between ICIs treated PD and R samples.	107
A-5	Enrichment map of differentially expressed functional modules between pre-anti-PD-1 treated PD and R samples.	108
A-6	Linear regression of tumor purity measured by whole exome sequencing (WES) and deconvolved malignant cell fraction in RNA-seq.	109
A-7	Integration of 11 scRNA-seq samples.	110
A-8	Heatmap of differentially expressed genes in pre- and on-ICIs CD8+ T cells.	111
A-9	Integration of 39 scRNA-seq samples.	112
A-10	Integration of CD4+ T cells from 34 scRNA-seq samples.	113
A-11	Dot plot of top gene sets enriched in CD4+ T cell subpopulations.	114
A-12	UMAP feature plot of selected driver genes of CD4+ T cell terminal state 2 fate inferred by <i>CytoTrace</i>	115
A-13	Integration of CD8+ T cells from 35 scRNA-seq samples.	116
A-14	Dot plot of top gene sets enriched in CD8+ T cell subpopulations.	117
A-15	Integration of myeloid cells from 39 scRNA-seq samples.	118
A-16	Integration of cDCs from 38 scRNA-seq samples.	119
A-17	UMAP feature plot of selected cDC3-fate driver genes inferred by <i>CytoTrace</i>	120
A-18	Assignment of cell types in snATAC-seq dataset.	121

Chapter 1

Introduction

1.1 Problem statement

Almost all chemotherapies reduce cancer growth by killing cells undergoing DNA replication or mitotic division. As a result, chemotherapy has high toxicity from killing normal cells in addition to cancer cells. In the late 1990s, scientists invented a new class of therapy, targeted inhibitors, which are specifically aimed at proteins produced or affected by gene mutations that allow cancer cells to grow, divide, and spread [1]. Although targeted inhibitors attack the specific mutated processes, tumors can often evolve to bypass the drug target and develop resistance within a short amount of time [2].

Starting in the 2010s, the first immune checkpoint inhibitors (ICIs) were highly successful in clinical trials, achieving 20 to 50 months of progression-free survival, and soon became the new standard of care for some metastatic cancers [3]. As a mutation-agnostic treatment, ICIs are effective in reinvigorating patients' own immunity to eliminate cancer. While the efficacy of ICIs is undeniable, only a fraction of patients experience a durable response and little is known on why ICIs fail in some patients [4]. Therefore, there is an intense interest in understanding response and resistance to ICIs treatment, both to enable rational guidelines for treatment decisions (e.g. whether patients should receive ICI therapy, or which regimen to use) and to uncover potential targets for the next generation of cancer immunotherapies. Given the high

complexity and heterogeneity in each tumor, it is critical to recognize the therapeutic effects on each individual cellular mediator and their interactions.

In this thesis, we used melanoma as an example to study the immune mediators that govern ICI response at the tumor-level. With many immune mediators and their functions universally observed across cancers, we hope to uncover key properties and hallmarks that can be extended to other cancer types.

1.2 Background

1.2.1 Etiology and Epidemiology of Melanoma

Melanoma, a malignancy that begins in the pigment-producing melanocytes, is by far the most serious type of skin cancer. The American Cancer Society predicted 106,110 new diagnoses of melanoma in the United States in 2021 alone, a number that has been growing rapidly over the past decades [5]. The average age of melanoma diagnosis is 65, since it is often, but not always, caused by accumulation of prolonged exposure to UV radiation. Nevertheless, it is one of the most common cancers in young adults due to the practice of indoor tanning [5]. Melanoma can develop anywhere on the surface of the body. Depending on the primary location of malignancy, melanoma can be classified as cutaneous (skin), acral (on palms, soles, or under nails), mucosal (nasal cavity, mouth, GI tract, etc.), and uveal (eyes) [6]. If not diagnosed and treated in early stages, melanoma can easily metastasize to other organs, making it the most dangerous skin malignancy [5].

1.2.2 Development of cancer and targeted inhibitors

Despite the remarkable genetic and physiological diversity across cancers, all cancer cells acquire the capacity of sustained proliferation [7]. Although cancer cells can sustain proliferation through several mechanisms, nearly 40% of melanomas acquire activated mutations affecting proto-oncogene B-Raf (BRAF) [7]. The activating BRAF mutations result in constitutive signaling of the RAS-RAF-MEK-ERK

pathway, which promotes mitotic division [2]. Two other proteins in the RAS-RAF-MEK-ERK pathway, mitogen-activated protein kinase kinase (MEK) and type III transmembrane receptor tyrosine kinase (c-KIT), are also amplified or mutated at moderate frequencies in melanoma cells [1]. To put a stop to the continuing proliferation of cancer cells, molecularly targeting agents of BRAF, MEK, and c-KIT proteins (targeted inhibitors) have been developed. While effective in inhibiting proliferation acquired through these specific mutations, targeted inhibitors are not applicable to cancers which do not harbor the specific mutations they are designed to target. Additionally, cancers that are treated with targeted inhibitors can quickly develop resistance by evolving new mechanisms to continue proliferation. Therefore, studies are actively researching strategies that combine targeted inhibitors with other treatments to extend their anti-tumor effects [8].

1.2.3 The tumor microenvironment

Although the field of cancer biology was first established on altered properties of cancer cells, tumors are far more complex than a mere collection of malignant cells. Cancer cells constantly interact with the surrounding ecosystem of extracellular matrix, blood vessels, immune and other cells, which are collectively referred to as the tumor microenvironment [9]. Recent studies recognize tumor and the microenvironment more as an organ, whose complexity can be no less than that of normal healthy tissue [7]. For a more accurate understanding of the tumor microenvironment, each specialized cell type and their contribution to the tumor should be studied in detail.

Malignant cells in the tumor microenvironment

Cancer cells are the roots of the disease; they start the tumor and define the cancer genetics; they are responsible for driving disease progression and metastasis [10]. As a result of combined hyperproliferation and genome instability, a tumor often contains several clonal subpopulations of malignant cells which lead to a high intratumoral heterogeneity. Due to the genetic and phenotypic heterogeneity within a tumor,

therapies targeting a specific mutation often fail to eradicate all cancer cells and may even act as a selective pressure to encourage diversification [11].

Stromal cells in the tumor microenvironment

Stromal cells constitute the connective tissue that provide structural support and deliver nutrients to the tumor [12]. Endothelial cells form the tumor-associated vasculature and construct blood vessels to deliver oxygen and nutrients to the tumor and lymphatic vessels for metastasis and immune cell infiltration. Cancer-associated fibroblasts (CAFs) are heterogeneous stromal cell populations in solid tumors that facilitate cancer progression by secreting growth factors, remodeling the extracellular matrix (ECM), promoting angiogenesis, and inducing tumor-promoting inflammation [7]. Studies have found CAFs assist cancer cells in immune escape by secreting cytokines to recruit and facilitate the differentiation of pro-inflammatory immune cells [12]. CAFs are also able to suppress the cancer-killing functions of cytotoxic T cells by inducing their checkpoint molecule expressions (e.g. PD-1, CTLA-4, LAG-3) [13].

Innate immune cells in the tumor microenvironment

Macrophages account for the majority of the innate immune cells in the tumor microenvironment. Macrophages have key roles in infection response and tissue repair, and can engulf cancer cells, induce necrosis, and prime T cells by presenting tumor antigen. On the other hand, macrophages can also promote tumor growth by secreting immunosuppressive cytokines, promoting epithelial–mesenchymal transition, and stimulating angiogenesis and lymphangiogenesis. Studies are actively researching the anti-tumor and pro-tumor spectrum of macrophage states [14]. Natural killer ((NK) cells are innate immune cells with potent cytolytic activity. When detecting cancer cells down-regulating major histocompatibility complex I (MHC I) to avoid T cell surveillance, NK cells release cytotoxic perforin and granzymes to eliminate cancer cells [14].

Conventional dendritic cells (cDCs) are the primary antigen-presenting cells (APCs) that bridge the innate and adaptive immunity. Present in almost all tissues of the

body, cDCs patrol the local environment by sampling antigens. While carrying the sampled antigen, cDCs migrate through afferent lymph vessels to the draining lymph nodes (LNs) [15]. At the T-cell zone of LNs, they present the antigen to naive T cells, which proliferate and specialize to antigen-specific T cells after receiving this signal [16]. In tumor tissues, cDCs present tumor antigen to T cells, which can result in antigen tolerance or effector T cell priming. Additionally, tumor-infiltrating cDCs can locally license the T cells for their anti-tumor immunity [16]. Although essential to cancer immunity, cDC involvement in cancer is understudied due to their low abundance in tumors.

Adaptive immune cells in the tumor microenvironment

T cells are the key conductors and effectors of adaptive immunity. CD8⁺ T cells are the leading anti-tumor cells that recognize cancer cells through T cell receptors (TCRs) and directly destroy them. CD4⁺ T helper cells assist cancer-killing through presentation of tumor antigens and secrete cytokines, such as IL-2, to promote anti-tumor activities in CD8⁺ T cells, NK cells, and macrophages. On the other hand, regulatory CD4⁺ T cells (Tregs) express immunosuppressive cytokines and immune checkpoint ligands (e.g. PD-L1) to halt the activation and cytotoxicity of other immune cells. B cells mediate humoral immunity through production of high-affinity antibodies. Although antibody production is hypothesized to have roles in assisting cancer cell detection and activating myeloid-derived suppressor cells (MDSCs), the contribution of B cells in cancer progression is not well understood [14].

1.2.4 Cancer immunity cycle

Human cells and tissues are constantly monitored by the immune system, which recognizes and eliminates the majority of emerging cancer cells. The cancer-killing immune response takes place over a series of events [17]. To start, neoantigens produced by cancer cells, often a product of non-synonymous somatic mutations, are captured by APCs, including DCs. At the signal of pro-inflammatory cytokines or

other cellular content released by the dying cancer cell, APCs present the captured neoantigens on MHC I or MHC II. At the lymph nodes, APCs prime the cytotoxic effector T cells against cancer-specific neoantigens. The activated T cells then traffic to the tumor site and recognize cancer cells through TCR interaction with cancer cell peptide-MHC I (p-MHC I). Killing of the cancer cells releases additional neoantigens and immunogenic signals to strengthen this cancer immunity cycle [17].

However, in cancer patients, the immunological monitoring could be obstructed in several ways. HIV patients, organ transplant recipients, and other pharmacologically immunosuppressed patients are often deficient in the key cancer-killing cells, including T cells, NK cells, or B cells [7]. In immunocompetent patients, the tumors may prevent immune cells from infiltrating or may present little neoantigen to avoid immune surveillance [18]. Cancer cells may actively debilitate infiltrating T and NK cells by inducing immune checkpoint molecules or secreting immunosuppressive factors such as TGF- β . Other mechanisms of suppressing the cytotoxic T cells include recruitment of immunosuppressive cells, such as Tregs and MDSCs.

1.2.5 Immune checkpoint inhibitors reinvigorate T cell effector functions

The development of immune checkpoint inhibitors has been transforming clinical cancer care with their impressive responses in several malignancies, including melanoma, lung cancer, head and neck cancer, and Hodgkin lymphoma [19]. In melanoma, the approved ICIs include anti-CTLA-4 (ipilimumab), anti-PD-1 (nivolumab, pembrolizumab), anti-PD-L1 (atezolizumab), and combination anti-PD-1/CTLA-4 regimens (nivolumab-ipilimumab) [20]. During the writing of this thesis, a new class of ICI, anti-LAG3, has just received FDA approval for stage III and IV melanoma [21]. These checkpoint inhibitors block the natural ‘checkpoints’ in T cells that put the brake on the cancer-killing effector functions.

Without any highly sensitive biomarkers for ICI response prediction, the current practice of therapy assignment for advanced melanoma patients is based on clinical

factors such as volume, site of malignancy, and BRAF mutation. For patients with high risk of recurrent melanoma after surgical resection, PD-1 inhibitors are now recognized as a standard of care adjuvant therapy [22]. Although considered to be less toxic than the conventional therapies and safe to use in patients with HIV, viral hepatitis, or organ transplants, ICIs can induce immune-related adverse events that mimic classic autoimmune diseases [23].

T cell activation is modulated by several co-stimulatory and co-inhibitory receptors, which are the targets of ICI therapies. The process of T cell activation starts with TCR binding to the specific p-MHC on APCs, including DCs [22]. In addition to the presence of p-MHC, T cell co-stimulatory receptor CD28 is also required for full T-cell activation. Through interaction with the B7 family ligands on APCs, CD28 promotes survival and proliferation in T-cells. Accompanying the co-stimulatory receptors are a number of co-inhibitory receptors, commonly referred to as immune checkpoints receptors (e.g. CTLA-4, PD-1, LAG-3, TIGIT), that turn off T cell responses to prevent destructive inflammation.

Checkpoint inhibitor of the CTLA-4 pathway

Cytotoxic T-lymphocyte-associated protein-4 (CTLA-4) was the first checkpoint receptor to be discovered and its discovery was awarded the 2018 Nobel Prize in Medicine [24]. Expressed on the surface of activated T cells, CTLA-4 abducts B7 ligands with a high binding affinity to prevent CD28-B7 interaction. Consequently, CTLA-4 binding can lead to attenuation of co-stimulatory signaling and halt T-cell-mediated anti-tumor immune responses. To combat this, CTLA-4-blocking antibodies were designed to remove the CTLA-4 inhibitory signal and restore T-cell immunity to eradicate tumors. In 2011, Ipilimumab, a fully human monoclonal IgG1 antibody, became the first FDA approved ICI and is currently still the only approved CTLA-4 targeting ICI for melanoma [22].

Checkpoint inhibitor of the PD-1/PD-L1 axis

Programmed cell death protein 1 (PD-1) is another extensively studied immune checkpoint expressed on T cells. PD-1 expression on T cells is induced by prolonged stimulation, often in the condition of chronic viral infection or cancer [25]. Unlike CTLA-4 interfering with the CD28-B7 interaction, PD-1 plays a role in a later stage of TCR signaling. The action of PD-1 starts with binding to one of its ligands: PD-L1, which is constitutively expressed on various immune cells, some endothelial cells, and many tumor cells, and PD-L2, expressed on APCs and occasionally induced in tumor cells [22]. Binding of PD-1 results in recruiting domain-containing phosphatase 1 and 2 (SHP1, SHP2) to dephosphorylate the TCR complex [18]. In this way PD-1 signaling inhibits T cell proliferation, survival, cytokine secretion, and ultimately “exhausts” the T cells from carrying out their effector function. To restore the anti-tumor function of exhausted T cells, two PD-1 blocking antibodies, nivolumab and pembrolizumab, have received FDA approval [22]. Along the same axis of action, a PD-L1 blockade, atezolizumab, also received FDA approval for metastatic melanoma patients [26].

Combinatorial blockade of CTLA-4 and PD-1 checkpoints

Because CTLA-4 and PD-1 induce inhibitory signals in T cells through different mechanisms of action, it was hypothesized that blocking both signals could lead to a higher chance of reversing the exhausted T cell phenotype. Thus, the combination of CTLA-4 and PD-1 inhibitors became a rational treatment approach. The clinical efficacy of these ICI regimens in previously untreated melanoma patients was compared in the Checkmate 067 clinical trial [27]. The median overall survival (OS) was 19.9 months in the anti-CTLA-4 arm, 36.9 months in the anti-PD-1 arm, and more than 60 months in the combination arm. The objective response rate was 19.0%, 43.7%, and 57.6%, respectively. Although the combination therapy is higher in clinical efficacy, the stronger regimen is also more likely to lead to grade 3 and 4 adverse events, which usually can be resolved by delaying the treatment or systemic corticosteroids administration [28].

1.2.6 Other immunotherapy approaches for melanoma

Melanoma is a highly immunogenic cancer due to the high burden of UV induced mutations, making it suitable for immunotherapies. Besides ICIs, several other immunotherapy approaches are currently used in the clinics or undergoing clinical trials.

Known for its role in T cell expansion, cytokine IL-2 was among the first FDA (1998) approved immune-based therapies for metastatic melanoma [29]. Although the response rate of IL-2 treatment alone was no higher than 20%, it is still included in trials in combination with other therapies.

Talimogene laherparepvec (T-VEC), a genetically modified herpes simplex virus, was the first oncolytic virus treatment for melanoma [22]. This nonpathogenic virus is injected directly into the melanoma nodule and only replicates in and lyses melanoma cells. The released tumor-specific antigens are picked up by APCs to activate the T cell anti-tumor responses.

Melanoma vaccines have also been designed to elicit the cancer-killing functions of the adaptive immune system. Epitopes of gp100, a glycoprotein expressed mostly in melanoma cells and melanocytes, is an appealing candidate for off-the-shelf melanoma vaccines [29]. Studies are actively researching the gp100 peptide vaccine as a monotherapy or in combination with IL-2 and other immunotherapies.

Chimeric antigen receptor (CAR)-T cell immunotherapy approaches have gained impressive success in hematological malignancies. While CAR-T cell therapies are not nearly as successful in solid tumors, including melanoma, engineering innovations are made to enable better CAR-T cell migration to tumor sites and to maintain effector functions in the immunosuppressive tumor microenvironment [30]. Adoptive T cell transfer therapy approach involves T cell collection from a patient's tumor or blood, potency selection and *in vitro* expansion of T cells, and infusion of lab-grown cells to the patient. Although not yet approved by the FDA, the enthusiasm of T cell transfer therapy for melanoma is reflected by the numerous on-going clinical trials [30].

1.2.7 Sequencing technologies assist cancer research

RNA-sequencing

Although only developed less than 20 years ago, RNA-sequencing (RNA-seq) has become one of the most powerful tools in understanding complex biological conditions at the molecular level. With the ability to measure expressions of more than 20,000 genes at a time, bulk RNA-seq captures a detailed snapshot of the entire tumor landscape [31]. One of the most common applications of RNA-seq is differential gene expression analysis, where two conditions are compared to find potential biomarkers for cancer diagnosis or treatment response. When co-extracted with Whole Exome Sequencing (WES), RNA-seq can also be used to detect gene fusions and predict neoantigens. In longitudinal studies, RNA-seq is used to monitor the tumor's evolution or reaction to treatments. Beyond bioinformatic analyses, machine learning methods are also used to unravel the richness of transcriptomic information RNA-seq has to offer. Methods from random forests to meta-learning to contextualized learning have been used on RNA-seq data for diagnosis, disease subtype classification, or treatment outcome prediction [32, 33].

Single cell RNA-sequencing

While bulk RNA-seq can detect all RNA transcripts in one mixture, the differences between cells are lost. As we have reviewed in the previous section, tumor tissue is an extremely heterogeneous composition of malignant cells, T cells, macrophages, endothelial cells, and many more cell types. On top of the various cell types, heterogeneity also accumulates as the malignant cells evolve and gain mutations. Single-cell RNA sequencing (scRNA-seq) unfolds the intratumoral heterogeneity by profiling the tumor transcriptome at the single-cell resolution. Since the technology became commercially available in 2015, an increasingly large number of cells can be processed in one experiment, allowing not only the study of multiple cell types at a time but also the discovery of rare cell types [34]. With tens of thousands of cells sequenced per tumor, scRNA-seq also allows more computational exercises, including inference

on copy number variation, developmental trajectory, and gene regulatory networks [35]. Even though the technology and supporting computational methods were only developed less than a decade ago, studies have already used scRNA-seq to find gene programs associated with phenotype switching, observe tumor-infiltrating T cell diversity, understand the mechanism of T cell exclusion, and much more [36, 37, 38].

Assay for Transposase-Accessible Chromatin sequencing

Transcription of mRNA is enabled by the concerted interactions of transcription factors (TFs) binding to genomic sites such as gene promoters, enhancers, and other distal regulatory elements. To ensure tight regulation on RNA expression, regions of chromatin usually remain in the ‘closed’ conformation and become accessible, or ‘open’, prior to transcription. With the exception of a few pioneer TFs that can bind to less accessible chromatin regions, most TFs can only bind to accessible nuclear DNA [39]. Therefore, understanding transcriptional regulation in the tumor entails profiling of the chromatin landscape. Assay for Transposase-Accessible Chromatin sequencing (ATAC-seq) using hyperactive Tn5 transposase was developed to identify open chromatin regions where TFs can bind [34]. Computational methods have been developed for single cell and single nucleus ATAC-seq (snATAC-seq) to find differential accessibility regions, infer binding motifs, predict genomic interactions, and perform pseudotime analysis of specific cell type or states [40, 41]. When combined with scRNA-seq, scATAC-seq data can relate the TF-targeted genomic loci to their transcript abundance [39]. Integration of the two modalities can further reveal regulatory layers that cannot be detected in either transcriptome or epigenome alone.

1.3 Study cohort

The melanoma samples used in this study were provided by G.B. We restricted the study cohort to annotated metastatic tumors that received ICIs, targeted inhibitors, other immune therapies, or a combination of these regimens as the primary treatment. After stringent quality control, 67 samples remained in the cohort, including 39 RNA-

seq samples, 39 scRNA-seq samples, and 15 snATAC-seq samples (with matched scRNA-seq). Collected from 45 patients, 66% samples were cutaneous melanoma with 4 mucosal, 3 uveal, 2 acral, and 2 of unknown origin. 64% samples in the cohort were skin metastases, and the rest in lymph, small intestine, brain, and other tissues. The biopsy time and length of progression-free survival (PFS) with respect to the treatments were also recorded. Additional clinical information, including age, sex, treatment state, and prior therapy history, are shown in Figure 1-1.

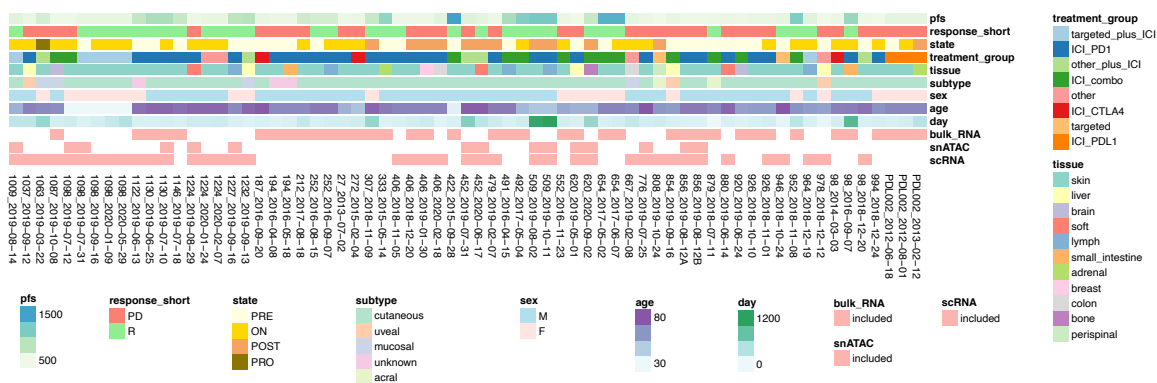


Figure 1-1: Clinical characteristics of metastatic melanoma cohort. Progression-free survival in days. Biopsy day measured in reference to treatment start date. Biopsy state assigned in reference to start of treatment. PRO, post-progression. Tumor response group assigned by RECIST criteria. PD, progressive disease; R, response. Melanoma subtype identified by primary tumor location. Tissue indicates metastasis location. Bulk RNA-seq n = 39; scRNA-seq n = 39; snATAC-seq n = 15.

Unlike clinical studies that tightly regulate sample enrollment to ensure homogeneity in disease manifestation and therapy course, the cohort in this study is highly heterogeneous in melanoma subtype, metastasis site, and treatment group and treatment state. We hope to leverage the cohort heterogeneity through computational methods and discover robust biomarkers and mechanisms that are shared universally across melanomas.

1.4 Study goals

While the success of ICIs is indisputable, only a fraction of patients experience a durable response [25]. The field has been spending a large effort in finding predictive

biomarkers to identify patients who are likely to benefit from ICI treatment and avoid the unnecessary risk of adverse events for patients who are not likely to benefit from ICIs. To extend our understanding of ICI treatment outcome, this thesis has four main goals:

1. to identify marker genes, functional modules, and cell types associated with ICI response and resistance (Chapter 2),
2. to elucidate how ICIs influence progressive disease at the tumor and cellular level (Chapter 3),
3. to characterize the diversity of adaptive immune mediators in the tumor and how each relates to therapeutic outcome (Chapter 4),
4. and to establish the clinical significance of innate immune mediators and uncover their interactions with adaptive immune mediators (Chapter 5).

Moreover, advancement on these fronts could shine a light on new directions for therapy design to achieve higher efficacy or to benefit patients who do not respond to the currently available ICI regimens.

Chapter 2

Molecular and cellular markers of ICI response and resistance

Past melanoma studies on ICI therapies have found higher PD-L1 expression in responding tumors, reflecting their vulnerability to PD-1/PD-L1 blockade [42]. In fact, immunohistochemistry (IHC) staining of PD-L1 is a FDA approved companion diagnostic for anti-PD1 therapy for NSCLC patients. However, PD-L1 status should neither be a necessary or sufficient biomarker for therapeutic decisions in the clinic, as patients with low to no detectable PD-L1 expression may still experience durable clinical benefit [43]. Therefore, in this chapter, we aim to identify a more comprehensive transcriptomic profile of ICI responders and progressors through differential gene expression, gene set enrichment, and cell type abundance analyses.

2.1 Background

Differential analysis of RNA-seq data has been used to unveil global tumor and microenvironment features associated with ICI response or resistance. In a pre-anti-PD1 treated melanoma study, Liu et al. found responder tumors had higher expression of MHC I and II associated HLA genes and enrichment in several immune related pathways, including interferon- γ (IFN- γ) response, allograft rejection, complement, inflammatory response, IL-6/JAK/STAT3 [42]. Deconvolution and immunohistochem-

istry analysis have also found that anti-PD 1 response was associated with higher levels of CD8+ T and NK cells [43]. In fact, studies have repeatedly found gene modules reflecting immune-checkpoint molecule (e.g. PD-L1, CTLA-4), antigen presentation, IFN- γ signaling, and T lymphocyte infiltration enriched in responders, but very few signatures in non-responders have been discovered [42, 44]. The difficulty in finding resistance markers can be partially attributed to the heterogeneity among resistant tumors, with potentially each individual tumor evolving different mechanisms to evade the effects of treatment. Moreover, the identified signatures can often be unique to the original cohort and fail to generalize in larger studies [43]. The failure to recapitulate a signature can be caused by the lack of robust sample size in the discovery cohort, compounded with failure to account for covariates in the validation study [43].

2.2 Research approach

We performed bulk RNA-seq analysis on 39 metastatic melanoma tumors including 22 responders and 17 with progressive disease (progressors). While accounting for the clinical heterogeneity among the samples, we applied three state-of-the-art methods (*DEseq2* [45], *EdgeR* [46], and *Limma-Voom* [47]) for the task of differential expression analysis, and summarized the gene statistics using gene set enrichment analysis (GSEA) [48]. To relate the differential biomarkers to tumor composition, we used *CIBERSORTx* to deconvolve the cell type abundances [49]. Lastly, we repeated the analyses on the pre-anti-PD-1 treated samples in order to find biomarkers that are specific for predicting anti-PD-1 treatment outcome.

2.3 Results and Discussions

2.3.1 Clinical cohort characteristics

We performed bulk RNA-seq analysis on 39 metastatic melanoma samples treated with anti-CTLA-4 (n=3, 8%), anti-PD-1 (n=17, 43%), anti-PD-L1 (n=3, 8%), or

combination therapy (n=16, 41%; Figure 2-1). With the help of clinical experts, we stratified the samples into responders (R; n = 22) and progressive disease (PD; n=17) groups according to the RECIST criteria [50]. Using a Kaplan-Meier estimator, we confirmed the PD and R labels accurately reflect PFS (Figure A-1).

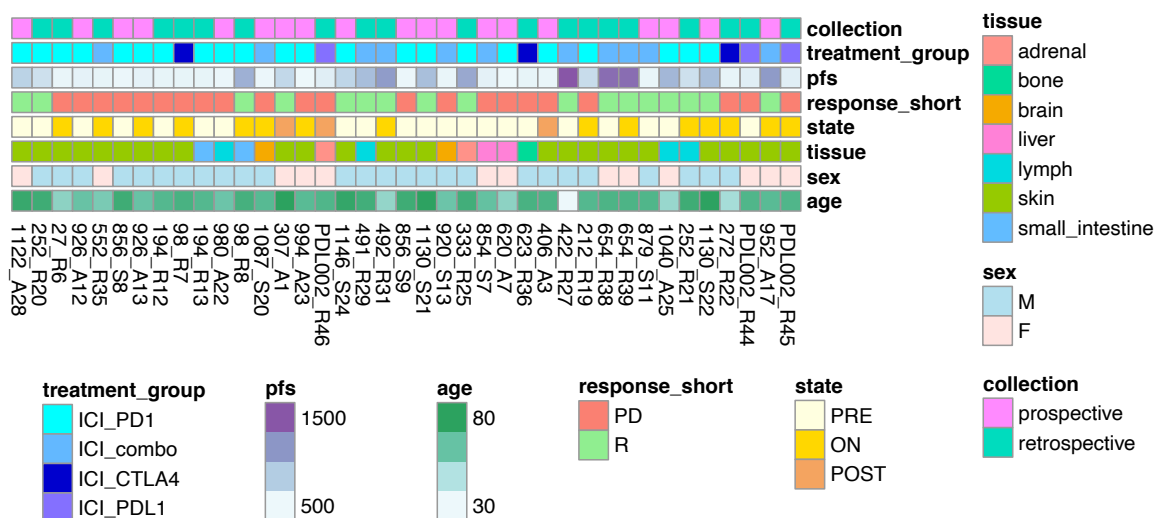


Figure 2-1: Clinical characteristics of RNA-seq cohort. Progression free survival in days. Biopsy state assigned in reference to start of treatment. Tumor response group assigned by RECIST criteria. PD, progressive disease; R, response. Tissue indicates metastasis location. n = 39.

Prompted by previous studies, we looked into the expression level of immune-checkpoint molecules PD-1 (PDCD1), PD-L1 (CD274), PD-L2 (PDCD1LG2), and CTLA-4, and found no significant association with response or PFS (Figure 2-2). Other clinical information is detailed in Figure 2-1. As demonstrated in the principal component analysis analysis, *ComBat-seq* was able to successfully correct the batch difference between samples in retrospective (formalin-fixed paraffin-embedded; n=20) and prospective (frozen; n=19) collection (Figure A-2A). We further ensured the samples had similar expression levels, as measured by $\log(CPM)$ (Figure A-2C).

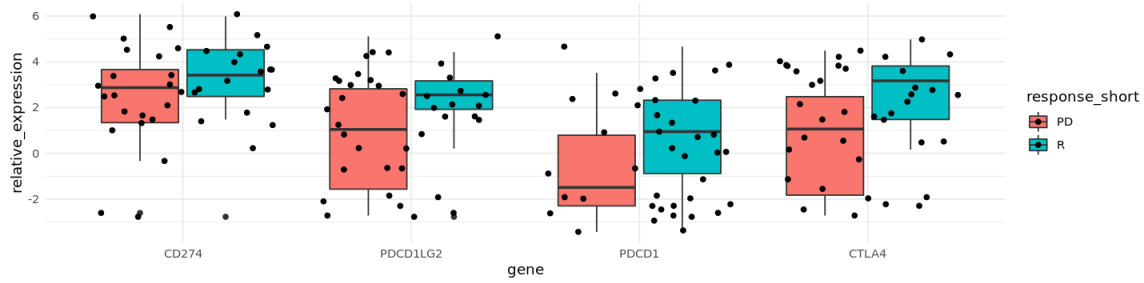


Figure 2-2: Expression of checkpoint molecule genes in PD and R samples measured by RNA-seq. Each data point is shown in boxplots, in addition to median and IQR.

2.3.2 Transcriptomic features associated with ICI response and resistance

We applied three state-of-the-art methods, *DEseq2* [45], *EdgeR* [46], and *Limma-Voom* [47], for the differential expression analysis between responder and progressor samples, with consideration of treatment state, treatment group, sex, tissue, and age as covariates. While the results produced by different methods were comparable, we found *Limma-Voom* as the more suitable method for the complexity of our hypothesis. We found that with the heterogeneity of this clinical cohort, *DEseq2* was overly sensitive to outlier data points and *EdgeR* was marginally underpowered compared to *Limma-Voom* (result not shown) [51].

Immune activities enriched in ICI responders

We found many gene whose expression were significantly associated with response to be involved in complement (e.g. C1R, MSR1), innate immunity (e.g. TLR1, FCGR3A), and antigen presentation (e.g. HLA-DRB5; Figure 2-3; Figure A-3), agreeing with previous literatures [42]. From gene set enrichment analysis of responders, we also observed significant enrichment of many immune cell activities, including T-cell and B-cell receptor signaling, NK cell cytotoxicity, Fc gamma receptor phagocytosis (Figure 2-4A). Additionally, we found several responder-enriched genes (e.g. ADAM19, CLEC2D, CDH11) with functions in immune cell-cell interaction. Interestingly, a few genes involved in tumor growth signaling (AXL, LTBP2, TGFB3)

again conferred a survival advantage for the tumor cells in the condition of immune checkpoint inhibitors therapy. In Chapter 3, we revisited the implications of mitochondrial activity and oxidative phosphorylation in resistant tumors through the lens of scRNA-seq.

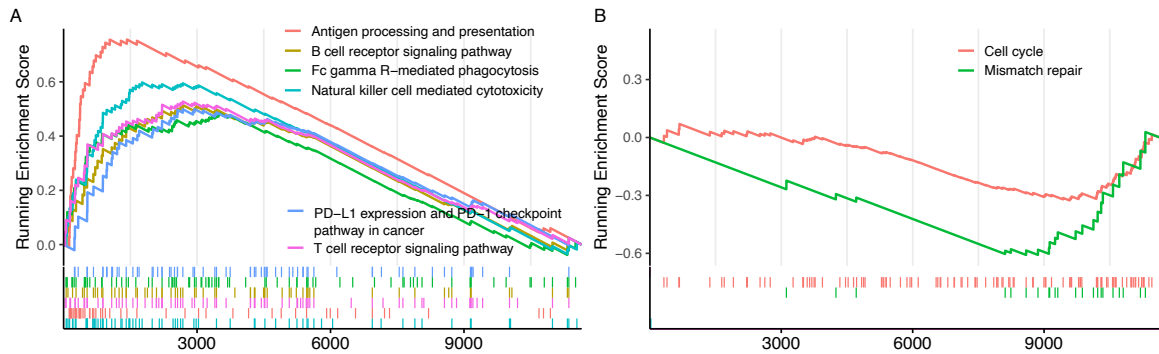


Figure 2-4: Differentially expressed gene sets between ICIs treated PD and R samples. A. Enrichment plot showing selected gene sets enriched in R. B. Enrichment plot showing selected gene sets enriched in PD. Top panel shows running enrichment score, bottom panel shows gene rank in the gene set. Adjusted $p < 0.01$.

2.3.3 Predictive biomarkers of anti-PD-1 treatment response and resistance

anti-PD-1-specific response predictors

To find biomarkers with clinical value specific to anti-PD-1 response, we focused on the RNA-seq analysis on 13 pre-anti-PD-1 treated samples (7 PD, 6 R). While most responder DEGs were also observed in the expanded cohort ($n=39$), we observed a few commonly studied genes specific to the pre-anti-PD-1 responders, including IL18, CXCL9, and CD226 (Figure 2-5). CXCL9, a predominantly macrophage derived T-cell recruiting chemokine, has been repeatedly reported as essential for CD8⁺ T-cell infiltration and the efficacy of anti-PD-1 [56, 57]. Recombinant IL-18 based therapy has been under clinical trials for stimulating CD8⁺ T cells anti-tumor responses, and its efficacy has been reported in synergy with ICI [58]. Predominantly expressed on T and NK cells, co-stimulatory receptor CD226 opposes the competing inhibitory

receptor TIGIT to augment or disrupt, respectively, effector T cell functions [59]. Although still in early clinical phase, therapies targeting the TIGIT/CD226 axis are considered a very promising ICI as monotherapy or in combination with the PD-1/PD-L1 therapies [60].

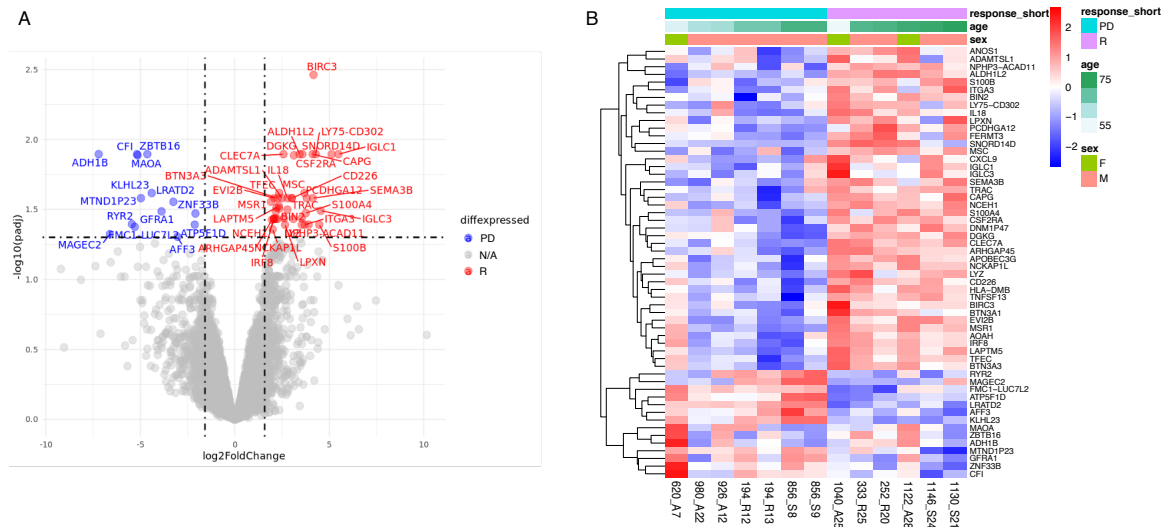


Figure 2-5: Differentially expressed genes between pre-anti-PD-1 treated PD and R samples. A. Volcano plot of differentially expressed genes. Adjusted $p < 0.05$, $\text{FoldChange} > \text{or} < 3$. B. Heatmap shows expression of differentially expressed genes in each sample. Color reflects $\log_2(\text{FoldChange})$.

In addition, we would like to point out that BIRC3 (Baculoviral Inhibitor of apoptosis Repeat Containing 3) had the most significant association with anti-PD-1 response. The role of BIRC3 up-regulation was initially puzzling, as high BIRC3 expression correlated with gliomas progression [61], yet its inactivation consistently associated with poor survival in chronic lymphocytic leukemia [62]. Using scRNA-seq, we found that increased BIRC3 expression as a signature of an activated state in conventional dendritic cells and the implications of this finding are further discussed in Chapter 5. From gene set analysis, we again observed a wide variety of innate and adaptive immune activities enriched in anti-PD-1 responders (Figure 2-6).

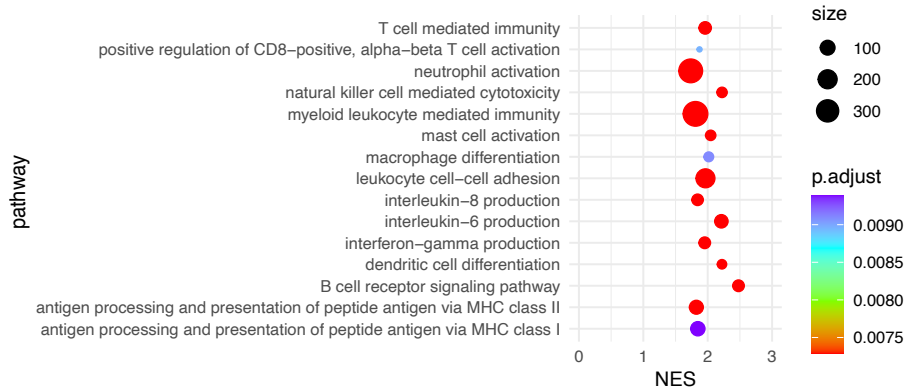


Figure 2-6: Selected differentially expressed gene sets enriched in pre-anti-PD-1 treated R samples. NES, net enrichment score. Size indicates the number of leading edge genes. Color reflects adjusted p.

anti-PD-1-specific progressive disease predictors

We also found a few genes, including MAOA, MAGEC2, and GFRA1, that were significantly associated with resistance to anti-PD-1 but not significant in the expanded cohort analysis (Figure 2-5). With high intratumoral MAOA (Monoamine oxidase A) expression correlating with poor survival in multiple cancers, preclinical mouse studies have successfully used MAOA inhibitors to suppress tumor growth through macrophage reprogramming [63]. MAGEC2 (Melanoma-associated antigens encoding family C2) is highly expressed in melanoma and other tumors but not in normal tissues, and strongly associates with poor prognosis and epithelial-mesenchymal transition [64]. Leveraging the tumor specificity of MAGEC2 expression, MAGEC2 TCR T cell has been engineered and is currently under phase I/II trial for advanced melanoma [64]. Again, we found gene sets related to cell division, DNA repair, and energy metabolism enriched in anti-PD-1 resisters, similar to the findings in the extended ICI cohort analysis (Figure A-5).

Immune infiltration in anti-PD-1 responders and progressors

Lastly, we used *CIBERSORTx* to deconvolve the pre-anti-PD-1 treated tumor composition from bulk RNA-seq. To confirm the inferred results, we compared the inferred tumor fraction with tumor purity derived from co-extracted whole exome sequencing

and established the fidelity of deconvolution (Figure A-6). Although inferred collective abundance of immune cells was similar between progressors and responders, CD8+ T cell fraction was inferred to be significantly higher in responders (Figure 2-7). The high number of T cell related DEGs enriched in responders was consistent with the CD8+ T cell-rich composition inferred by deconvolution.

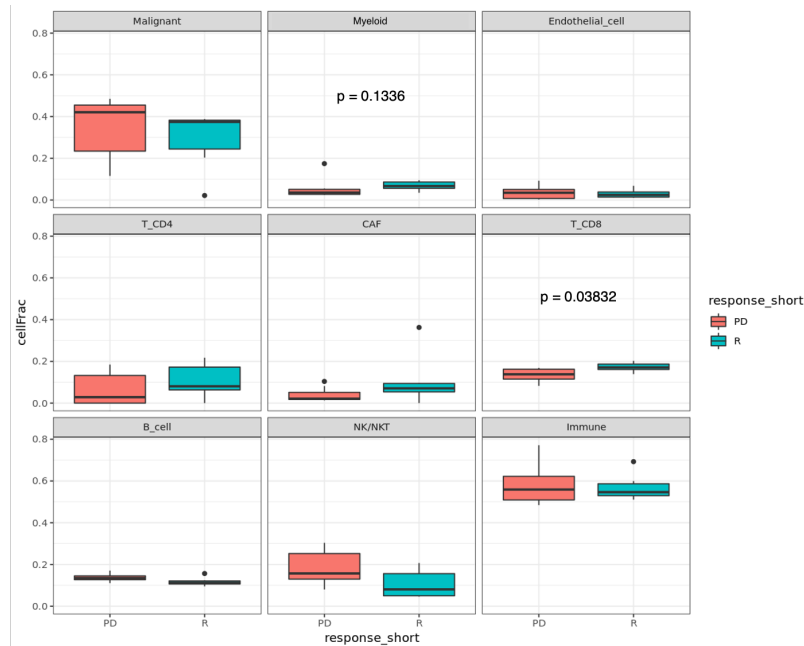


Figure 2-7: Cell type deconvolution of RNA-seq data comparing pre-anti-PD-1 treated PD and R samples. Wilcoxon test. 7 PD, 6 R.

2.4 Contributions and future steps

In this chapter we studied the landscape of ICI responders and progressors through differential expression analysis, gene set enrichment analysis, and cell type deconvolution. After establishing *Limma-Voom* as the most robust differential analysis framework, we confirmed the high innate and adaptive immune activities in ICI responders and established several anti-PD-1 response markers, including IL18, CXCL9, and CD226. Additionally, we also discovered two novel marker genes, AXL and BIRC3, associated with response. In Chapter 5, we use scRNA-seq to concentrate the study of BIRC3 in a novel conventional dendritic cell state.

For ICI resistance biomarkers, we also found a short list of genes, including *AFF3* and *CDCA7*, with known roles in promoting tumor growth. We would like to validate these progression associated genes in larger ICI-treated melanoma cohorts before proposing them as clinical biomarkers. Additionally, we found progressor tumors with significantly enriched activities in malignant growth (e.g. cell cycle, mismatch repair) and bioenergetics (e.g. sugar and fatty acid metabolisms). Finally, using *CIBERSORTx* deconvolution, we found lower levels of T cells and myeloid cells in progressors but no overall difference in immune infiltration compared to the responders. To investigate how a pre-existing immune ‘hot’ environment could still lead to ICI failure, we looked into the pre- and on-treatment changes in progressor tumors in Chapter 3.

2.5 Methods

2.5.1 RNA-seq data generation and preprocessing

Briefly, L.H. and K.G. extracted total RNA from 5-20 mg of melanoma tissues using AllPrep DNA/RNA Mini isolation kit (Qiagen) and allocated 100 ng of total RNA as input for RNA-seq libraries. After removal of rRNA transcripts with SMARTer Stranded Total RNA-seq Pico (Takara Bio USA, Inc), each library was sequenced on HiSeq 2000 (Illumina). The FASTQ files were aligned to hg38 human genome using STAR and quantified using salmon. After filtering the libraries by quality (> 10% reads mapped to genome) and selection criteria described in Chapter 1.3, 39 samples remained in the study.

2.5.2 RNA-seq data batch effect correction

Of the 39 samples in the RNA-seq cohort, 20 were collected retrospectively (formalin-fixed paraffin-embedded tissues) and 19 were collected prospectively (frozen tissues). After finding a strong batch difference between retrospective and prospective collections, we employed *ComBat-seq* to regress the batch effects. Starting from the

untransformed raw count matrix, *ComBat-seq* uses a negative binomial regression to model batch effects and returns the corrected integer matrix [65]. The corrected data can be readily analyzed by the state-of-the-art differential expression methods (e.g. *EdgeR*, *DEseq2*).

2.5.3 Identification of differentially expressed genes

Identification of differentially expressed genes is a key step in understanding phenotypic differences between groups in almost every RNA-seq study. As a result, many methods and tools have been published for the task of differential analysis, yet there is no consensus about a universally best model for all experiment designs. We adopted three widely used methods: *DEseq2*, *EdgeR*, and *Limma-Voom* for the differential gene expression analysis in this project. Prior to the differential analysis by either of the three methods, low count genes should be removed to allow better mean-variance relationship estimation and to reduce the number of statistical tests performed. We filtered the expression matrix and only kept genes that had more than 10 counts in at least half of the samples.

When studying the differential expression between R and PD groups, We used a design formula that takes response as the main variable, and state, treatment group, sex, tissue, and age as the covariates. All three methods produce the $\log_2(\text{FoldChange})$, p value, and BH corrected padj value for each gene. We considered genes with padj < 0.05 and $absolute(\log_2\text{FC}) > 1.58$ as differentially expressed genes (DEGs).

DEseq2

DEseq2 relies on a negative binomial distribution model [45]. Starting with the size factor-adjusted counts (sample-specific scaling factor reflecting the sequencing depth), it first performs a maximum likelihood estimation for the gene-wise dispersion. Then *DEseq2* shrinks the dispersion estimates towards an average value using the assumption that genes with similar expression levels have similar dispersion (α). Finally, *DEseq2* performs a general Linear Model (GLM) fit to estimate the $\log(\text{FoldChange})$

(β) for each gene (Equation 2.1).

$$y_{ij} \sim NB(\mu_{ij} \exp(x_{ij}^T \beta), a_i) \quad (2.1)$$

EdgeR

Similar to *DEseq2*, *EdgeR* makes use of a negative binomial distribution in modeling the counts and moves over-dispersion towards a common dispersion [46]. One major difference between the two methods is their scaling factors calculation: *DEseq2* uses a scaling factor that is related to the median of the geometric means of gene expression values, while *EdgeR* uses the trimmed mean of M-values (TMM) factor.

Limma-Voom

Also normalizing the libraries by TMM, the *Voom* method estimates the mean-variance relationship of the \log_2 (per counts per million reads (CPM)), and generates a weight for each gene and sample that enter the limma empirical Bayes analysis [47].

2.5.4 Gene set enrichment analysis

We performed Gene Set Enrichment Analysis (GSEA) to investigate the pathway activities in each group [48]. All genes were ranked by average \log_2 (FoldChange) and used as input for the R software *fgsea* [66]. Using Kyoto Encyclopedia of Genes and Genomes (KEGG) and Gene Ontology (GO) gene sets annotation information downloaded from MSigDB [67], the *fgsea* algorithm calculates the size-adjusted enrichment score (NES) as a running sum statistic for each gene set and estimates the statistical significance of the NES against a permutation-generated null distribution. Gene sets with BH-adjusted p value < 0.5 and size > 10 were considered significant. When many significant gene sets were detected, we used Enrichment map representation to organize the overlapping gene sets into connected functional modules. The enrichment map function was implemented through the R package *ClusterProfiler* [68].

2.5.5 Cell type deconvolution

While scRNA-seq can offer transcriptional profiling at the single cell level, the technology cannot be applied on fixed clinical specimens for they cannot be dissociated into single cells. As a result, deconvolution techniques have been developed to computationally dissect the cellular contents from such mixed samples. We used *CIBERSORTx* to infer the abundance of 8 cell types from bulk RNA-seq profiles [49]. The 8 cell types and their gene expression signatures were derived from the Tirosh et al. single-cell reference [38]. The *CIBERSORTx* framework is based on the assumption that biological mixture samples can be modeled as a system of linear equation: $H \times F = M$, where M represents the n genes $\times k$ mixture samples matrix, H represents a $n \times c$ cell type signature matrix of n genes across cell types c_1, \dots, c_i , and F represents the $c \times k$ fractional abundance matrix that records mixing proportions of c cell types for k samples. With user input H and M , *CIBERSORTx* estimates F using a ν -support vector regression, a machine learning technique robust to noise and collinearity [49]. Due to the batch effect between the retrospective and prospective collections, we separated the untransformed raw RNA-seq expression matrix by collection and applied *CIBERSORTx* independently.

Chapter 3

Tumor microenvironment evolution during ICI treatment

In this chapter, we aimed to understand how ICIs shape the tumor microenvironment. With some knowledge of the pre-treatment transcriptomic differences between responder and progressor tumors, we asked the question of how the responders and progressors react similarly and differently to ICIs. While previous studies have attempted to elucidate how ICIs enhance the immune functions in tumors that respond favorably, little is known about how non-responding tumors are shaped by ICIs. Therefore, we sought to bring light to the mechanisms that exacerbated ICI failure at the tumor and cellular level. To pinpoint the cellular mediators of tumor-level observations, we paid additional attention to how ICIs failed to reinvigorate the exhausted CD8+ T cells in progressor tumors [69].

3.1 Background

ICI treatments strengthen immune activities in responders

The hypothesis that ICIs can shape the tumor microenvironment to reflect clinical outcome is not new. Riaz et al. have sequenced 26 matched pre- and on-anti-PD-1 (Nivolumab) samples (6 R, 8 stable disease, 12 PD) to examine the treatment in-

duced expression changes [4]. The study found 400+ differentially expressed genes (DEGs) in on-treatment samples, regardless of response, with most DEGs involved in immune regulation [4]. The study also observed increased expression in many immune checkpoint genes, including PDCD1 (PD-1), CTLA-4, CD274 (PD-L1), CD80 (CTLA-4-L), LAG3, and TNFRSF9 (4-1BB), regardless of response to therapy. In pre- versus on-treatment analysis, the study found responders up-regulated a larger set of immune-related genes, including genes in lymphocyte activation, migration, and cytolytic activities, and down-regulated pathways in cell-cycle regulation, mitotic divisions, and translation. Additionally, the study also performed TCR sequencing for pre- and on-treatment responders and found clonal expansion of specific populations associated with treatment while CDR3 diversity remained similar. Bulk RNA-seq deconvolution showed an increase of CD8+ T and NK cell levels and a decrease in macrophages when comparing on-treatment responders to pre-treatment. While DEGs were also found in the on-treatment progressor samples, the study did not identify any specific gene modules associated with progressors, except minimal immune activation [4].

Potential mechanisms of ICI resistance

Although the ICI resistance mechanisms are unknown in most progressor tumors, there are a few speculated programs. Down-regulated tumor antigen presentation is a likely route of immune evasion. Case studies of melanoma and other cancers have reported acquired truncating mutation of B2M, a key gene in stabilizing MHC I molecules, at the time of progression [38]. Secretion of IFN- γ from effector T cells can trigger the JAK-STAT pathway in tumor cells to induce cell death [70]. As a result, defects in IFN- γ signaling is another speculated mechanism of ICI resistance. Cell line studies have reported the inactivation of JAK1/JAK2 or amplification of IFN- γ pathway inhibitors resulted in the loss of tumor sensitivity to IFN- γ [70]. Additionally, some reports have found up-regulation of other T cell checkpoints, including TIM3, LAG3, and VISTA in resisting tumors during ICI treatment, although it remains unclear if such association is causal.

3.2 Research approach

Using 3 pairs of responder pre- and on-ICI (anti-PD-1, anti-PD-L1, or combination therapy) RNA-seq (1130_S21, 1130_S22, 252_R20, 252_R21, 654_R38, 654_R39) and 2 pairs of progressor pre- and on-ICI RNA-seq (926_A12, 926_A13, PDL002_R44, PDL002_R45), we first looked into the gene sets up regulated by treatment in responders and progressors, respectively. To confirm the signal in a larger sample size, we used *Limma-Voom* derived gene statistics to repeat the gene set analysis with unmatched pre- and on-ICI responders (10 pre, 6 on) and progressors (12 pre, 9 on) samples. Then we used deconvolved cell type abundances to relate the on-ICI gene programs to tumor composition.

For a more detailed investigation of progressor tumors, we performed scRNA-seq on 10 progressor tumors (5 pre, 5 on) and analyzed the on-ICI cell population changes. Lastly, we focused our attention on CD8+ T cells and used two approaches, pseudo bulked *Limma-Voom* and *NEBULA*, to study the pre- and on-ICI differential expression and pathways in CD8+ T cells.

3.3 Results and discussions

3.3.1 ICIs enhance immune functions in responders

To study how ICIs shape the tumor microenvironment, we first performed paired pre- versus on-treatment analysis in both responders and progressors. To capture the most robust functional signals and reduce the measuring noise, we focused on gene sets and pathways instead of genes. The on-treatment responders showed significant enrichment in several immune functions, including T cell receptor signaling, IgA production, NK cell mediated cytotoxicity, Fc gamma mediated phagocytosis, cytokine signaling, and antigen presentation (Figure 3-1A). The favorable response of these samples were also reflected by a decrease in the DNA replication and ribosome enrichment scores, potentially reflecting reduced tumor growth. Beyond the immune and tumor growth related pathways observed in previous studies, we also

detected an increase in cell adhesion molecules (CAMs) and decrease in oxidative phosphorylation. Next, in an expanded analysis of unpaired on-treatment samples, we again found enrichment in many immune gene sets and decrease in tumor growth and metabolism pathways (Figure 3-1B). On the adhesion related pathways, we saw on-treatment samples associated with both increase in cell adhesion and decrease in anchoring junction (Figure 3-1B). While such observation could possibly indicate gain and loss of adhesion functions in two or more cell types, more detailed studies are required to pinpoint the specific adhesion functions involved.

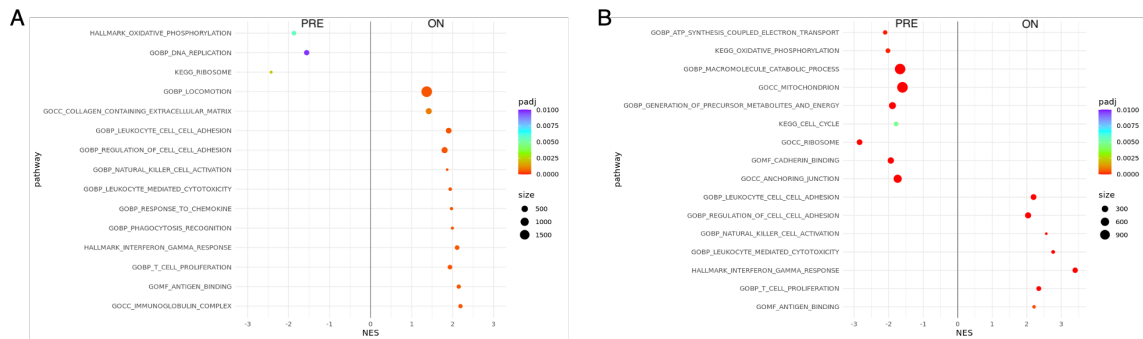


Figure 3-1: Differentially enriched gene sets in pre- and on-treatment responders. A. Selected differential gene sets in paired pre-versus-on analysis. B. Selected differential gene sets in unpaired pre-versus-on analysis. NES, net enrichment score. Size indicates the number of leading edge genes. Color reflects adjusted p.

3.3.2 ICIs affect ribosomal and metabolic activities in progressive disease

On the pre- versus on-ICI analysis of progressor disease, we saw unhalted tumor growth in on-treatment samples, reflected by increase in ribosome and DNA replication activities (Figure 3-2). Similar to the trend in on-treatment responders, the two pairs of on-treatment progressors also showed decreased fatty acid and small molecule metabolism (Figure 3-2A). Although pre-treatment progressors exhibited higher sugar and fatty acid metabolism than pre-treatment responders (Figure A-4B), these metabolic activities were decreased during ICI treatment in both respon-

der and progressor tumors. In the opposite direction to the on-treatment responders, on-treatment progressors had reduced cell-cell adhesion in the paired analysis (Figure 3-2A), while the unpaired on-treatment progressors showed increase in epithelial-mesenchymal transition (Figure 3-2B). These findings exhibited the loss of anchorage dependent growth in progressive disease, which is recognized as one of the cancer hallmarks [71]. With already lower TNF- α activity in pre-treatment progressors than responders (Figure A-4A), progressor tumors showed decreased TNF- α signaling and IFN- γ response in response to ICIs (Figure 3-2B).

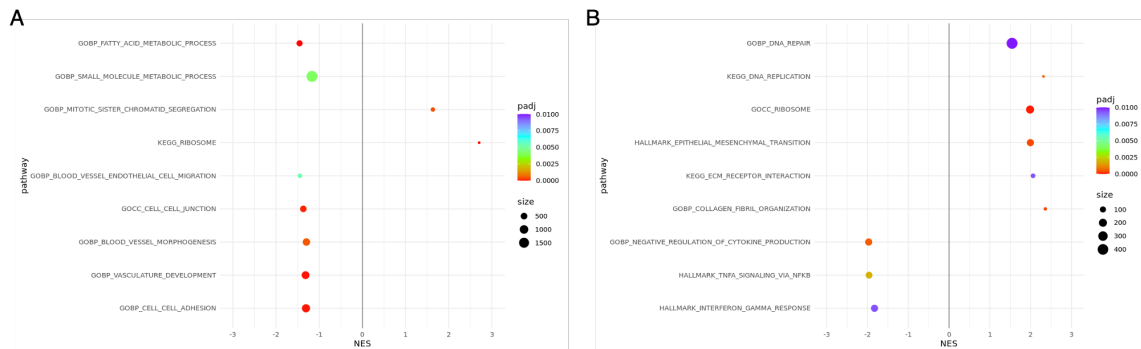


Figure 3-2: Differentially expressed gene sets enriched in pre- and on-treatment progression diseases. A. Selected gene sets detected in paired pre-versus-on analysis. B. Selected gene sets detected in unpaired pre-versus-on analysis. NES, net enrichment score. Size indicates the number of leading edge genes. Color reflects adjusted p.

3.3.3 Immune infiltration in progressive disease unaffected by ICIs

To relate to the decrease of immunological signaling in on-ICI progressors, we used deconvolved cell type abundances to infer immune infiltration. Both progressors showed high levels of immune filtration pre-treatment and growth of malignant cells on-treatment (Figure 3-3A). On-treatment progressor samples had a slight decrease in the immune compartment proportion due to the increase in malignant compartment. Additionally, we further checked the level of CD8+ T cells in progressors, and confirmed that the level of CD8+ T cells in the immune compartment did not

decrease on-treatment (Figure 3-3B). These combined results showed no evidence of progressive tumors developing immune exclusion before or during ICIs treatment.

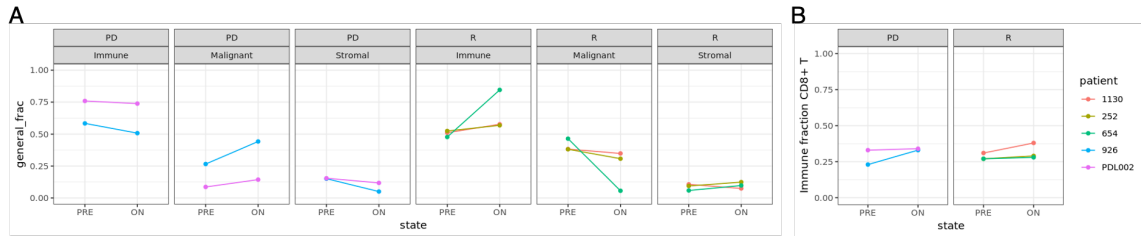


Figure 3-3: Changes in deconvolved tumor composition following ICI treatment. A. Line graphs show changes in immune, malignant, stromal compartment abundances. B. Line graphs show changes in CD8⁺ T frequency within the immune compartment.

Single cell measurement of immune infiltration

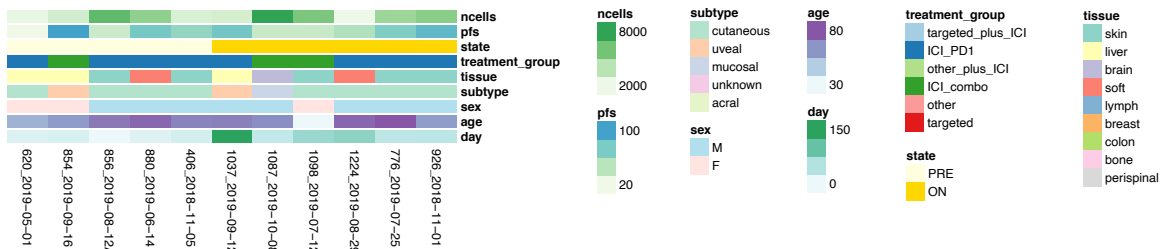


Figure 3-4: Clinical characteristics of pre-, on-ICI therapy progressive disease scRNA-seq samples. Progression free survival in days. Biopsy day measured in reference to treatment start date. Biopsy state assigned in reference to start of treatment. Melanoma subtype identified by primary tumor location. Tissue indicates metastasis location. Number of cells in each sample recorded. n = 11.

For a more detailed investigation of progressor tumors, we sequenced 64,362 cells from 11 progressor tumors (5 pre-, 6 on-ICI; Figure 3-4). Using known expression markers, we identified immune cells (ITGAM⁺ or PTPRC⁺) and CD8⁺ T cells (CD3E⁺, CD8A⁺) (Figure A-7). Both pre- and on-ICI samples exhibited sufficient immune cell and CD8⁺ T cell infiltration (Figure 3-5). Additionally, we observed a slight increase of immune cell abundance associated with ICIs treatment.

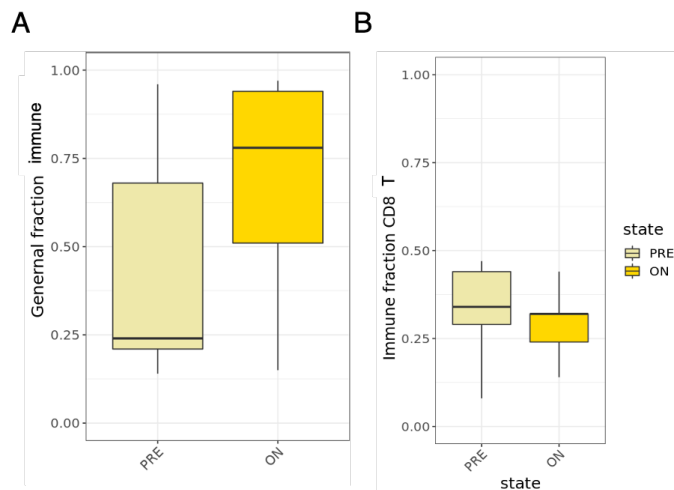


Figure 3-5: Immune infiltration measured by scRNA-seq. A. Box plot shows abundance of immune cells in pre- and on-ICI samples. B. Box plot shows frequency of CD8⁺ T cells in immune cells in pre- and on-ICI samples. 5 pre, 6 on.

3.3.4 ICIs affect CD8⁺ T cell activities in progressive disease

Using single cell RNA-seq, we focused our attention on CD8⁺ T cell’s contribution to the tumor-level effects of the ICIs in progressors. One well-received differential expression analysis practice is the pseudobulk-based *Limma-Voom* approach, where the cell-by-gene expression matrix is sample-aggregated to a ‘bulk’ sample-by-gene matrix as the input for *Limma-Voom* [72]. By aggregating the expression across cells, pseudobulk approach is expected to flatten out the noisy nature of scRNA-seq and reduce the false discovery rate, while preserving the most robust biological signals. However, with high sample-level heterogeneity in this specific dataset, we found pseudobulk-based *Limma-Voom* approach severely underpowered (results not shown). To address this lack of statistical power, we employed a novel single-cell differential analysis framework, *NEBULA*, which accounts for both subject-level and cell-level overdispersions [73]. By accounting for the inter-sample heterogeneity effect, *NEBULA* detected similar top DEGs as the pseudobulk-based *Limma-Voom* analysis detected, but with higher statistical confidence.

T cell cytotoxicity is diminished during ICIs treatment in progressive disease

The on-treatment progressor CD8+ T cells showed significantly decreased expression in genes related to granzyme and cytotoxicity regulation (e.g. GZMA, GZMH, CST7, CTSC; Figure 3-6, A-8). We also observed lower lymphocyte homing cytokine expressions (e.g. CCL4, CCL5, CCL4L2) during ICIs treatment, which agreed with the decrease in relative CD8+ T cell frequency in the immune compartment (Figure 3-5B). GSEA analysis confirmed that, compared to pre-treatment, on-treatment T cells had reduced activity in IFN- γ , immune process regulation, T lymphocyte chemotaxis, and T cell apoptosis (Figure 3-7).

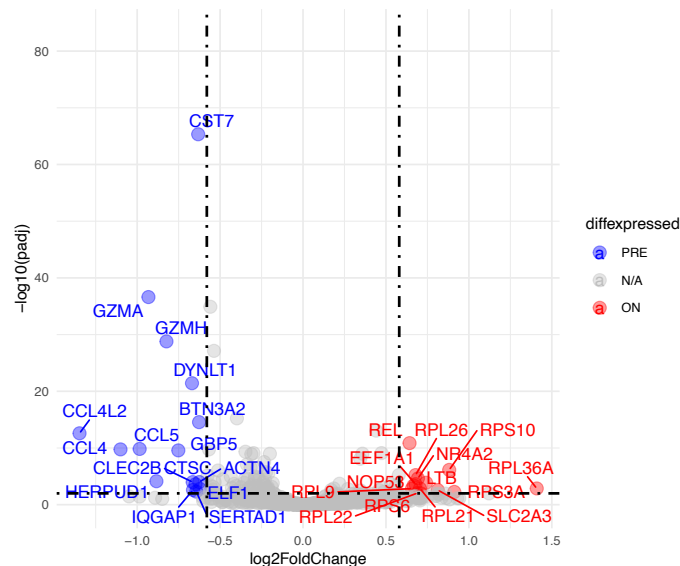


Figure 3-6: Volcano plot of differentially expressed genes in pre- and on-ICIs CD8+ T cells. Adjusted $p < 0.01$, $\text{FoldChange} > \text{ or } < 1.5$.

CD8+ T cell transcriptomes reflect tumor-level cell adhesion and ribosomal activity in progressive disease

Agreeing with the tumor-level observation, we found on-ICIs CD8+ T cells showing down-regulated cell adhesion and up-regulated ribosomal activity in progressive disease (Figure 3-7). The down-regulation of cell adhesion was also reflected by decreased CLEC2B (C-type lectin domain family 2 member B) expression, a gene involved in

many functions including cell-cell adhesion and immune response to pathogens (Kuttruff et al., 2008). Genes up-regulated in on-treatment CD8+ T cells were mostly ribosomal genes or involved in ribosome genesis (e.g. RPS10, RPL22, NOP53; Figure 3-6), which was confirmed in the enrichment of ribosome and peptide synthesis pathways (Figure 3-7). We speculated that the higher ribosomal activity detected in on-treatment CD8+ T cells reflected a higher abundance of naive cells, which are known to have high expression of ribosomal genes [74]. By using a panel of naive T cell makers including CCR7 and IL7R, we indeed saw higher expression of naive signatures in the on-treatment than pre-treatment CD8+ T cells (Figure 3-8A). In Chapter 4, we presented the association of naive T cell populations and treatment state in more detail.

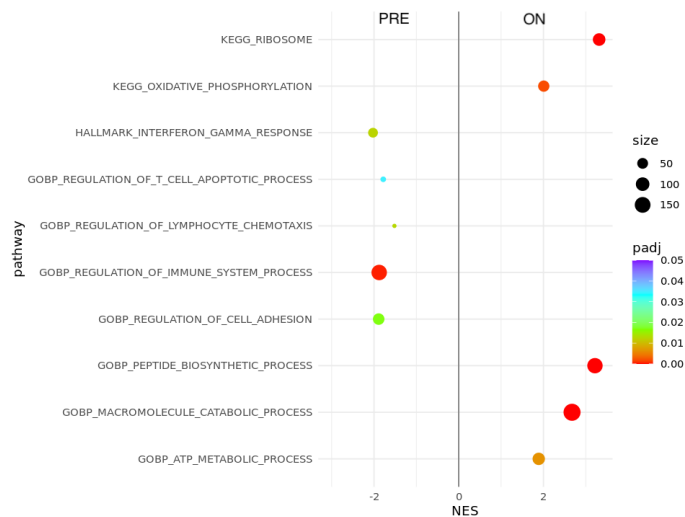


Figure 3-7: Selected differentially expressed gene sets in pre- and on-ICIs CD8+ T cells. NES, net enrichment score. Size indicates the number of leading edge genes. Color reflects adjusted p.

CD8+ T cell displays elevated oxidative phosphorylation in progressive disease

Apart from the ribosome signature, GSEA also found on-treatment T cells from progressive disease with higher activities in oxidative phosphorylation and ATP metabolism. As discussed in Chapter 4, the elevated metabolism in T cell reflected the exhausted

state. Using expression of checkpoint molecules (e.g. PDCD1, TIGIT) as exhaustion markers, we confirmed that T cell exhaustion was aggravated in on-ICI progressors (Figure 3-8B). The potentially inflated need for energy under conditions of stress could contribute to the failure of treatments in reprogramming exhausted T cells to a cytotoxic state [75]. Interestingly, in the context of these oxidative phosphorylation and ATP metabolism findings, a recent melanoma study has reported detection of both peripheral circulating and tumor infiltrating CD8+ T_{oxphos} cells with elevated energy metabolism, including increased mitochondrial activity and ATP production [76]. The study has also found that CD8+ T_{oxphos} were more pronounced in ICI-resistant tumors and proposed using CD8+ T_{oxphos} level to predict ICI response [76].

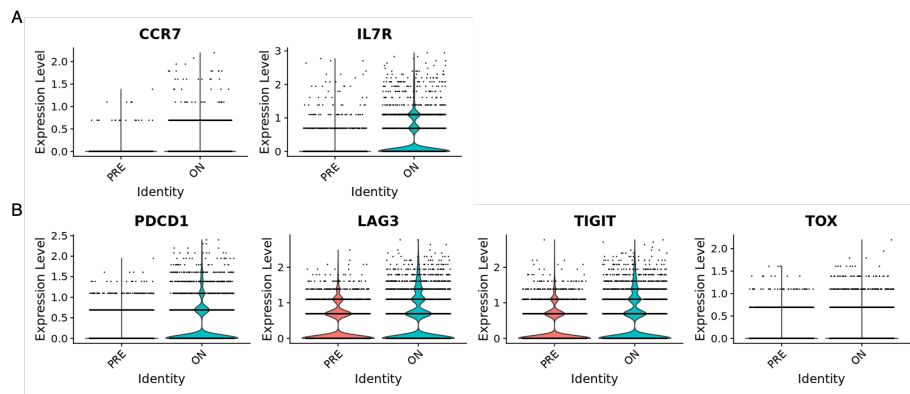


Figure 3-8: Molecular features of pre- and on-ICI CD8+ T cells. A. Violin plots show expression of selected naive T cell marker genes. B. Violin plots show expression of selected exhaustion marker genes.

3.4 Contributions and limitations

In this chapter we found that ICIs lowered the tumor-level fatty acid metabolism and ATP generation in both responders and progressors. ICIs affected two other tumor characteristics, cell-cell adhesion and ribosomal activity, differentially in responders and progressors through CD8+ T cells. Through RNA-seq deconvolution and scRNA-seq, we confirmed that both pre- and on-treatment progressors had adequate

immune infiltration, and consequently rejecting immune exclusion as a potential resistance mechanism. Focused study of CD8+ T cells found on-treatment progressors with reduced activities in granzyme production, lymphocyte homing, IFN- γ signaling, and adhesion, reflecting their diminished anti-tumor cytotoxicity. Additionally, we observed that on-treatment progressor CD8+ T cells had elevated ribosomal and mitochondrial activities. While we attributed the enrichment of ribosome to higher naive cell abundance and the elevated mitochondrial oxidative phosphorylation to aggravated exhaustion, *invitro* experiments, such as immunohistochemistry staining or Seahorse assay, are required to validate our hypotheses.

We acknowledged that a major limitation of our study is the approach of using unpaired pre- and on-treatment samples. Although limited by the scarcity of paired data, we successfully adopted a more complex statistical model, *NEBULA*, to account for the patient-level heterogeneity when analyzing unpaired samples. While we demonstrated *NEBULA* as a powerful statistical framework, we would like to expand the sample size to establish higher confidence in the findings.

3.5 Methods

3.5.1 Identification of differentially expressed genes and gene sets from RNA-seq

We obtained the gene expression $\log_2(\text{FoldChange})$ between pre- and on- ICI samples using *Limma-Voom* with the design formula taking treatment state as the main variable, and treatment group, sex, tissue, and age as the covariates. Then, we used Gene Set Enrichment Analysis (GSEA) to investigate the pathway activities in pre- and on-ICI states, as described in Chapter 2 Methods. Additionally, we performed GSEA on paired pre-on samples by ranking genes using the average *on* – *pre* expression (E) difference across pairs (Equation 3.1).

$$Stat = avg(E_i^{on} - E_i^{pre}) \tag{3.1}$$

3.5.2 scRNA-seq data generation and preprocessing

L.H. and K.G. dissociated fresh melanoma tumors using tumor dissociation protocols and prepared the scRNA-seq libraries using the 10x Genomics chromium controller and reagent kits. With a target of 5000 cells per sample, 150-300 pM of pooled libraries were profiled using the Novaseq S2 (Illumina) technology. BioMicro Center (MIT) received the sequences, mapped the reads against the GRCh38 human reference genome, and quantified the read counts using *Cell Ranger* pipeline version 3.1.0 (10x Genomics Inc). E.R. used *Scrublet* to remove ambient RNA in each sequencing library and called multiplets using *CellBender* [77]. After filtering the multiplets, we performed quality control on the cells by selecting cells with between 2,000 and 6,000 genes detected and $< 10\%$ mitochondrial reads. We then normalized and scaled each library using *SCTransform* (*Seurat v4.01*) to adjust for sequencing depth and remove mitochondrial mapping percentage as a confounding variable [78].

3.5.3 scRNA-seq data dimensionality reduction, cell-type identification, and clustering

For downstream analysis, we merged the libraries together and performed principal component analysis (PCA) using the genes detected in all samples. After obtaining the low-dimensional embeddings, we performed Uniform Manifold Approximation and Projection (UMAP) on the top 40 principal components to visualize the dataset. We identified CD8⁺ T lymphocytes (CD3E⁺, CD8A⁺, GZMA⁺) from the cohort using known cell-type specific markers. To identify the proliferating cells, we used the *CellCycleScoring* function to calculate the S phase score and G2M phase score for each cell [78]. Proliferating cells were not used in cell type specific analyses. We then constructed a k Nearest Neighbor (kNN) Graph in the top 40 principal components space and clustered cells using the Louvain algorithm. In all the datasets, we used the default parameter $k = 20$ and resolution parameter ranging from 0.2 to 1.4 and proceeded with the lowest resolution that sufficiently highlighted the biological differences between clusters.

3.5.4 scRNA-seq integration

Joint analysis of multiple samples often faces difficulties in identifying cell populations which are shared across samples. Differences in sequencing platform, data source, or sample-level noise can lead cell populations to co-cluster with other distinct cells from the same dataset, rather than co-clustering with cells of the same biology from different datasets. In this study, we used *Harmony* for the task of integration [79]. Starting with the PCA embeddings of a joint dataset, the *Harmony* algorithm uses a variant of soft k-means clustering that favors mixing datasets in a cluster. Then, *Harmony* calculates a correction factor for each cluster and corrects each cell by the linear combination of correction factors according to their membership in the soft cluster assignment. This soft clustering and factor correction is repeated until convergence. *Harmony* transforms the cells to a new space that can be directly followed up by UMAP dimensionality reduction and Louvain algorithm clustering.

3.5.5 Identification of differentially expressed genes and gene sets from scRNA-seq

Pseudo bulk analysis with *Limma-Voom*

Differential expression analysis in single cells is often challenging due to the high dropout rate, varying cell quality, and noisy nature of single cell measurements. One way to circumvent these problems is to create pseudo-bulk samples by combining single cell count matrices into one matrix that resembles a bulk RNA-seq sample. The grouping is operated with the assumption that cells in the one group are relatively homogeneous and the existing difference among them can be ignored. we generated the pseudo-bulk matrix by grouping the single cells by cell type and tumor sample and averaging the expressions within a group. Prior to applying the bulk RNA-seq differential expression methods on the pseudo-bulk matrix, we filtered the genes and only kept genes that were detected in at least 20% cells in both pre- or on-ICI conditions. We then used *Limma-Voom* to perform differential expression analysis on the pseudo-bulk samples with the same formula and parameters as bulk RNA-seq

analysis.

NEBULA

While the pseudo-bulk analysis approach on single cells should be able to detect most of the significant expression differences between cells of two conditions, it is often statistically underpowered due to the much smaller sample size at the pseudo-bulk level. To analyze the single cells at the cell level, we need a framework that can remove the inter-sample heterogeneity effect when comparing cells of two different conditions. A recently published statistical model, *NEBULA*, allowed us to do so [73]. Using a negative binomial mixed-effects model, *NEBULA* accounts for both subject-level and cell-level overdispersions. Parameterized by σ^2 , the subject-level overdispersion reflects differences caused by batch effects, patient genetics, and other clinical covariates, while the cell-level overdispersion ϕ reflects cellular covariates such as mitochondria percentage or cell cycling (Equation 3.2).

$$y_{ij} \sim NB(\mu_{ij} \exp(x_{ij}^T \beta + \log(\omega_i)), \phi_i) \quad (3.2)$$

Prior to *NEBULA* analysis, we filtered the samples with > 50 CD8+ T cells and subsetted the genes that were expressed in at least 20% cells in both pre- or on-ICI conditions. We then ran *NEBULA* on the count matrix with sample-level information of each cell, nFeature_RNA as the size factor, and tissue, age, treatment group, sex, and mitochondria percentage as covariates.

Chapter 4

Diversity of T cells in the tumor microenvironment

T cells in the tumor microenvironment encounter an immense number of other cells and molecules that could shape their dynamic differentiation paths. Their complex development process is further influenced by the presence of therapeutics and the tumor's evolving escape mechanisms to therapy. Understanding the cellular differentiation paths and mechanisms can help us understand their functional evolution. It can also give clues on how to, *in vivo*, manipulate differentiation into states that are associated with favorable prognosis or, *in vitro*, re-create desirable cell states for cell therapies [80]. By linking cells in early time points to their future selves or progeny, we can investigate how cells transition from one state to another and estimate the state transition likelihoods [81]. In this chapter we aim to 1) characterize the subpopulations of tumor-infiltrating T cells to gain a better understanding of the T cell compositions in melanoma tumors, 2) study the developmental trajectory of these subpopulations, and 3) investigate the relationship between the identified subpopulations and clinical variables such as treatment group or state.

4.1 Background

Human T cell development and differentiation

T cells, or T lymphocytes, develop and undergo selection at thymus before exporting to the periphery [82]. Peripheral T cells contain many subsets including naive T cells, memory T cells, and regulatory T cells (Tregs). After encountering antigen and co-stimulatory molecules presented by dendritic cells, naive T cells differentiate into effector cells, which execute immune functions to kill infected cells or cancer cells [83]. With notable heterogeneity at the single-cell level, CD4+ effector T cells secrete key cytokines to promote response to various infections, while CD8+ effector T cells have cytolytic capacity. While activated effector cells are short-lived, some become memory T cells that maintain long-term immunity. Under immunosuppression mechanisms or persistent antigenic stimulation, effector T cells can also differentiate into a dysfunctional “exhausted” state. Defined by sustained expression of checkpoint molecules (e.g. CTLA-4, PD-1, LAG-3, TIM-3), exhausted T cells have impaired effector function, thus fail to kill cancer cells [84].

Treg cells are responsible for maintaining tolerance to self or ubiquitous antigens and keeping the immune response in check. By regulating T cell effector function and proliferation, Tregs are critical in preventing autoimmunity [82]. Also developed from CD4+CD8+ thymocytes are the nature killer T (NKT) cells, which feature both conventional T cell and NK cell characteristics [85]. Although rare in abundance, NKT cells can kill target cells directly or indirectly by stimulating other immune cells and are increasingly recognized as a key mediator of anti-tumor immunity [85].

Trajectory inference reveals T cell differentiation paths

Lineage tracing methods have advanced from using microscopy-based methods to sequencing inherited ‘barcodes’ in cell clones [80]. Considered as the next generation of ‘microscopes’, single-cell technologies can capture much more cellular information at once. Although the technology of sequencing single cells over time has yet to arrive, computational methods have been developed to infer developmental processes from a

single sample that contains cells in different points of development. In recent years, trajectory inference has been established as a subfield of computational biology and is frequently studied in the context of stem cells, neural generation, hematopoiesis, and immune responses [86].

A recent pan-cancer study of tumor-infiltrating T cells leveraged multiple trajectory inference methods to study the diverse CD4⁺ T and CD8⁺ T cell differentiation paths and the regulation of state transitions. Using diffusion map and RNA velocity, Zheng et al. delineated the three major fates of naive CD4⁺ T cells as terminally differentiated effector memory T cells (Temra), T follicular helper/T helper 1 cells (TFH/TH1), or TNFRSF9⁺ Treg cells [31]. Diffusion map and RNA velocity analysis also demonstrated that naive CD8⁺ T cells differentiate to either terminally differentiated effector memory cells or terminally exhausted cells (Tex). More detailed analysis of the naive to terminal Tex cells trajectory showed that the development of exhaustion follows two major paths going through effector memory T cells (path 1) or tissue-resident memory T cells (path 2). Additionally, different cancer types have different paths towards exhaustion. When analyzing the melanoma samples in isolation, the study found that CD8⁺ T cells exhibit a single continuous progression of cells from pre-dysfunctional state to dysfunction [31]. The developmental trajectory of resting to activated T cells is conserved across melanomas and more than half of melanoma samples in the study had a high proportion of Tex.

4.2 Research approach

In order to have more statistical confidence in our findings, we expanded the study cohort to 39 samples treated with ICI therapies, targeted therapies, other therapies, targeted plus ICI therapies, or other plus ICI therapies. The 39 samples were taken pre, on, or post therapy and had various prior therapy histories (Figure 4-1). We preprocessed, QCed, and integrated the 39 libraries; performed 2D embedding; and clustered them (Chapter 3 Methods). Using the markers described in Chapters 3 and 5, we identified at least 14 cell types in the samples (Figure A-9). We further

clustered the CD4+ T and CD8+ T populations, and characterized the clusters by differentially expressed genes and pathways. In agreement with the current best practice in trajectory inference, we compared multiple methods to establish an agreed topology [87]. In this chapter, we used diffusion map [88], *Monocle3* [89], *CytoTrace* [86], and RNA velocity [90] to infer the differentiation trajectories in CD8+ T cells and CD4+ T cells.

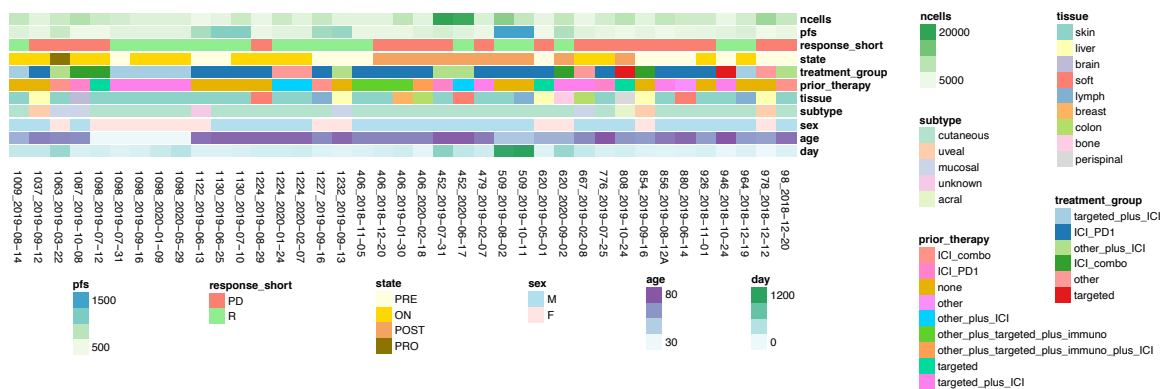


Figure 4-1: Clinical characteristics of scRNA-seq cohort. Progression-free survival in days. Biopsy day measured in reference to treatment start date. Tumor response group assigned by RECIST criteria. PD, progressive disease; R, response. Biopsy state assigned in reference to start of treatment. PRO, post-progression. Melanoma subtype identified by primary tumor location. Tissue indicates metastasis location. Number of cells in each sample recorded. $n = 39$.

4.3 Results and discussions

4.3.1 Diversity of tumor-infiltrating CD4+ T cells

We identified 17,952 CD4+ T cells across 34 single-cell transcriptomes and organized these cells into 8 clusters (Figure A-10A). Cells in all clusters were good in quality and were well integrated across samples on the UMAP (Figure A-10B). We identified six clusters of CD4+ T cell subpopulations, including the commonly reported naive T cells (Tn), memory T cells (Tm), and Tregs (Figure 4-2A). Identified by high expression of the naive marker CCR7, Tn (c0) also showed significantly high expression

of ribosomal genes, which are indications of cells in naive or quiescent states (Figure 4-2B, 4-3) [74]. Tm (c3) showed high expression of memory marker CCL5 and enrichment in gene sets related to migration and activation, suggesting its effector potential (Figure A-11). Regulated by transcription factor FOXP3, Tregs (c1) also expressed high levels of co-inhibitory molecules CTLA-4 and TIGIT (Figure 4-3)[69]. Additionally, we identified a NKT (c5) subpopulation with a unique expression of XCL1, XCL2, and KLRD1, in addition to CD4, agreeing with the innate lymphoid phenotype (Figure 4-2).

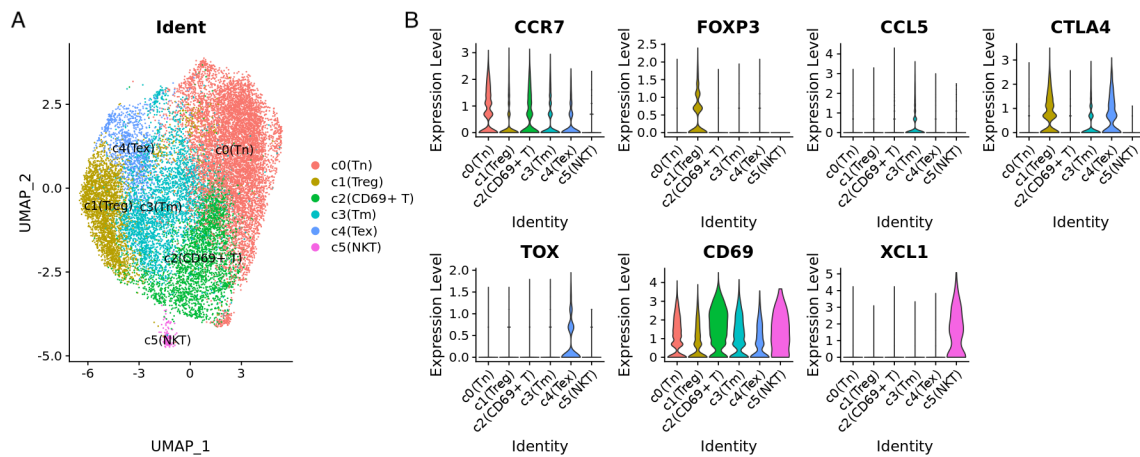


Figure 4-2: Identification of CD4⁺ T cell subsets. Tn, naive T cells; Treg, regulatory T cells; Tm, memory T cells; Tex, exhausted T cells; NKT, Natural Killer T cells. A. UMAP plot shows six clusters of CD4⁺ T cells recovered. B. Violin plots show expression of selected signature genes in CD4⁺ T cell subpopulations.

Exhausted CD4⁺ T cell shows elevated glycolytic metabolism

To further define the other subpopulations, we examined the top differentially expressed genes and pathways of each cluster. Cluster 4 showed a high expression of checkpoint molecules, including TOX, CTLA-4, PDCD1, and TIGIT, indicating cells in an exhausted state (Tex; Figure 4-3B). Additionally, Tex also showed high expression of GAPDH, which suggested an elevation in glycolytic metabolism. Pathway analysis also reflected that Tex had elevated activities in glycolysis and metabolism of glucose and other small molecules (Figure A-11). As discussed in Chapter 3, the

excessive need for energy in exhausted T cells has been observed in other studies and is starting to be recognized as a feature of the exhaustion state [75].



Figure 4-3: Heatmap of top differentially expressed genes across CD4+ T cell subpopulations. Color reflects normalized expression levels.

Activated CD69+ T cell shows high level of heat shock proteins

Lastly, closer analysis of cluster c2 (CD69+ T) showed high expression of CD69, which is considered a classical early marker of lymphocyte activation (Figure 4-3) [91]. The activated phenotype of CD69+ T was confirmed by its up-regulation of FOS, JUN, and cell-cycle activities (Figure 4-3, S4-3). Additionally, CD69+ T showed high expression in heat shock protein (HSP) family genes (e.g. HSPA1B, HSP90AA1), which encode molecular chaperones for protein folding. HSPs are often induced by cellular stresses such as heat, infectious agents, or, as is most likely in the context of cancer, hypoxia [92]. In particular, HSP90A, encoded by HSP90AA1, has been identified as a therapeutic target to promote T cell anti-tumor activities. One recent study demonstrated that HSP90A inhibition renders tumor susceptible to adoptive T

cell transfer and anti-PD-1 treatment [93]. We hypothesized CD69+ T could be the primary target of these HSPs inhibitors.

4.3.2 Inference of CD4+ T cell differentiation trajectory

After detecting multiple CD4+ T clusters in the tumor samples, we asked how these cell types and cell states are related to each other in the course of differentiation. Using the diffusion map algorithm [88], we summarized the cell similarity based transition probability into diffusion component 1 and component 3, as component 2 only captured non-meaningful noise. The diffusion map concentrated Tn on one side of the space but failed to provide a resolution that separated the other subpopulations (Figure 4-4). To simplify the trajectory inference problem, we removed Treg (c1) and

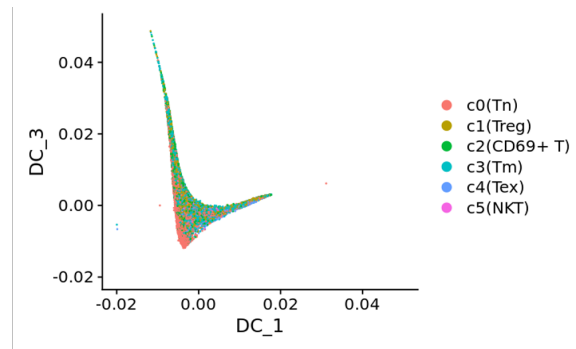


Figure 4-4: Diffusion map of CD4+ T cells.

NKT (c5) from the dataset in the following analyses, since their fates were determined earlier in lymphoid hematopoiesis [82]. With the reduced dataset, we employed *Monocle3*, *CytoTrace*, and RNA velocity to study the differentiation process among Tn, CD69+ T, Tm, and Tex (Figure 4-5A).

With Tn as the root, *Monocle3* inferred a mostly linear trajectory of Tn to CD69+ T to Tm to Tex (Figure 4-5B). *CytoTrace* also inferred a general direction of Tn to Tm pseudotime progression, but ‘late’ cells were detected across Tn, Tm, Tex, and CD69+ T populations (Figure 4-5C). The *CytoTrace*-based transition stream embedding confirmed the general Tn to Tm, Tex, and CD69+ T direction but no clear topology of branching can be extracted from the 2D projection (Figure 4-6A). Using

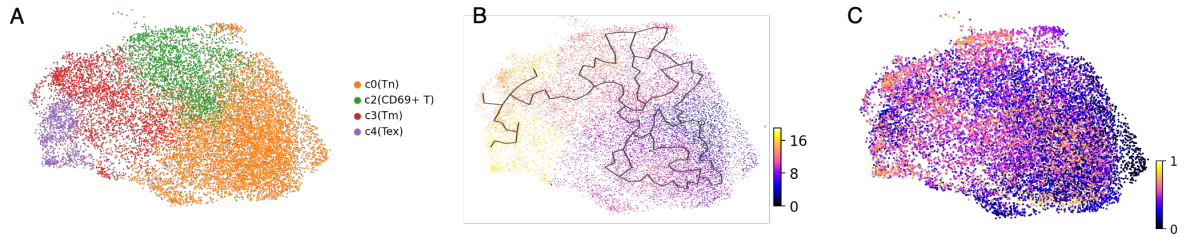


Figure 4-5: Pseudotime inference of CD4+ T cells. A. UMAP plot shows four clusters of CD4+ T cells. B. *Monocle3* inferred pseudotime overlaid on UMAP. Black line indicates the inferred trajectory. Color represents pseudotime. C. *CytoTrace* inferred pseudotime overlaid on UMAP.

Generalized Perron Cluster Cluster Analysis (GPCCA) on the *CytoTrace* transition matrix, we found one initial state in Tn (state 0) and two terminal states in CD69+ T (state 2) and Tex (state 4; Figure 4-6B). With exception of the few cells around terminal state 2, all CD4+ T cells are predicted to eventually transition into the exhausted terminal state 4 (Figure 4-6C). We found the terminal state 2 fate probability strongly correlated with multiple heat shock protein genes (e.g. HSPA6, HSPA1B, HSPA1A), reflecting the phenotype of CD69+ T (Figure A-12).

Finally, leveraging the presence of spliced and unspliced genes, RNA velocity infers a general direction of Tn to CD69+ T transitions with only one terminal state in CD69+ T (Figure 4-7). While *CytoTrace* detected both trajectories of Tn to Tex and Tn to CD69+ T, *Monocle3* only inferred Tn to Tex trajectory and RNA velocity only inferred Tn to CD69+ T trajectory. The deviation of the results indicate that each method could be more adept at detecting different differentiation events.

4.3.3 Tumor-infiltrating CD8+ T cells show universal exhaustion

In the CD8+ T compartment we similarly used *Harmony* to integrate cells from 35 samples and identified clusters through the Louvain clustering algorithm (Figure A-13). After checking the quality of the cells, we found a cluster with high mitochondrial percentage and number of gene features, which are likely doublet cells. With the doublet cells removed, 22,008 cells in 10 clusters remained in the study (Figure 4-

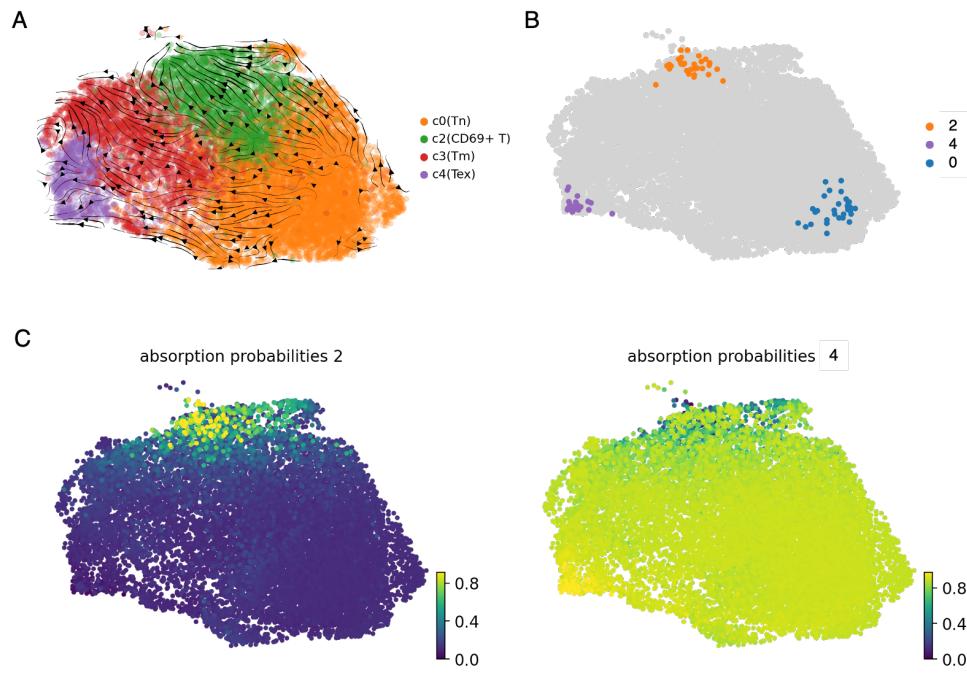


Figure 4-6: Identification of CD4⁺ T cell macrostates by *CytoTrace*. A. *CytoTrace* stream embedding overlaid on UMAP shows inferred differentiation trajectory. B. Macrostates detected by *CytoTrace*. C. Inferred terminal fate probabilities in each cell. Color reflects likelihood of transition into terminal state 2 or 4.

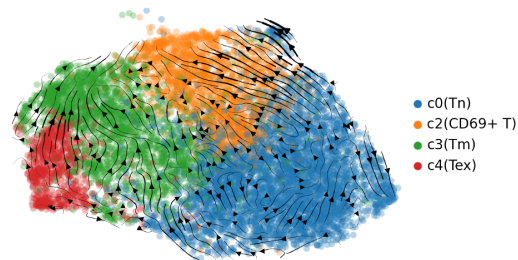


Figure 4-7: CD4⁺ T cell trajectory inference through RNA velocity. Arrows show the RNA velocity field.

8A). Mirroring the CD4+ T compartment, we identified Tn (c3, CCR7+), memory T cells (c0, c1, CXCR6+), and NKT (c6, CD8+XCL2+; Figure 4-8B) [85]. We further separated the memory T cells into effector memory T (Tem, c1) and exhausted memory T (Texme, c0) based on the expression of cytotoxic genes (GZMA, GZMB) and exhaustion marker TOX.

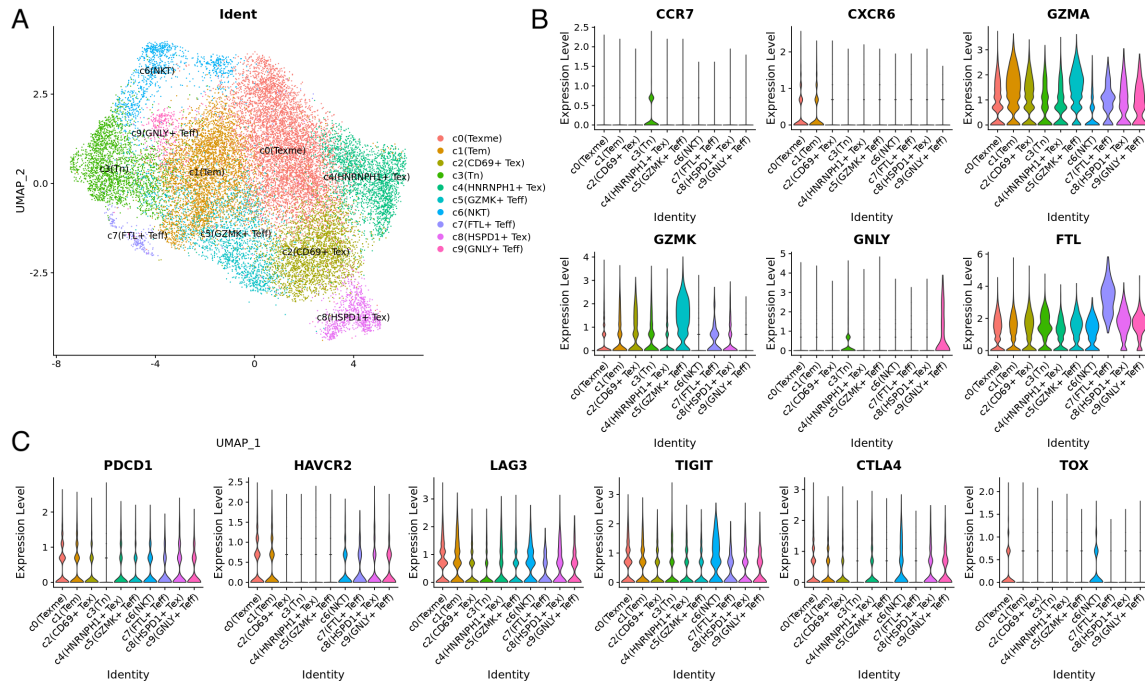


Figure 4-8: Identification of CD8+ T cell subsets. Texme, exhausted memory T cells; Tem, effector memory T cells; Tex, exhausted T cells; Tn, naive T cells; Teff, effector T cells; NKT, Natural Killer T cells. A. UMAP plot shows ten clusters of CD8+ T cells recovered. B. Violin plots show expression of selected signature genes in CD8+ T cell subpopulations. C. Violin plots show expression of selected checkpoint molecule genes.

Cytotoxicity diversity in effector CD8+ T cells

Additionally we identified three clusters of effector T cells (Teff) with moderate to high GZMA and GZMB expressions. GZMK+ Teff (c5) showed a distinct GZMK, GZMH, GZMM and CST7 high signature, suggesting its high cytotoxic potential (Figure 4-9) [94]. GZMK+ Teff are also the only cluster of cells, other than Tn, that does not

express CTLA-4. FTL+ Teff (c7) showed high expression of FTL and FTH1, both genes encode for subunits of the iron storage protein ferritin (Figure 4-9). Although the role of ferritin in T cell effector function has not been thoroughly studied, past study has found FTL and FTH1 highly correlated to infiltration of immune cells overall, and Tregs in particular [95]. Gene set enrichment analysis confirmed FTH+ Teff were enriched in iron homeostasis and secretory granule (Figure A-14). GNLY+ Teff (c9) is the only GNLY expressing cluster other than Tn (Figure 4-8B). GNLY+ Teff showed high expression in S100A10 and S100A11, which encode for calcium binding proteins. In addition to calcium ion binding pathways, GNLY+ Teff also had significant enrichment in collagen containing extracellular matrix (Figure A-14).

Terminally exhausted T cell shows low ribosomal expression

While checkpoint molecules PDCD1, LAG3, TIGIT, and CTLA-4 were detected in almost all clusters, more detailed differential expression analysis revealed three clusters of exhausted T cells (Tex) with different exhaustion and cytotoxicity profiles (Figure 4-8C). CD69+ Tex (c2) had a CD69, FOS, JUN, and HSPA1A high signature, resembling that of CD69+ T in CD4.c2 (Figure 4-9). Similar to CD69+ Tex, HSPD1+ Tex (c8) had high expression of heat shock protein family genes and enrichment in protein folding and heat response related pathways, but unlike CD69+ Tex, HSPD1+ Tex did not express CD69 or FOS/JUN family genes (Figure 4-9, S4-5). HNRNPH1+ Tex (c4) showed a curious profile of high expression of long non-coding RNA (lncRNA) MALAT1, NEAT1, and ribonucleoprotein HNRNPH1, HNRNPU. It is not until recently that studies found lncRNA could epigenetically or post-transcriptionally regulate the T-cell-mediated immune response and contribute to ICI resistance. In particular, pre-clinical studies have confirmed that NEAT1 is able to subvert the cytotoxicity and induce apoptosis in CD8+ T through the miR-155/Tim-3 pathway [96]. Gene set analysis further showed that HNRNPH1+ Tex showed high enrichment in nuclear proteins, RNA splicing, and cell cycle related gene

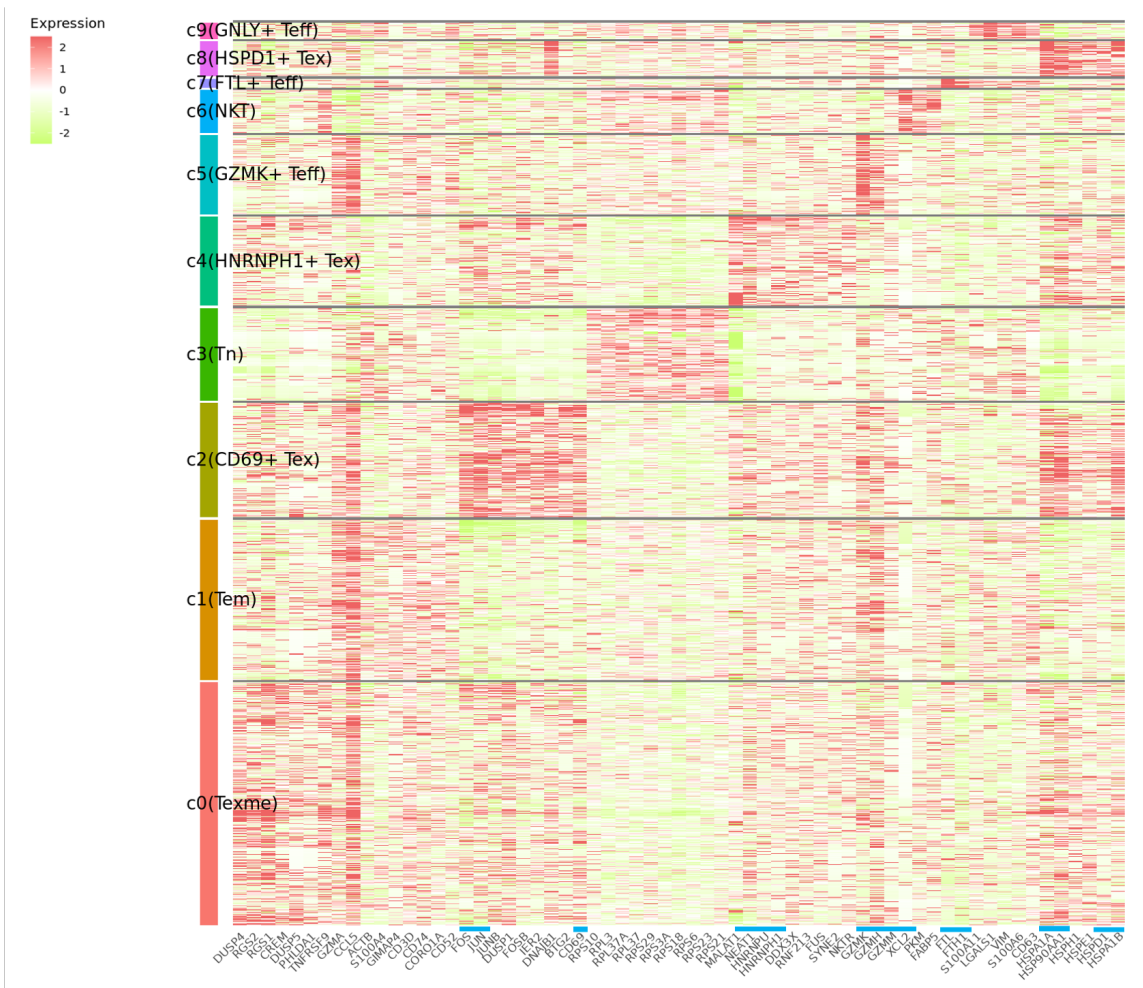


Figure 4-9: Heatmap of top differentially expressed genes across CD8+ T cell subpopulations. Color reflects normalized expression levels.

sets (Figure A-14). While confirming the good quality of these cells in terms of mitochondrial percentage and number of features detected, we noted that HNRNPH1+ Tex had lower ribosomal percentage than all other clusters (Figure A-13B). A similar signature has been reported in terminally differentiated CD8+ T cells in the context of lymphocytic choriomeningitis virus infected mouse study [74]. The authors observed lower amounts of ribosomal mRNA in terminally differentiated effector CD8+ T cells that have stopped dividing just prior to the contraction phase [74]. In the context of exhausted T cells, we recognized HNRNPH1+ Tex as a terminally exhausted state. To our knowledge, this is the first time that this terminally exhausted state with low ribosomal expression is reported in a cancer study.

4.3.4 Inference of CD8+ T cell exhaustion trajectory

We used two pseudotime based algorithms, *Monocle3* and *CytoTrace* to infer the differentiation order of the CD8+ T cells. Both algorithms inferred a generally linear exhaustion progression along UMAP component 1 and a separate branch for NKT (Figure 4-10A, B). Diffusion map also separated the cells to two branches that are concordant to early/late *Monocle3* pseudotime (Figure 4-9C).

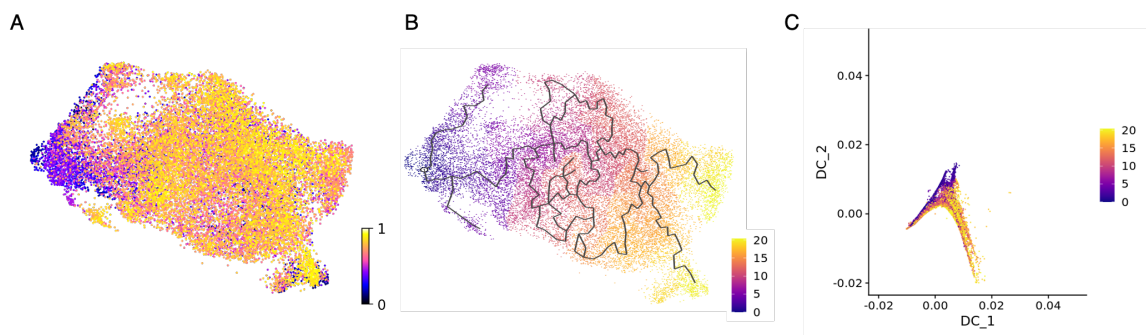


Figure 4-10: Pseudotime inference of CD8+ T cells. A. *CytoTrace* inferred pseudotime overlaid on UMAP. Color represents pseudotime. B. *Monocle3* inferred pseudotime overlaid on UMAP. C. Diffusion map of CD8+ T cells. Color represents *Monocle3* inferred pseudotime.

To gain a finer resolution of the inferred trajectory, we embedded the *CytoTrace* pseudotime and RNA velocity streams on the UMAP. Both methods showed the gradual Tn to Tex to Tex transition (Figure 4-11A,B). Moreover, both methods detected

HNRNPH1+ Tex as the terminal state, agreeing with the terminally differentiated phenotype (Figure 4-11C).

In contrast, *CytoTrace* and RNA velocity detected few transitions between HSPD1+ Tex and other states, hinting that HSPD1+ Tex could be an artificially induced state instead of an *in vivo* biological state in the exhaustion progression. Single-cell technologies rely on the premise of faithful *ex vivo* measurement of cell expression. However, one recent paper reported widespread aberrant *ex vivo* response widespread in brain and peripheral blood scRNA datasets [97](Marsh et al., 2022). This *ex vivo* response shows a signature of high expression in 20 genes including FOS, JUN, HSPA1A, DUSP1, EGR1, and ZFP36. Hypotheses on the induction source of the *ex vivo* response include enzymatic digestion artifacts from dissociation of the cells and prolonged room-temperature exposure during experiment. The study also advised against computational solutions such as removing the cells or regressing the signature to remove the *ex vivo* activation signature, for such solutions could bias the interpretations of true biological state.

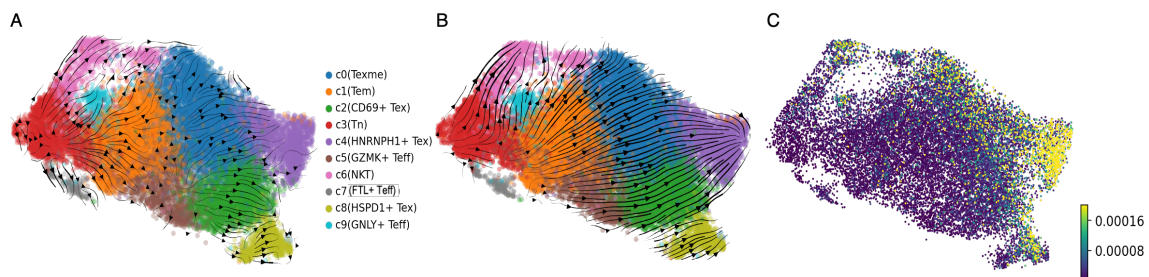


Figure 4-11: Differentiation trajectory of CD8+ T cells. A. *CytoTrace* stream embedding overlaid on UMAP shows inferred differentiation trajectory. B. RNA velocities overlaid on UMAP. Arrows show the RNA velocity field. C. Terminal state probabilities inferred through RNA velocity. Color reflects likelihood of cells in terminal state.

4.3.5 Relating T cell composition to clinical information

T cell composition changes with treatment state

To examine whether treatment state associates with distinct compositions of T cells in the tumor microenvironment, we calculated the fraction of CD4.Tn, CD4.Tex, CD4.Treg, CD8.Tn, CD8.Teff (including CD8.GZMK+ Teff, CD8.FTL+ Teff, and CD8.GNLY+ Teff), and CD8.Tex (including CD8.Texme, CD8.CD69+ Tex, and CD8.HNRNPH1+ Tex) in each sample. To reduce the heterogeneity in treatment group, we focused the analysis on pre-, on-, and post-anti-PD-1 treated samples (n=4,4,5). In both the CD4+ T and CD8+ T compartments we observed the trend that Tn abundance is higher in on-treatment samples than pre- or post-treatment samples (Figure 4-12A, B). Both CD4.Tex and CD4.Treg abundances remained similar across pre-, on-, or post-anti-PD-1 (Figure 4-12A). CD8.Teff abundance appeared to be increasing with the temporal order of pre, on, post state while CD8.Tex decreasing with the temporal order (Figure 4-12B). Aware of the lack of statistical power in small sample sizes, we did not do statistical tests to verify these associations. Other studies have observed a similar trend of increased CD8.Tn, CD8.Tem and reduced CD8.Tex on-treatment [4].

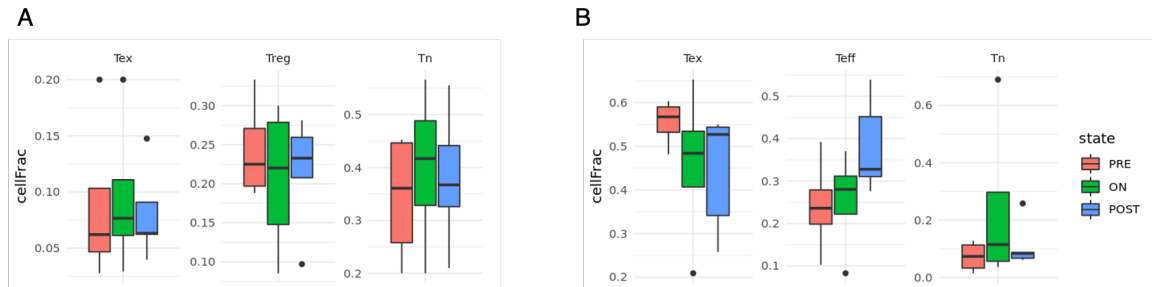


Figure 4-12: T cell compositions across treatment states. A. Boxplot shows frequencies of CD4+ T cell subtypes. B. Boxplot shows frequencies of CD8+ T cell subtypes.

T cell composition associates with survival

We then studied how T cell composition in the pre-treatment tumors could inform us on the clinical prognosis. To increase our sample size, we once again expanded

our analysis to include pre-treatment samples in all treatment groups. Using a linear regression model, we found CD4.Tn and CD8.Tn abundances had positive correlations with progression-free survival (Figure 4-13A,B). These findings are agreed by Zhang et al., which reported anti-PD-1 responders have a higher frequency of naive T cells. Additionally, CD4.Treg, CD4.Tex, and CD8.Tex abundance were found to be negatively correlated with progression-free survival, while CD8.Teff abundance had no association.

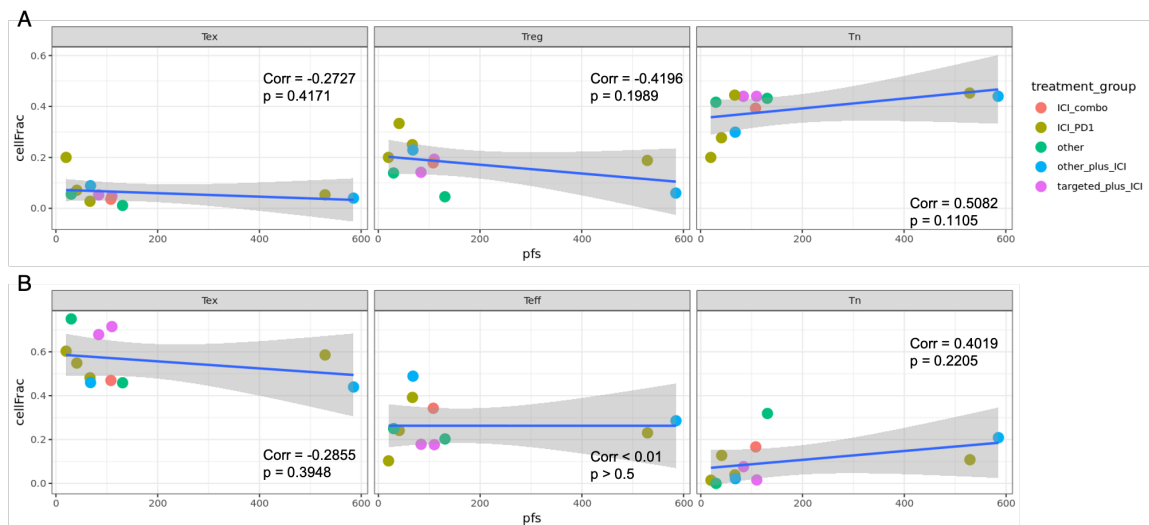


Figure 4-13: Association of progression-free survival and T cell compositions. A. Linear correlation of CD4+ T cell subtype frequencies and progression-free survival. n = 34. B. Linear correlation of CD8+ T cell subtype frequencies and progression-free survival. n = 35.

4.4 Contributions

In this chapter, we looked into the complex tumor immune landscape by analyzing 17,952 CD4+ and 22,008 CD8+ T cell. We successfully identified six subpopulations of CD4+ T cells and ten subpopulations of CD8+ T cells. Using multiple trajectory inference tools, we reconstructed the developmental path of CD4+ T and CD8+ T cells and the transitions between cell states. While most of the T cell subpopulations have been commonly reported in melanoma or other cancers, we identified a CD69+ early activation T cell state and a novel terminally exhausted CD8.HNRNPH1+ Tex

state that have not been studied. Before further biological interpretation of these cell states, we require experimental validation of their presence in tumor tissue. In both CD4+ T and CD8+ T compartments, we found Tn abundances increased with treatment and pre-treatment Tn abundances were associated with better progression-free survival. Finally, although without statistical test, we observed that CD8.Teff levels increased in the course of treatment and continued to rise post-treatment, while CD8.Tex levels decreased.

4.5 Limitations

Although trajectory inference methods have been widely tested, they are not fool-proof. All methods of trajectory inference follow several assumptions [98]: 1. The developmental process of interest is dynamic, 2. The all stages of the developmental process are present, and 3. Transcriptional changes along the developmental process are gradual. In reality, not all biological data follow these assumptions. Most existing methods are better at inferring simple trajectory topologies such as linear or branching, which are also the most common [99]. The rarer and more complicated topologies that include cycles and convergences would impose more challenges to the inference and cannot be handled by all inference methods. Additionally, most approaches adopt a two-dimensional representation or suggest projection onto a two or three dimensional space of choice to assist the visualization of the inferred trajectory. While two dimensional representations are very helpful in capturing the general trend, it is possible that they produce a “distorted flattening” of the high dimensional structure. For this reason, low-dimensional representation of trajectory can be occasionally misleading and should be interpreted with care.

4.6 Methods

4.6.1 Cell type assignment

Based on known cell-type specific markers, we identified tumor cells (MLANA+, PMEL+, S100B+), CD4+ T cells (CD3E+, CD4+), CD8+ T cells (CD3E+, CD8A+, GZMA+), Natural Killer cells (NCAM1+, XCL1+), myeloid cells (CD68+, CD163+), B cells (JCHAIN+, IGHM+), mast cells (CD117+), endothelial cells (CLEC14A+), fibroblasts (DNC+, COL5A1+), keratinocytes (KRT14+) in the dataset. We were able to identify CD4+ T cells in 34 out of 39 samples in the dataset and CD8+ T cells in 35 samples. Then, for each cell type, we performed sample integration, data dimensionality reduction, and clustering as described in Chapter 3 Methods.

4.6.2 Identification of cluster signature genes and pathways

To better characterize the distinct biological functions and states of the T cell clusters, We compared cells in one cluster to all cells in other clusters to identify the cluster signature genes. We used the Wilcoxon test to calculate a p-value for each gene that was expressed in at least 25 percent of cells in either of the two populations and the obtained p-values were subjected to multiple hypothesis adjustment using the Benjamini-Hochberg (BH) method. The test can be carried out with the *Seurat* function *FindMarkers* [78]. Genes with adjusted p.value > 0.01 were considered significant and the top 10 genes with the highest average $\log_2(\text{FoldChange})$ values were used as cluster signature genes.

We also performed Gene Set Enrichment Analysis (GSEA) to investigate the pathway activities in each cluster [48]. For each cluster, all genes are ranked by average $\log_2(\text{FoldChange})$ and used as input for the software *fgsea* (see Chapter 2 Methods). The top 10 pathways with highest positive NES, while satisfying adjusted p value < 0.1 and size > 10 , are considered the signature pathways.

4.6.3 Trajectory inference

The current trajectory inference approaches can be grouped into cluster-based (e.g. *Monocle3*) and graph-based (e.g. Diffusion map, RNA velocity, *CytoTrace*). Both approaches begin with a dimensionality reduction method to compress the dimensions in the gene space. Then, the cluster-based approaches first identify clusters and connect the clusters to a trajectory, while the graph-based approaches first convert the isolated data points (cells) to a similarity graph and organize the connected components to states and trajectory. Finally, both approaches allow projection of inferred trajectory to a low dimensional space for easy visualization.

Diffusion map

The diffusion map algorithm aims to restore the hidden topology of a dataset by first estimating a transition probability matrix on the data points and then performing singular value decomposition on the transition matrix to summarize the topology in eigenvectors [88]. We used diffusion map (implemented by the R package *destiny*) on the *SCTransformed* expression matrices to model the CD4+ T and CD8+ T development trajectory [88]. *Destiny* first calculates the transition probabilities between each cell and its k nearest neighbors based on a Gaussian kernel of width σ to create a sparse transition probability matrix M . The distance between cells can be defined by their transcriptome Euclidean distance, rank correlation, or cosine similarities. Then *destiny* normalizes M by density and performs eigen decomposition to produce the eigenvectors as diffusion components ordered by decreasing eigenvalues. We used the *destiny* suggested k value, which is based on the number of data points, and searched for the optimal σ through the function *find_sigmas* [88]. We compared the diffusion map results using multiple distance metrics before choosing Euclidean distance for all diffusion map figures presented in this thesis.

Monocle3

Monocle3 is a cluster based pseudotime method for inferring cell trajectories [89]. Pseudotime is an abstract unit of progress: it’s the distance between a cell and the start of the trajectory, measured along the shortest path, reflecting how much progress a cell has made through a process such as differentiation. To begin, we divided the cells into large groups based on the UMAP embeddings using the function *cluster_cells*, and learned the principal graph for each group using the function *learn_graph* [89]. The learned graph assigns each datapoint to the nearest principal graph nodes, and we manually choose the root node based on the highest fraction of naive T cells in a node. Using a minimal spanning tree starting at the root, each cell’s pseudotime is calculated as its geodesic distance to the root [89].

RNA velocity

One limitation of *Monocle3* trajectory inference is that it requires a user-specified root node to determine the directionality of the trajectory. As a result, the method is limited to developmental processes with known single initial state. RNA velocity circumvents this problem by inferring trajectory with direction based on the ratio of spliced and unspliced mRNA [98]. The newly transcribed pre-mRNA, containing both intron and exons, undergoes intron splicing to produce the mature mRNA that contains only exons. Based on this principle, cells with high amounts of unspliced transcripts of a gene are expected to have high amounts of spliced transcripts of the same gene in the “future” [81]. The abundance of unspliced (u) and spliced mRNA (s) can be modeled as a deterministic and fully decoupled system of linear differential equations with constant transcription rate α , splicing rate β , and degradation rate γ (Equation 4.1, 4.2) [98].

$$\frac{d\mu_u(t)}{dt} = \alpha(t) - \beta\mu_u(t) \quad (4.1)$$

$$\frac{d\mu_s(t)}{dt} = \beta\mu_u(t) - \gamma\mu_s(t) \quad (4.2)$$

The deviation of observed u/s ratio from inferred steady-state u/s ratio, which

is physically caused by the temporal response delay of splicing pre-mRNA to mature RNA, is termed RNA velocity [99]. This velocity is modeled on each gene and the combined velocity of all genes is used to infer the future state of a cell.

The RNA velocity method consists of two steps: obtain spliced/unspliced matrices and calculate velocities. To call the spliced/unspliced/ambiguous matrices, we used the *velocity* command line interface to align the 10x Chromium .bam output to hg38 transcriptome (downloaded from Ensembl) while masking highly repeated elements identified by the RepeatMasker track on UCSC genome browser [99]. The velocity computation procedures are nicely summarized in the python package *scvelo*, which was used for this project. We started by filtering low readcount cells in the spliced and unspliced gene-by-cell matrices (the ambiguous matrix is discarded) and subsetting the top 2000 most expressed genes. Then, we normalized the counts by the number of reads and log-transformed the splice RNA counts before using PCA reduction. The top-30 PC space were used for finding $k = 30$ nearest neighbors which are pooled to smooth the counts. The smoothed counts are fitted to the systems of ordinary differential equations to estimate the ratio γ/β (Equation 4.1, 4.2). Using the inferred ratio, the velocity v_i for each cell i can be calculated as

$$v_i := \frac{\Delta s_i}{\Delta t} = (\beta \mu_i - \gamma s_i) \propto u_i - \frac{\gamma}{\beta} s_i \quad (4.3)$$

, where Δt is Infinitesimal time increase and Δs is the change is spliced counts over that time. We performed the velocity inference with the function *scv.tl.velocity* in "dynamical" mode. To visualize the velocities, We used the function *velocity_embedding_stream* to map the high-dimensional velocity vectors to stream vectors on the UMAP space.

CytoTrace

CytoTrace is a new, simple, yet robust, framework for predicting trajectory from the transcriptional entropy of scRNA-seq data [86]. Leveraging the number of expressed genes per cell as a developmental potential hallmark, *CytoTrace* generates a dataset-

specific gene counts signature (GCS) that simply averages the expression levels of genes that were most highly correlated with gene counts in the dataset. By one additional step of smoothing GCS based on transcriptional covariance, *CytoTrace* generates a pseudotime that reflects on transcriptional entropy along a differentiation process without prior knowledge of cell lineage or mRNA splicing identification. After filtering, normalizing, and log-transforming the total counts and identifying the highly variable genes, we leveraged the *CytoTraceKernel* function in the python package *Cellrank* to infer the *CytoTrace* pseudotime [86].

4.6.4 Terminal state identification and fate probability estimation

Given the inferred pseudotime or RNA velocity, the python package *Cellrank* enables initial and terminal states identification and fate probability estimation [90]. The *CytoTrace* kernel in *Cellrank* models state transitions using a Markov chain derived from a kNN graph representing cell-cell similarities, where the states represent cellular profiles and edges represent transition probabilities with directions pointing to increasing pseudotime. The function *compute_transition_matrix* generates an extremely large transition matrix, which we projected onto the UMAP space using the function *compute_projection* for easier visualization. To gain more intuition on the state transitions, we sampled cells of early pseudotime and simulated random walks on the transition matrix. Using the Generalized Perron Cluster Cluster Analysis (GPCCA) estimator in *Cellrank*, we summarized the transition state matrix and gene expression profiles into ‘macrostates’, which are phenotypical manifolds that cells are unlikely to leave [90]. When we had no prior knowledge on the expected number of macrostates in the data, we used Schur decomposition to find the ‘eigengap’ and set the number of macrostates to the number of eigenvalues before the gap. To confirm that the macrostates are stable, we used *plot_coarse_T* to compute a coarse-grained transition matrix between them. To remove unstable macrostates that have self-transition probability < 0.96 , we ran *compute_macrostates* with a smaller *n_states* parameter.

The function *compute_macrostates* also uses soft assignment to assign cells a probability of belonging to each state. We named the macrostates as initial or terminal states using knowledge of their transcriptome phenotype or inferred pseudotime. If there are more than one terminal macrostate, We computed each cell’s likelihood of eventually transitioning into each terminal state, which is termed fate probability.

The cell transition matrix can also be computed based on the RNA velocity [90]. The velocity kernel uses RNA velocity as the Markov chain edge directions and uses the number of neighboring cells in the direction of the velocity vector to determine the transition probability. Then the resulting matrix is combined with a second set of transition probabilities computed from transcriptome similarity to generate the final transition probabilities matrix for followed analysis. We computed macrostates, fate probability, and driver genes based on velocity in a similar fashion as in the *CytoTrace* kernel, with one exception that we identified the initial and terminal states by running functions *initial_states* and *terminal_states* [90]. These two functions are only offered by the velocity kernel and can determine the number of initial/terminal states without any user input.

Chapter 5

Conventional dendritic cells bridge adaptive and innate cancer immunity

Besides T cells, a large number of myeloid cells penetrate the tumor microenvironment. The most commonly detected tumor infiltrating myeloid lineages include conventional dendritic cells (cDCs), plasmacytoid dendritic cells (pDCs), monocytes, and macrophages [100]. Traditionally cDCs are divided into two subtypes, cDC1s and cDC2s, with distinctions in surface markers and functionality [16]. Large-scale scRNA-seq studies have identified a new subset of cDCs, namely cDC3s, in melanoma and other cancers [101]. Even before cDC3s were characterized, one study found the density of dendritic cells bearing cDC3-like markers correlated with better survival and clinical outcome in cutaneous melanoma patients [100]. With the objective to further our understanding of cDC3, this chapter has five goals: 1) assess cDC3 association with clinical variables such as treatment group and survival, 2) characterize cDC3 transcriptome using scRNA-seq, 3) study the developmental path of cDC3 and their lineage driver genes, 4) investigate potential cellular interactions between cDC3 and T cells, and 5) evaluate the chromatin landscape of cDC3 to attempt to identify enriched peaks and motifs.

5.1 Background

Single cell studies discover the novel cDC3 state

cDCs are traditionally divided into cDC1 and cDC2, with more possible subdivisions within each subtype. Distinguished by a $XCR1^+Cadm1^+CD172a^-$ marker set, cDC1 has a preference for MHC class I cross presentation of antigen to induce $CD8^+$ T cell activation. On the other hand, $XCR1^-Cadm1^-CD172a^+$ cDC2 is commonly thought to specialize in MHC class II presentation and activate $CD4^+$ T helper cells and Tregs, in addition to interacting with $CD8^+$ T cells [102]. A newer subset of cDC, namely cDC3, has been reported in the more recent scRNA-seq cancer studies [100]. Transcriptomically characterized as $LAMP3^+CCR7^+$, the tumor-infiltrating DC3 state is found exclusively in tissue. Due to their recent emergence in the field, cDC3 is also named tumor-infiltrating $LAMP3^+$ DC, $CCR7^+$ DC, and mature DC enriched in immunoregulatory molecules (mregDCs) in some publications [15]. Although transcriptomically distinct from cDC1 and cDC2, CITE-seq experiments (Cellular Indexing of Transcriptomes and Epitopes sequencing) have found that cDC3s express cDC1 (e.g., $XCR1$, $CD103$) or cDC2 associated proteins (e.g. $CD11b$). These findings suggest that cDC3 could be a dendritic cell state that supersedes the lineage differences between cDC1 and cDC2 [15].

A recent pan-cancer single cell study identified the two classical $CLEC9A^+$ cDC1 and $CD1C^+$ cDC2 subsets, and a $LAMP3^+$ cDC3 subset with mature phenotype in all 15 cancer types analyzed with various proportions [100]. The study found $LAMP3^+$ cDC3 to have high expression of maturation markers, regulatory molecules, and migratory genes, as well as low expression of Toll-like receptors. From trajectory analysis using *Monocle2* and *CytoTrace*, the study found $LAMP3^+$ cDCs originated from both cDC1 and cDC2. Additionally, the study subdivided $LAMP3^+$ cDCs from different origins using *SingleR*, which mainly relied on gene expression Spearman coefficients with the reference dataset. The study found more cDC1-derived cDC3s in almost all cancer types (nearly 80% cDC3 in melanoma samples were cDC1-derived), despite more cDC2 cells being found in the tumors. Differential expression analysis

found cDC1-derived cDC3s had much higher expression of BTLA and IL12B, which is a cytokine that could induce the differentiation of T helper 1 (TH1) cells. On the other hand, cDC2-derived LAMP3+ cDCs showed high expression of CD1E and CCL17, a chemokine that could recruit CCR4+ Treg to create an immunosuppressive environment in the tumor [100]. These findings suggest that the two cDC3 subsets could still maintain distinct transcriptomic properties and functions after converging to the cDC3 cell state.

Potential for cDC3-T cell interaction

With the knowledge that chemokine ligands of CCR7 guide egress trafficking to lymph nodes, it is hypothesized that cDC3 would migrate to draining lymph nodes, where they may activate tumor antigen-specific T cells. In an anti-PD-1 treated mouse xenograft study, Garris et al., 2018 reported cDC3 was enriched at locations close to blood vessels, suggesting their potential for migration. Moreover, the study reported a positive feedback of IFN- γ and IL-12 crosstalk between cDC3 and CD8+ T cells that could lead to a full-fledged anti-tumor immunity. Although the interaction between cDC3 and T cells has been less studied in human tumors, immunohistochemistry staining of colorectal cancer patient tumor confirmed physical juxtaposition of cDC3 and multiple T cell types, suggesting room for cDC3-T cell crosstalk [103].

5.2 Research approach

Using the same scRNA-seq cohort as in Chapter 4, we used markers suggested by previous studies to identify the cDC subpopulations and focused on cDC3. We performed clinical correlation study using Pearson correlation and linear regression, and differential expression analysis as described in Chapter 4 methods section. To study the developmental path of cDC3, we used *CytoTrace* and RNA velocity to infer their trajectory. Finally, we employed the *CellPhoneDB* database to inquire the potential cell-cell-interactions between cDCs and subpopulations of T cells identified in the previous chapter.

5.3 Results and discussions

5.3.1 scRNA-seq reveals cDC3 transcriptomic profile

Consistent with other melanoma studies, we identified four major cell types within the myeloid compartment: pDCs (LILRA4+ IL3RA+), cDCs (FLT3+, FCER1A+), monocytes (FCN1+, FCGR3A+), and macrophages (C1QA+, IL1B+; Figure 5-1). Within the macrophage and monocyte clusters, we observed a slight separation of cells by tissue of origin due to the presence of niche-specific tissue-resident macrophages (Figure A-15). Nevertheless, 2160 cDCs were identified in 38 samples and were well-integrated when subsetted to study in isolation (Figure A-16).

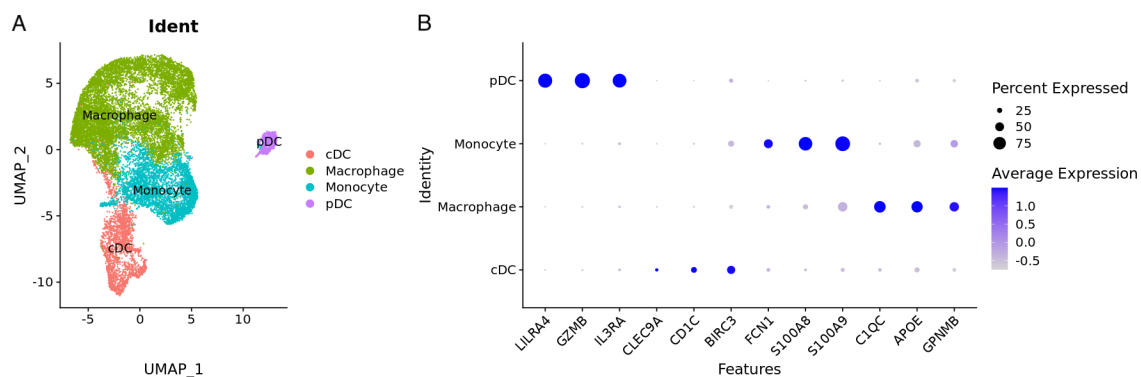


Figure 5-1: Identification of myeloid cell subsets. A. UMAP plot shows the major lineages of myeloid cells in melanoma. B. Dot plot shows expression levels of selected signature genes in different myeloid cell subsets. Dot size indicates fraction of expressing cells, color reflects normalized expression levels.

By clustering the cDCs at a finer resolution, we recovered the two standard CLEC9A+XCR1+ cDC1 and CD1C+FCER1A+ cDC2 subtypes, as well as the novel LAMP3+CCR7+ cDC3 (Figure 5-2A). Differential expression analysis revealed a distinct cDC3 signature, which included high expression of apoptosis inhibitor BIRC3, Lysosome-associated membrane glycoprotein 3 (LAMP3), dendritic cell maturation marker C-C Motif Chemokine Receptor 7 (CCR7), and immunoregulatory C-C Motif Chemokine Ligand 19 (CCL19; Figure 5-2B) [104]. In total, 419 cDC3-enriched DEGs were detected and an extended signature panel is shown in Figure 5-2C.

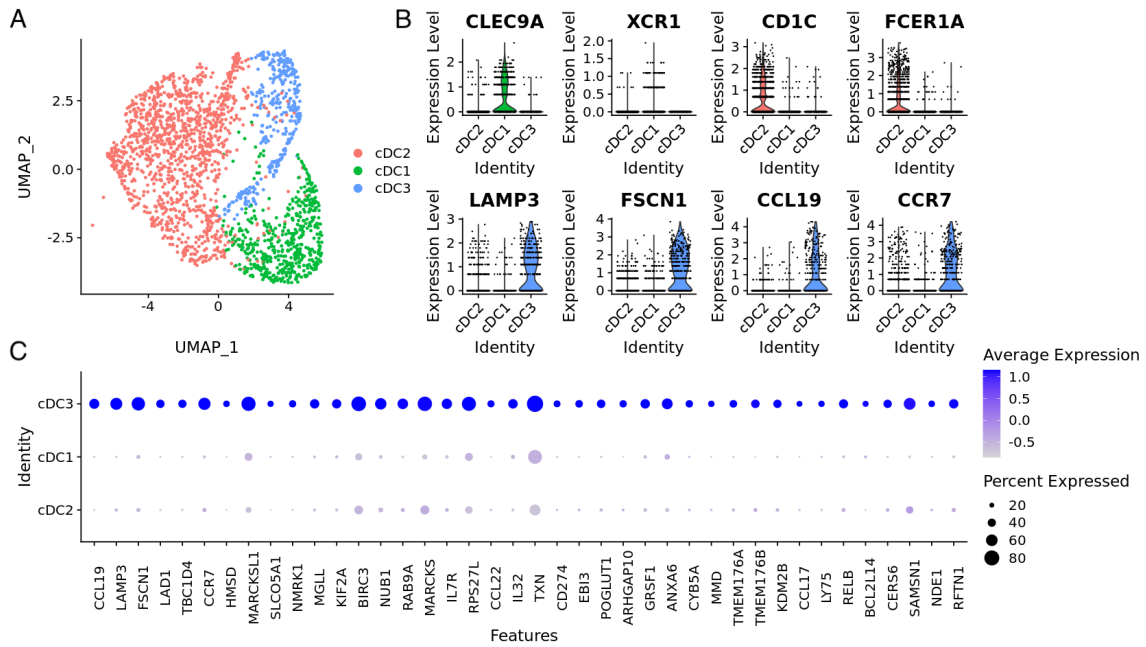


Figure 5-2: Transcriptomic characterization of cDC3 in melanoma. A. UMAP plot shows the three major subpopulations of cDC in melanoma. B. Violin plots show expression of cDC subpopulation signature genes. C. Dot plot shows expression of extended cDC3 signature genes. Dot size indicates fraction of expressing cells, color reflects normalized expression levels.

5.3.2 cDC3 abundance predicts progression-free survival

In a 2015 study, the serum concentration of CCL17, which we now know as a cDC3 signature expression, was found as a powerful predictor of favorable overall survival in metastatic melanoma [105]. Using our cohort of various treatment groups and states, we observed a strong correlation of cDC3 proportion and progression-free survival in both pan-treatment cohort and anti-PD-1 treated subsets (Figure 5-3A,B). Furthermore, we stratified the samples into cDC3_level_high and cDC3_level_low groups. Using the Wilcoxon test, we confirmed the survival benefit of high cDC3 abundance ($p = 0.077$, Figure 5-3C). When restricting the analysis to anti-PD-1 treated samples to reduce cohort heterogeneity, the association was found to be even stronger ($p = 0.018$; Figure 5-3D). Limited by sample size, we did not perform the same analysis on other immunotherapy or non-immunotherapy treated samples.

5.3.3 Differentiation trajectory of cDC3 state

Trajectory inference using *CytoTrace* successfully re-established that cDC1s and cDC2s converge to the cDC3 state (Figure 5-4A) while RNA velocity failed to infer the correct developmental direction (Data not shown). While previous literature reported higher abundance of cDC1-derived cDC3 than cDC2-derived cDC3, we found more cDC2s to have high probability of transitioning into cDC3 terminal state (Figure 5-4B). By correlating gene expression and inferred probability of transitioning into cDC3 state, we found several potential cDC3-fate driver genes including PPP1R14A, GRASP, and CFP (Figure A-17). After extensive literature search, we found very few studies on our identified potential cDC3-fate driver genes in the context of dendritic cells. Further investigation of the cellular functions of these genes should be conducted before making claims on their role in cDC3 differentiation.

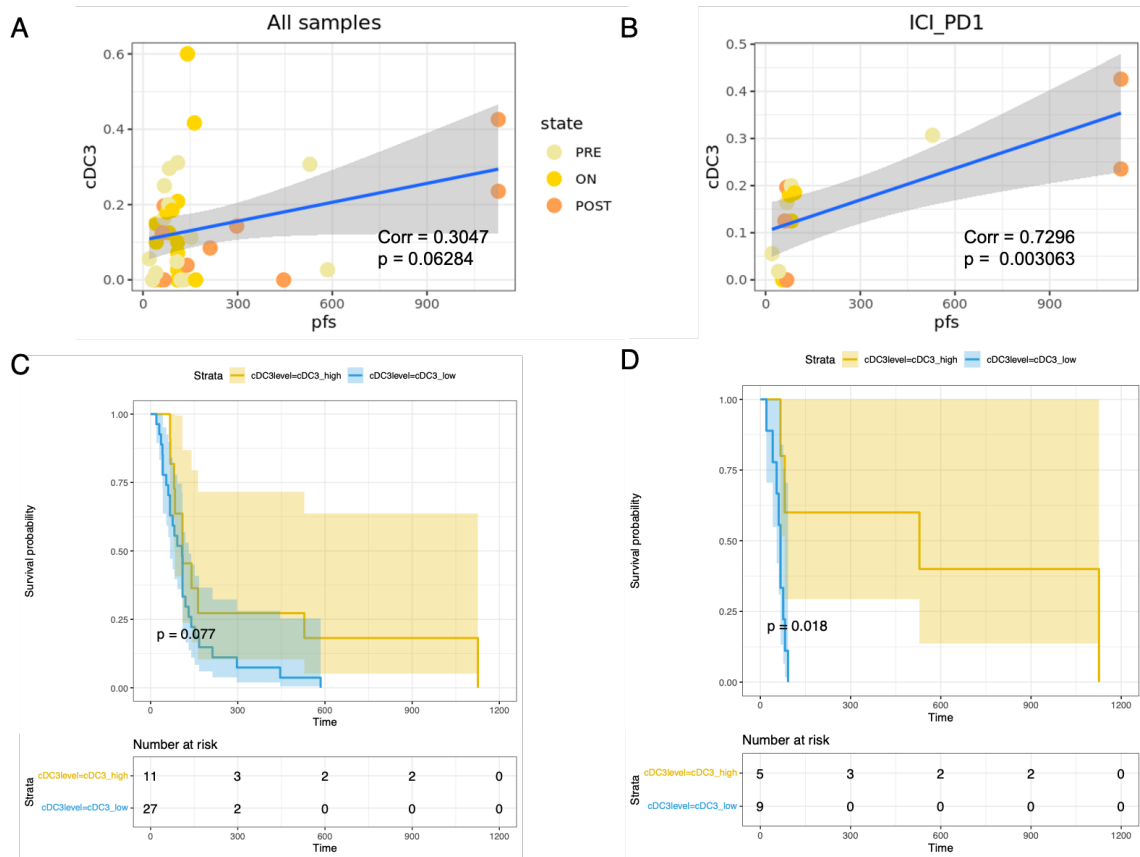


Figure 5-3: Developmental trajectory of cDC subpopulations inferred by *CytoTrace*. A. *CytoTrace* stream embedding overlaid on UMAP shows converging transition paths from cDC1 and cDC2 to cDC3. Arrows show state transition directions. B. cDC3 fate probability of each cell. Color reflects likelihood of transition into cDC3 macrostate. Pearson correlation.

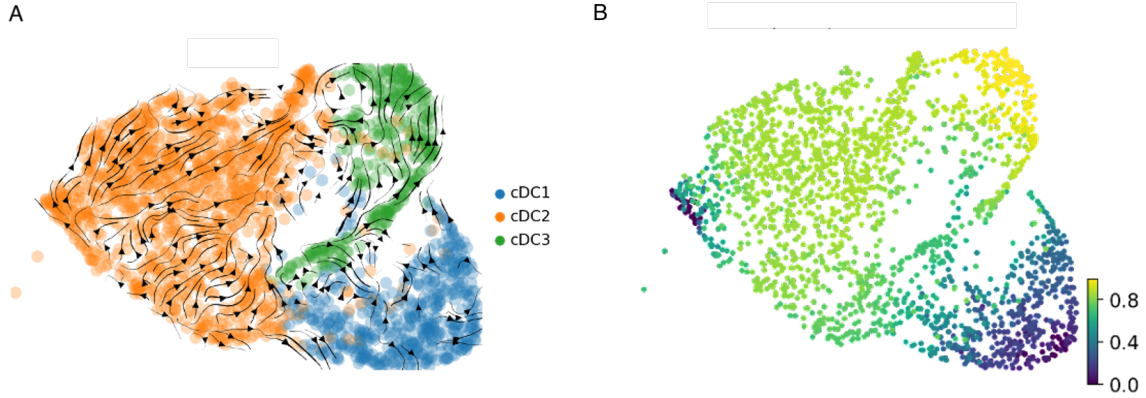


Figure 5-4: Association of progression-free survival and cDC3 frequency. A. Linear correlation of cDC3 frequency and progression-free survival across all treatment groups. $n = 38$. Time in days. Pearson correlation. B. Linear correlation of cDC3 frequency and progression-free survival in anti-PD-1 treated samples. $n = 14$. C. Survival plot across all treatment groups stratified by cDC3 frequency. cDC3_high group defined as $> 20\%$ cDC3 in cDC. Willcoxon test. D. Survival plot of anti-PD-1 treated samples stratified by cDC3 frequency.

5.3.4 NF- κ B and KLF3 transcription factors regulate cDC3 state

The cell transcriptome is an orchestration of regulatory networks where a limited number of transcription factors and co-factors regulate each other and their downstream genes. To study the regulatory networks underlying cDC states, we employed *SCENIC* (Single-Cell rEgulatory Network Inference and Clustering) to uncover regulations specific to the cDC3 state. We observed several regulons in the Rel/NF- κ B transcription factor family, including REL, NFKB1, and NFKB2, had high specificity in cDC3 (Figure 5-11). Additionally, a recent mouse study reported that Krüppel-like factor 3 (KLF3) engages in a feedback inhibition of NF- κ B subunit RELA expression in inflammatory monocytes [106]. While this interaction is yet to be confirmed in human cDCs, enriched activity of both KLF3 and NF- κ B transcription factors may reflect a highly dynamic regulation of the cDC3 state.

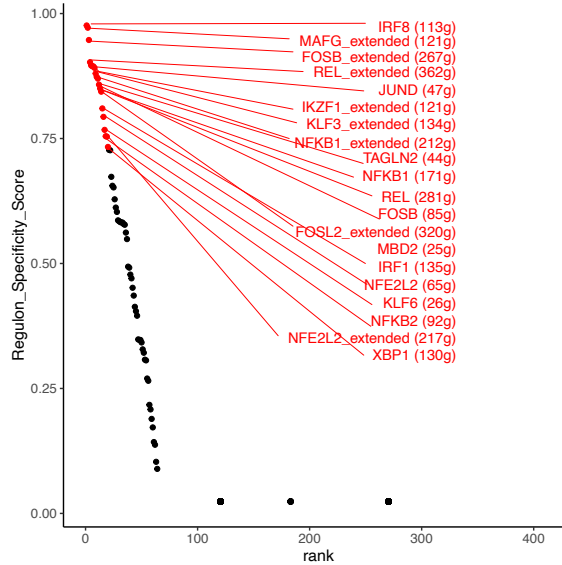


Figure 5-5: Scatter plot of cDC3 regulon specificity scores inferred by *SCENIC*. Top 20 regulons are highlighted.

5.3.5 cDC3 influences T cell homing and activation

Correlation of tumor-infiltrating cDC3 and T cell frequencies

Reflecting on previous studies, we hypothesized an association between cDC3 and T cells [103]. For the first time to our knowledge, we confirmed a significant correlation between cDC3 and CD8+ T cell tumor infiltration in on-treatment samples from the single-cell point of view (Cor = 0.5363, p-val = 0.04806; Figure 5-6A). No significant correlation of cDC3s and CD8+ T infiltration was found in pre- or post-treatment samples, suggesting such coordination between cDC3 and CD8+ T could be induced by treatment. We also found a positive correlation between the on-treatment cDC3 and CD4+ T infiltration (cor = 0.4173, p-val = 0.1377; Figure 5-6B).

Predicting cDC3-T cell interactions through *CellPhoneDB*

Leveraging the ligand-receptor databank *CellPhoneDB*, we next investigated the potential molecular interactions that are specific between cDC3 and T cells. With the knowledge that cDC3 expressed significantly higher levels of lymphoid chemokine CCL19, we found high interaction potential between CCL19 and receptors CCR7

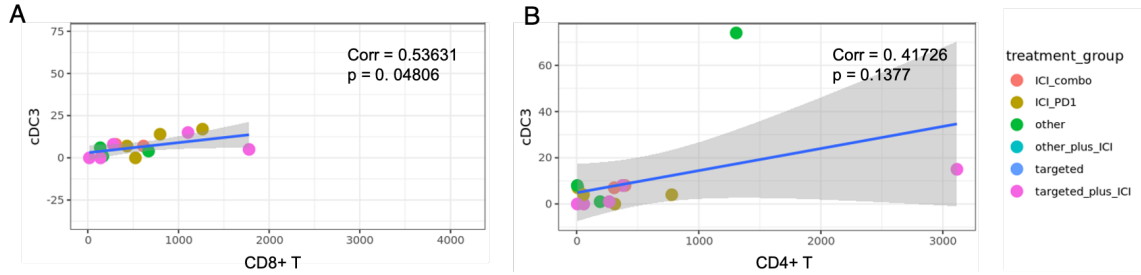


Figure 5-6: Scatter plot of cDC3 and T cell abundances in on-treatment melanoma. $n = 34$. A. Linear correlation of cDC3 and CD8+ T cell abundances. B. Linear correlation of cDC3 and CD4+ T cell abundances. $n = 35$. Pearson correlation.

and CXCR3 expressed on both CD4+ and CD8+ T cells (Figure 5-7A,B). Compared to cDC1s and cDC2s, cDC3s also had more CD4+ T cells homing potential through the CCL22-CCR4 interaction [107]. All these potential interactions indicated cDC3s' ability to recruit T cells to the tumor. Interestingly, we also detected ex-

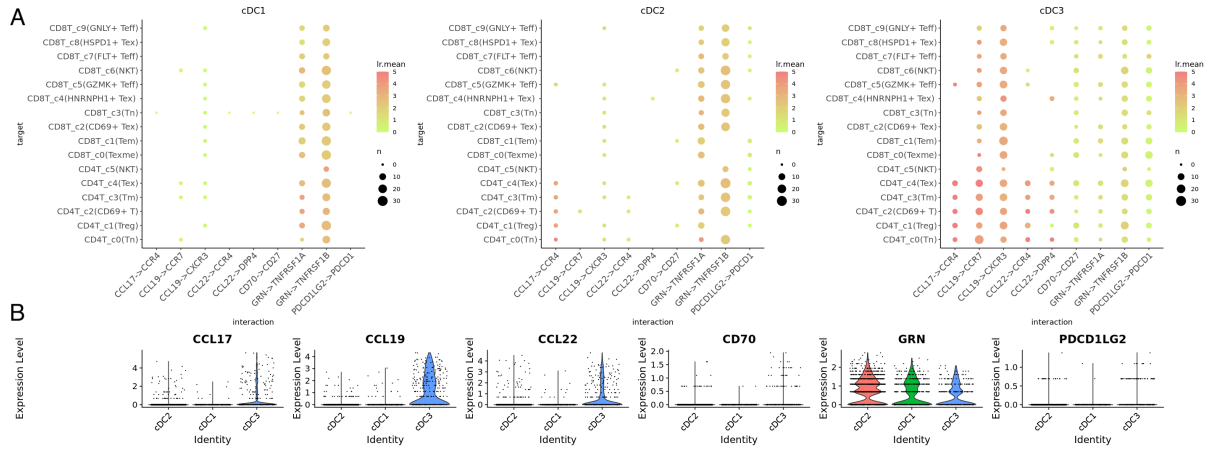


Figure 5-7: cDC-T cell interactions predicted by *CellPhoneDB*. A. Dot plots show selected statistically significant interactions between cDC and T cell subpopulations. Dot size indicates the number of samples in which the interaction was found to be statistically significant, color reflects average strength of interaction across samples. B. Violin plots show expression of the selected ligand in respective cDC subpopulations.

pression of chemokine-degrading dipeptidyl peptidase DPP4 on most CD4+ T and a few CD8+ T cell states (Figure 5-7A). By truncating CCL22 at the N-terminal, DPP4 restrains T cells' chemotactic behavior toward cytokines [108]. Among all the

T cell populations, we found CD4.c4 (KLRB1- Tm), CD8.c3 (Tn), CD8.c5 (GZMK+ Teff), CD8.c1 (Tem), CD8.c2 (CD69+ Tex), CD8.c6 (NKT) expressing CCR4 but not DPP4, suggesting their uninhibited chemotactic ability in response to CCL22. Additionally, we found cDC3 equipped with CD70 and the potential to interact with T cells through the T cell co-stimulatory CD70-CD27 axis (Figure 5-7A,B). Together with the pMHC-TCR signal, the co-stimulatory CD27 molecule can induce T cell clonal expansion and effector differentiation [109]. On the other hand, cDC3 also expressed PDCD1LG2, which encodes PD-L2, and could inhibit T cell activation through the PD-L2-PD-1 (PDCD1LG2-PCCD1) interaction. Prediction of both co-stimulatory and co-inhibitory interactions with T cells suggested a dynamic role of cDC3 in priming T cells for tumor-killing or immune regulation.

When studying the T cell ligand to cDC3 receptor interactions, we found lower expression and interaction potential of CD74, HLA-DPA1, HLA-DPB1 in cDC3s (Figure 5-8). We recognized the down-regulation of antigen-processing as a feature of cDC maturation, as they switch out of the antigen capturing mode [106].

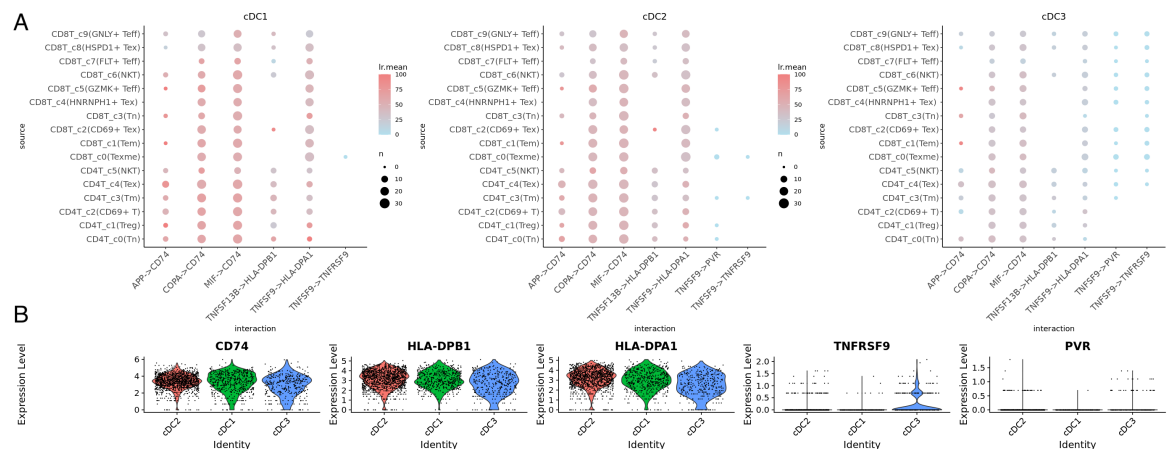


Figure 5-8: T cell-cDC interactions predicted by *CellPhoneDB*. A. Dot plots show selected statistically significant interactions between T cell and cDC subpopulations. Dot size indicates the number of samples in which the interaction was found to be statistically significant, color reflects average strength of interaction across samples. B. Violin plots show expression of selected receptors in respective cDC subpopulations.

5.3.6 snATAC-seq evaluates open chromatin regions and motifs enriched in cDC3

To further understand the transcription regulation of cDC3s, we evaluated their chromatin landscape using snATAC-seq. After QC we retained 45478 snATAC-seq cells from 15 samples, all of which had matched scRNA-seq data of the same tumor (Figure 1-1). With a combination of known markers and label transfer from scRNA-seq, we identified 12 cell types, including cDC (Figure A-18).

To further distinguish the cDC subpopulations, we integrated and co-embedded the snATAC-sequenced cDCs and scRNA-sequenced cDCs using canonical correlation analysis (CCA) [78]. We adopted the snATAC-seq cell with cDC subpopulation labels from their mutual nearest neighbors in the scRNA-seq dataset (Figure 5-9).

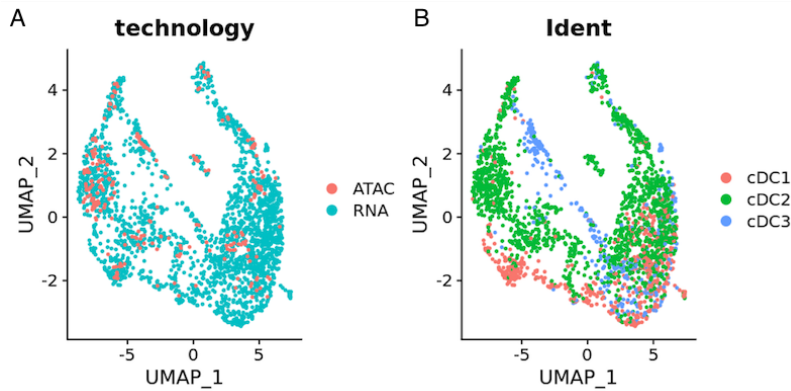


Figure 5-9: Integration of snATAC-seq and scRNA-seq detected cDCs. A. UMAP plot includes 2160 scRNA-seq cells and 235 snATAC-seq cells. B. UMAP plot shows canonical correlation analysis (CCA) inferred cDC subpopulation labels.

Using differential peak analysis, we found 44 peaks that were significantly enriched in cDC3 cells ($p < 10^{-5}$) and annotated them with the closest gene, 6 of which were also differentially expressed in scRNA-seq ($p.\text{adj} < 0.001$) and 2 were included in the cDC3s signature panel (FSNC1, CCR7; Figure 5-10). The most significant peak was in the intronic region of lysine-specific demethylase 2b (KDM2B), which encodes a histone demethylase targeting H3K36me2 and H3K4me3 [110]. While generally associated with epigenome reprogramming for cell-cell adhesion and migration, the role of KDM2B in cDCs remains to be elucidated [111].

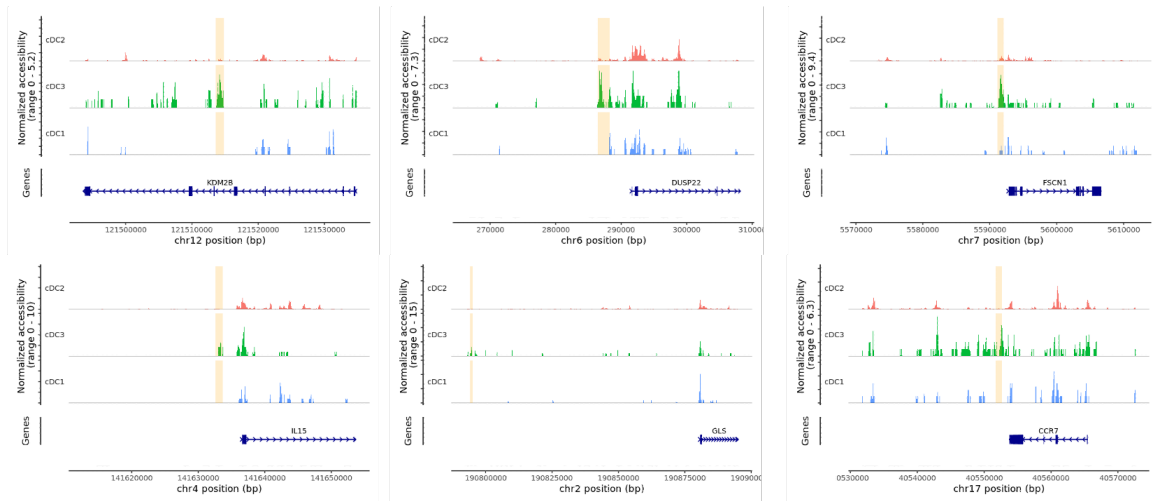


Figure 5-10: Chromatin accessibility profiles of cDC3 in melanoma. Genome tracks show cDC3 differentially accessible peaks ($p < 10^{-5}$, yellow regions) near differentially expressed genes identified in scRNA-seq analysis ($p.\text{adj} < 0.005$). Blue bars represent the gene.

snATAC-seq confirms Rel/NF-kB transcription factors as master a regulator of cDC3 state

We further extracted the position and frequency of motifs in each cDC3 enriched peak region ($p < 0.005$) and identified 111 motifs enriched in cDC3 ($p < 0.001$). Rel/NF-kB and KLF/SP transcription factor (TF) families were again found among the top motifs, confirming the findings from gene regulatory network inference (Figure 5-11). NF-kB TFs are known to control genes encoding proteins essential to the adaptive immunity, such as MHC class I and II, co-stimulatory signal CD80/CD86, cytokines and receptors, or cell adhesion molecules [106]. In the context of APCs, we recognize NF-kB TFs as a master regulator for cDC3's ability in T cell co-stimulation and activation.

5.4 Contributions and future steps

In this chapter we conducted an in-depth study of the LAMP3+CCR7+BIRC3+CCL19+cDC3 state dendritic cells. The strong association of cDC3 abundance and progression-

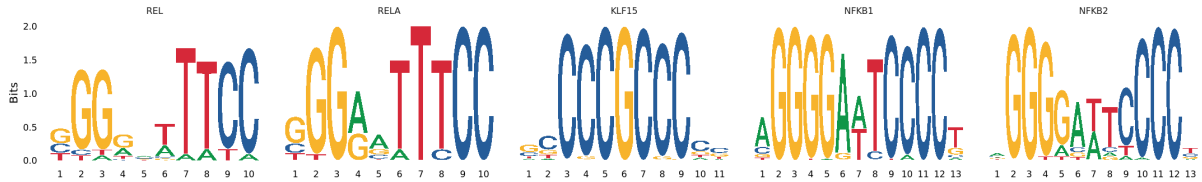


Figure 5-11: Sequence logo plot of selected motifs enriched in cDC3.

free survival highlights the clinical potential of using cDC3 as a prognosis marker. After finding significant correlation of cDC3 and CD8+ T cell infiltration, we hypothesized direct cDC3 and T cell interaction in the tumor microenvironment. Based on the *CellPhoneDB* data bank, we found several potential interactions specific to cDC3 and T cells that could contribute to T cell homing (e.g. CCL19-CCR7, CCL19-CXCR4) and activation (e.g. CD70-CD27). We confirmed that cDC3 cells differentiated from both cDC1s and cDC2s through trajectory inference and identified Rel/NF- κ B TF family as a master regulator of cDC3 state through gene regulatory network inference. Using snATAC-seq, we confirmed that Rel/NF- κ B family motifs were enriched in open chromatin regions in cDC3s.

In a contextualized learning project in collaboration with B. L., we again independently arrived at the finding that cDC3 abundance is highly predictive of progression-free survival (results not shown). To fully harness cDC3's clinical potential, we propose to leverage deconvolution methods to separate cDC3s from bulk RNA-seq and confirm their association with survival in large cohorts. Moreover, inspired by our finding that BIRC3 was strongly associated with responders in both pan-ICI and pre anti-PD-1 cohorts (Chapter 2), we would inspect other cDC3 markers for their response association in published datasets. In the meantime, we would also like to validate cDC3's presence in the draining lymph nodes and their molecular interaction with T cells through *in vitro* co-culturing or tumor sample immunohistochemistry. If we are able to experimentally demonstrate that cDC3s enter lymph nodes and prime naive T cells, it would be likely that the increased infiltration of naive T cells during on-treatment, reported in Chapter 4, is facilitated by cDC3.

5.5 Methods

5.5.1 Identification and scRNA characterization of cDC3s

To start, we identified myeloid cells (CD68+, CD163+) from the study cohort using known cell-type specific markers. We performed sample integration, data dimensionality reduction, and clustering as described in chapter 1 methods section to further classify the myeloid cells into pDCs (LILRA4+ IL3RA+), cDCs (FLT3+, FCER1A+), monocytes (FCN1+, FCGR3A+), and macrophages (C1QA+, IL1B+). We then subsetted the cDCs and repeated the dimensionality reduction and clustering to separate them into cDC1s (CLEC9A+ XCR1+), cDC2s (CD1C+ FCER1A+), and cDC3s (LAMP3+ CCR7+). We further characterized cDC3s transcriptome through differential expression analysis as previously described.

5.5.2 Trajectory and fate-driver gene inference

We inferred the developmental path of cDCs using *CytoTrace* and RNA velocity. We identified terminal state and estimated fate probability as described in Chapter 4 methods section. Finally, to find the potential driver genes of each fate, we correlated fate probability against all gene expressions and studied the top genes of highest correlation and lowest p-value.

5.5.3 Cell-cell-interaction prediction

Cell-cell-interactions begin with binding of a secreted or surface ligand from source cell to its receptor on the target cell. Subsequently the receptor sends down a signal that induces cellular response in the target cell. Identification of the ligand-receptor interactions would help us begin to understand the dynamic intercellular communications in the highly complex tumor microenvironment. scRNA-seq can simultaneously and quantitatively measure the expression of ligands or receptors across multiple cell types. *CellPhoneDB* is a repository of 1400 ligand-receptor interactions that includes a statistical tool that tests cellular interactions between two cell groups of scRNA-seq

data [112]. The strength of interaction of a ligand-receptor pair between two cell groups are derived from the mean expression of the ligand on one group and the receptor on the other group. If the ligand or receptor gene encodes for a subunit of a complex, the gene in the complex with lowest average expression is used for the interaction strength calculation. *CellPhoneDB* calculates the p value for a given ligand-receptor pair by a permutation test, where the source and target cell labels are randomly permuted and the simulated expression strength are calculated to generate the null distribution [112]. The likelihood of simulated strength being greater than the true interaction strength is considered the p value. For easier visualization of the result, we used the *liana_wrap* function offered by the R library *LIana* to run *CellPhoneDB* algorithm with *method* = 'cellphonedb', *resource* = 'CellPhoneDB', and *nperms* set to 10,000 [113].

5.5.4 Regulatory network inference with *SCENIC*

We analyzed the activated regulatory networks in cDC1, cDC2, and cDC3 subsets with *SCENIC* [114], which consists of three steps. Starting with the raw count matrix as input, we used *GRNBoost2* to find regulatory networks, which are sets of genes co-expressed with transcription factors. To remove false positives and indirect targets, we pruned the networks using *RcisTarget*, which identifies direct-binding targets with motif enrichment of the correspondent upstream regulator. Finally, we used *AUCell* to compute the regulon activity score (RAS) in each cell based on the ranked expression value of genes in the regulon [114]. To select regulons specific to cDC3s, we calculated the regulon specificity score, which reflects the entropy of RAS in cells across cDC subpopulations, for each detected regulon. The regulon specificity score ranges from 0 to 1, with a higher value indicating more specificity of the regulon.

5.5.5 snATAC-seq data generation and preprocessing

L.H. and K.G. performed scATAC-seq using the Chromium single cell ATAC v1 chemistry from 10x Genomics with the target of 5000 nuclei per sample. Then the libraries

were profiled using the Novaseq S2 (Illumina) technology. We aligned and quantified the libraries using the 1x cellranger-atac-2.0.0 pipeline. For quality control, we kept cells with peak region fragments between 5000 to 20,000 nucleotides, transcription start site enrichment score > 4 , and percent reads in peaks $> 20\%$. We quantified the activity of each gene in the genome using the *GeneActivity function* in *Signac*, which sums the fragments in the gene body coordinates including 2 kb upstream region, according to Ensembl annotation EnsDb.Hsapiens.v86 [115]. For dimensionality reduction, we perform term frequency inverse document frequency (TF-IDF) normalization and singular value decomposition (SVD) on the peak-by-cell matrix. To visualize the dataset in 2-dimensions, we performed UMAP using the top 50 components and used graph-based clustering to find clusters. With a combination of known markers and label transfer from scRNA-seq data, we assigned cell labels to each snATAC-sequenced cell.

5.5.6 Integration of snATAC-seq and scRNA-seq data

To integrate the snATAC-seq profiles with scRNA-seq profiles, we used *FindIntegrationAnchors* in *Signac* to identify co-varying components of the snATAC-seq and scRNA-seq datasets. Then we leveraged canonical correlation analysis (CCA) to co-embed cells from both the transcriptomic and epigenomic space using the identified canonical ‘basis’ vectors [78]. The co-embedding in shared lower-dimensional space maximizes correlation between the two datasets, thus allowing joint analysis and cell-typing of scRNA-seq and snATAC-seq datasets. After subsetting cDCs from both snATAC-seq and scRNA-seq datasets, we repeated the integration process and assigned the snATAC-seq cells with cDC subpopulation labels from their mutual nearest scRNA-seq neighbors in the shared space.

5.5.7 Differentially accessible peaks and motif enrichment analysis

To find differentially accessible regions in cDC3s, we tested for differential accessibility using logistic regression while accounting for total number of fragments to remove sequencing depth influence. Due to the high drop-out rate and sparsity of snATAC-seq data, we tested all peaks detected in at least 5% of cDC3 cells and annotated them by the closest gene. We considered peaks with $p < 10^{-5}$ as significantly different. Then, using the motif position frequency matrices reference from *JASPAR2020* database, we searched for DNA motifs overrepresented in all cDC3 enriched peaks with $p < 0.005$. The motif enrichment analysis was performed using the *Signac* function *FindMotifs* [115].

Chapter 6

Conclusion

6.1 Summary of research contributions

This study has advanced our understanding of the melanoma microenvironment in the context of immune checkpoint inhibitor therapy. In Chapter 2, we identified potential marker genes for ICI response (e.g. CD226 and BIRC3) and resistance (e.g. AFF3 and CDCA7) through differential expression analysis of bulk RNA-seq. In Chapter 3, we confirmed adequate immune infiltration in progressive disease both pre- and on- treatment, through deconvolved bulk RNA-seq and scRNA-seq. Moreover, we made the observation of tumor properties that are similarly (e.g. bioenergetics) or differentially (e.g. cell adhesion) affected by ICIs in responders and progressors. Identification of these responder or progressor associated gene expressions and tumor properties can have clinical application in disease prognosis and treatment assignment.

In Chapter 4 we dived into the diversity of tumor-infiltrating T cells through the lens of single cell sequencing technologies. In addition to the exhausted T cell state reported in previous studies, we identified a novel CD69+JUN+HSPA1A+ early activated T cell state in both CD4+ and CD8+ T cell compartments, as well as a previously undescribed MALAT1+NEAT1+HNRNPH1+ exhausted T cell state as the terminal state in the differentiation trajectory of CD8+ tumor infiltrating T cells. Furthermore, we established high CD4+ and CD8+ naive T cell abundance pre-treatment as survival predictors, and demonstrated that naive T cell abundance

increased with treatment. By separating the “exhausted” T cells into more detailed cell states, we can potentially manipulate T cell differentiation *in vivo* into states that are associated with favorable prognosis or, re-create desirable cell states *in vitro* for cell therapies [80].

In Chapter 5, we described a previously unrecognized LAMP3+CCR7+BIRC3+CCL19+ cDC3 dendritic cell state as a powerful predictor of survival, and comprehensively characterized the cDC3 state, including its differentiation trajectory, transcriptome signatures, and epigenome landscape. Through both scRNA-seq regulatory network inference and snATAC-seq motif enrichment, we identified Rel/NF- κ B transcription factors family as a master regulator of the cDC3 transcriptome. Finally, relating to our findings in tumor infiltrating T cells, we identified potential cDC3-T cell interactions involved in T cell homing (e.g. CCL19-CCR7, CCL19-CXCR4) and activation (e.g. CD70-CD27). Overall, our findings suggest cDC3 as a key anti-tumor mediator that bridges the innate and adaptive immunity in metastatic melanoma.

6.2 Future directions

In this thesis, we conducted an in-depth study on the effects of ICIs in the immune compartment of the tumor microenvironment. While we have computationally arrived at many significant findings, we are actively planning validation experiments using additional clinical tumor tissues and mouse models. Specifically, we propose to perform immunohistochemistry staining for the novel T cell and DC states in tumor tissues to confirm their presence, explore their spatial organization, and identify their potential interactions with other cell types. In the meantime, we are also collaborating with other research institutes to computationally verify our findings in larger independent melanoma cohorts.

While we have investigated the immune cells in the tumor microenvironment, we have conducted relatively little investigation into the roles of stromal and malignant cells in determining the tumor-level response. Recent studies have reported that ICI treatment may affect tumor vasculature, and particularly the high endothelial venule

cells (HEVs) that facilitate T cells in entering tumor sites [116]. Using the scRNA-seq dataset presented in this thesis, we propose to conduct an extensive study on HEVs and their interaction with T cells and DCs in response to treatments. Finally, to investigate the contribution of the malignant cells themselves in shaping the tumor microenvironment and cDC3 abundance in particular, we propose to characterize the malignancies by their key mutations, copy number variations, and neoantigen loads. Incorporation of immune, stromal, and malignant characteristics would allow us to see the full picture of ICI actions and observe their interplay in the tumor microenvironment.

6.3 Concluding words

Immune checkpoint inhibitors are a vital and promising tool in the battle against cancer, despite response rates that are still unsatisfactory. In an attempt to improve ICI response, we have identified several molecular and cellular mediators as potential biomarkers to predict ICI treatment outcome. The identified mediators may also serve as candidates for new therapeutic targets in combination with existing ICIs to improve the therapeutic efficacy or benefit patients who do not respond to the current treatment regimens. Furthermore, we have highlighted the role of both the innate and the adaptive immune system in the anti-tumor immune response. In particular, our findings regarding the cDC3 dendritic cell subset as a key anti-tumor mediator emphasise the importance of crosstalk between innate and adaptive immunity in ICI-treated metastatic melanoma. Finally, as many of the immune mediators we have highlighted have previously been linked to ICI response in other cancer types, we hope that the findings in this thesis could be more broadly applicable.

Appendix A

Supplementary figures

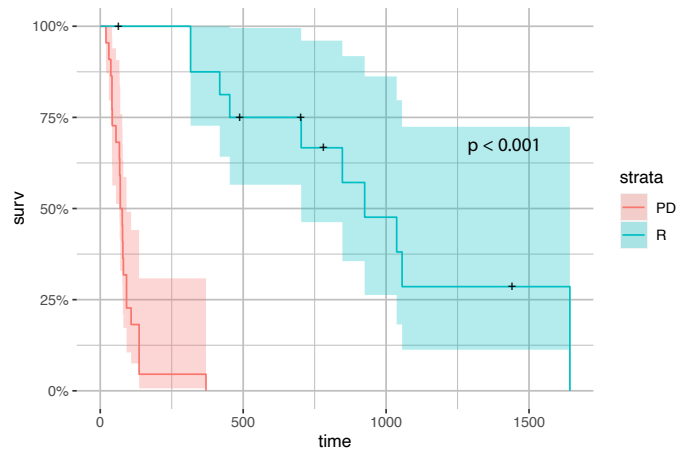


Figure A-1: Survival plot of response groups. Willcoxon test.



Figure A-2: Quality control of 39 RNA-seq samples. A. Principal component analysis comparing prospective (n = 20) and retrospective collections (n = 19). B. Principal component analysis comparing R (n = 22) and PD groups (n = 17). C. Boxplot of log₂(counts per million reads). Samples colored by response group.

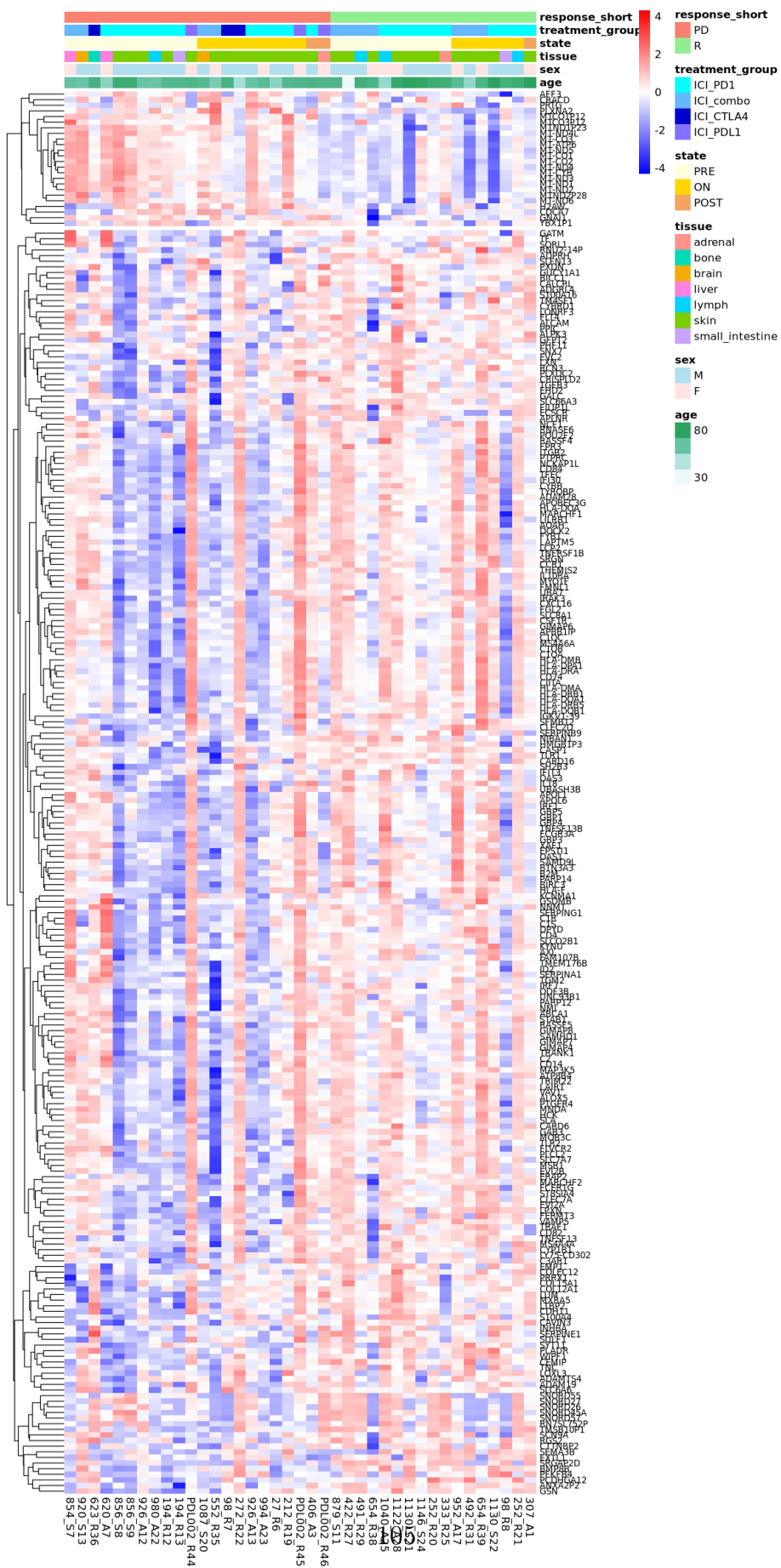


Figure A-3:

Figure A-3: Heatmap of differentially expressed genes between ICIs treated PD and R samples. Color reflects normalized expression level in each sample.

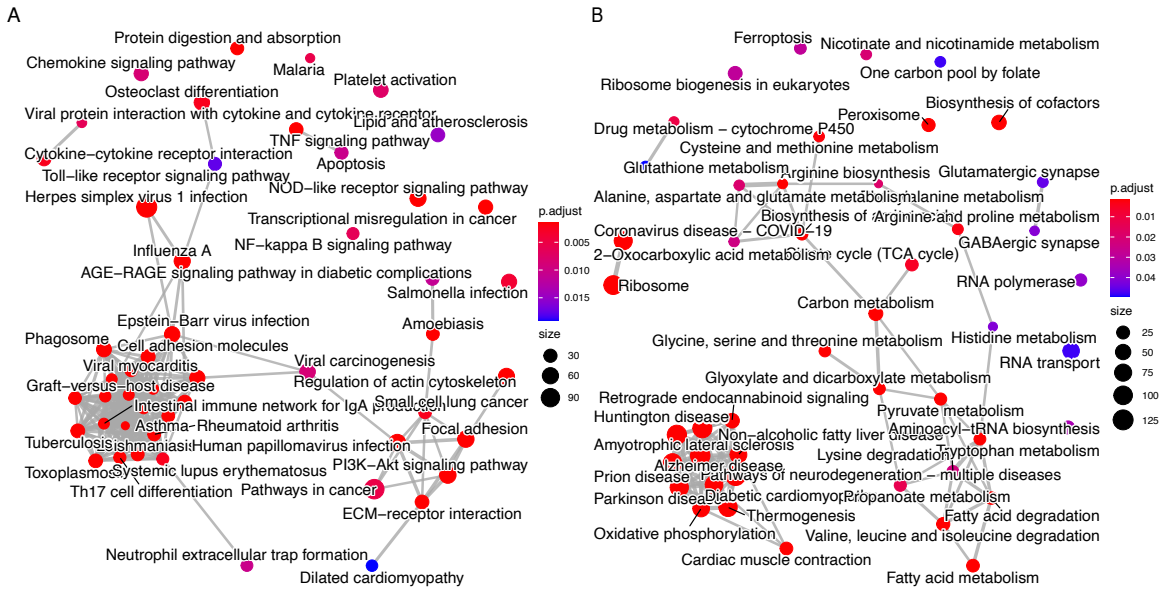


Figure A-5: Enrichment map of differentially expressed functional modules between pre-anti-PD-1 treated PD and R samples. A. Enrichment map showing functional modules enriched in R. Adjusted $p < 0.02$. B. Enrichment plot showing functional modules enriched in PD. Adjusted $p < 0.05$. Size indicates the number of leading edge genes. Color reflects adjusted p .

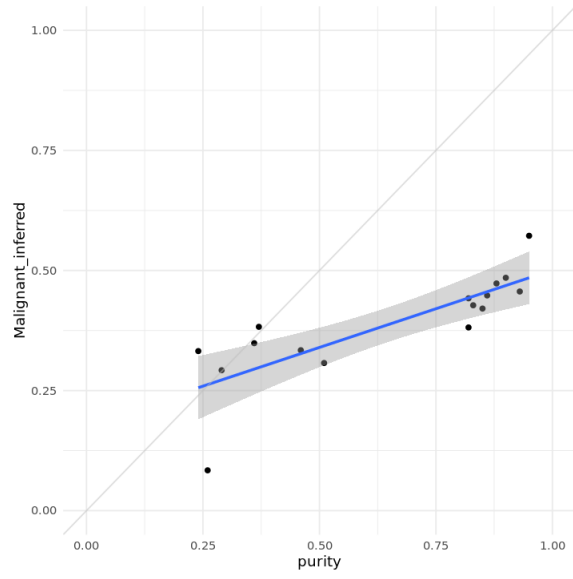


Figure A-6: Linear regression of tumor purity measured by whole exome sequencing (WES) and deconvolved malignant cell fraction in RNA-seq.

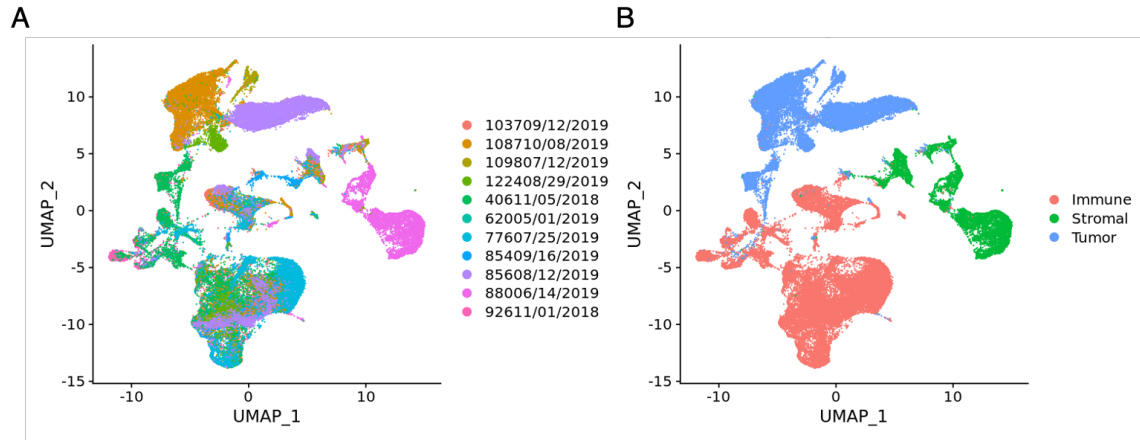


Figure A-7: Integration of 11 scRNA-seq samples. A. UMAP plot shows the sample origin. B. UMAP plot shows the assigned tumor compartment. 64,362 cells included.

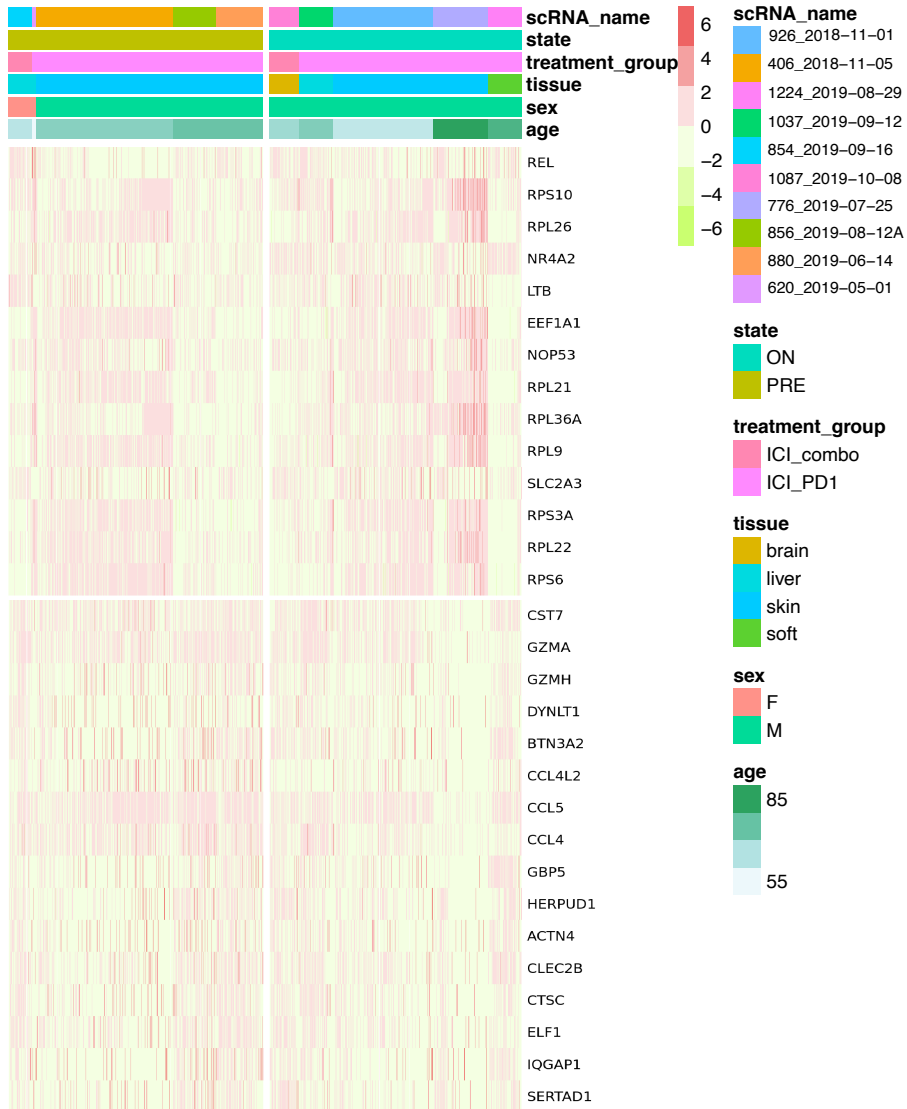


Figure A-8: Heatmap of differentially expressed genes in pre- and on-ICIs CD8+ T cells. Color reflects normalized expression level in each cell.

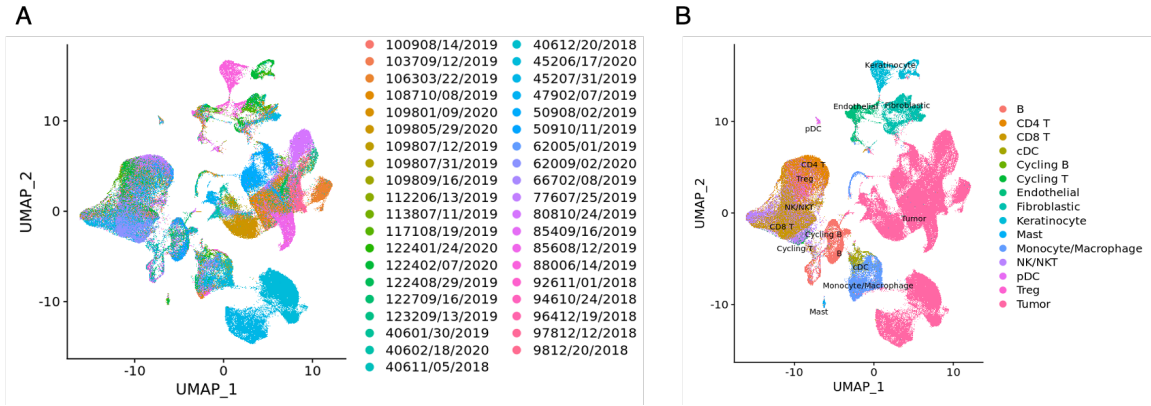


Figure A-9: Integration of 39 scRNA-seq samples. A. UMAP plot shows the sample origin. B. UMAP plot shows the assigned cell types. 222,351 cells included.

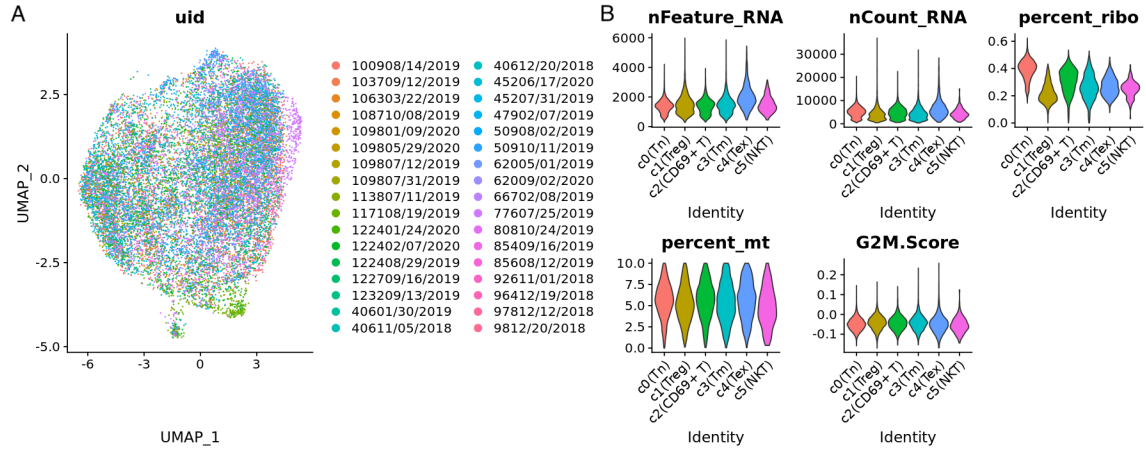


Figure A-10: Integration of CD4⁺ T cells from 34 scRNA-seq samples. A. UMAP plot shows the sample origin. B. Violin plots show the quality control metrics of each subpopulation. 17,952 cells included. nFeature_RNA, number of genes expressed; nCount_RNA, RNA read count, percent_ribo, percentage of reads aligned to ribosomal genes; percent_mt, percentage of reads aligned to mitochondrial genes; G2M.score, cell cycle G2/M phase activity score.

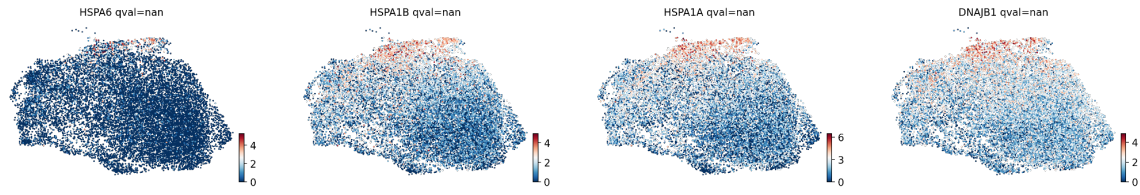


Figure A-12: UMAP feature plot of selected fate-driving genes of CD4+ T cell terminal state 2 inferred by *CytoTrace*. Benjamini Hochberg adjusted Spearman correlation p values. Color reflects normalized expression levels.

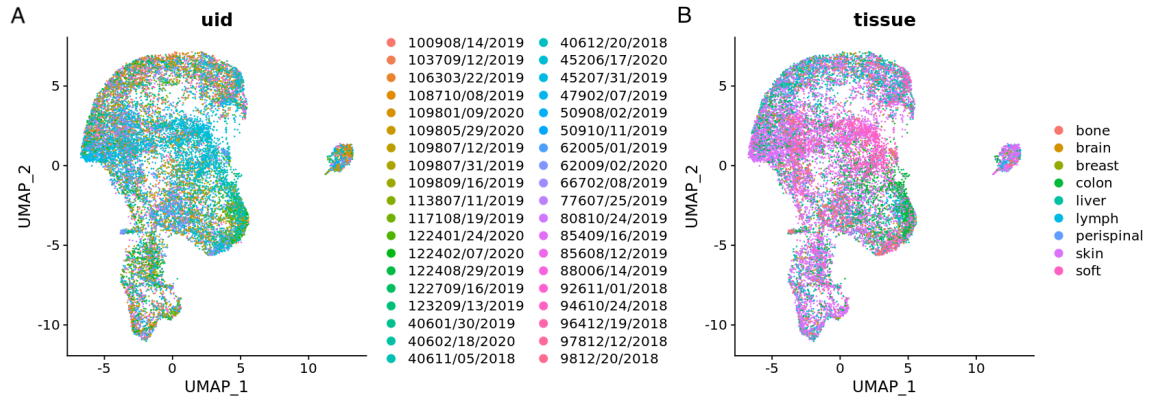


Figure A-15: Integration of myeloid cells from 39 scRNA-seq samples. A. UMAP plot shows the myeloid sample origin. B. UMAP plot shows the myeloid tissue origin.

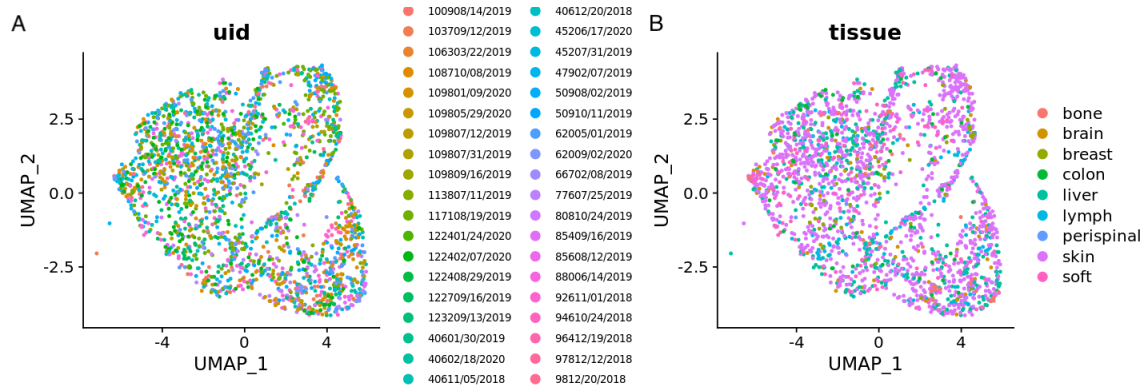


Figure A-16: Integration of cDCs from 38 scRNA-seq samples. A. UMAP plot shows the cDC sample origin. A. UMAP plot shows the cDC tissue origin. 2160 cells included.

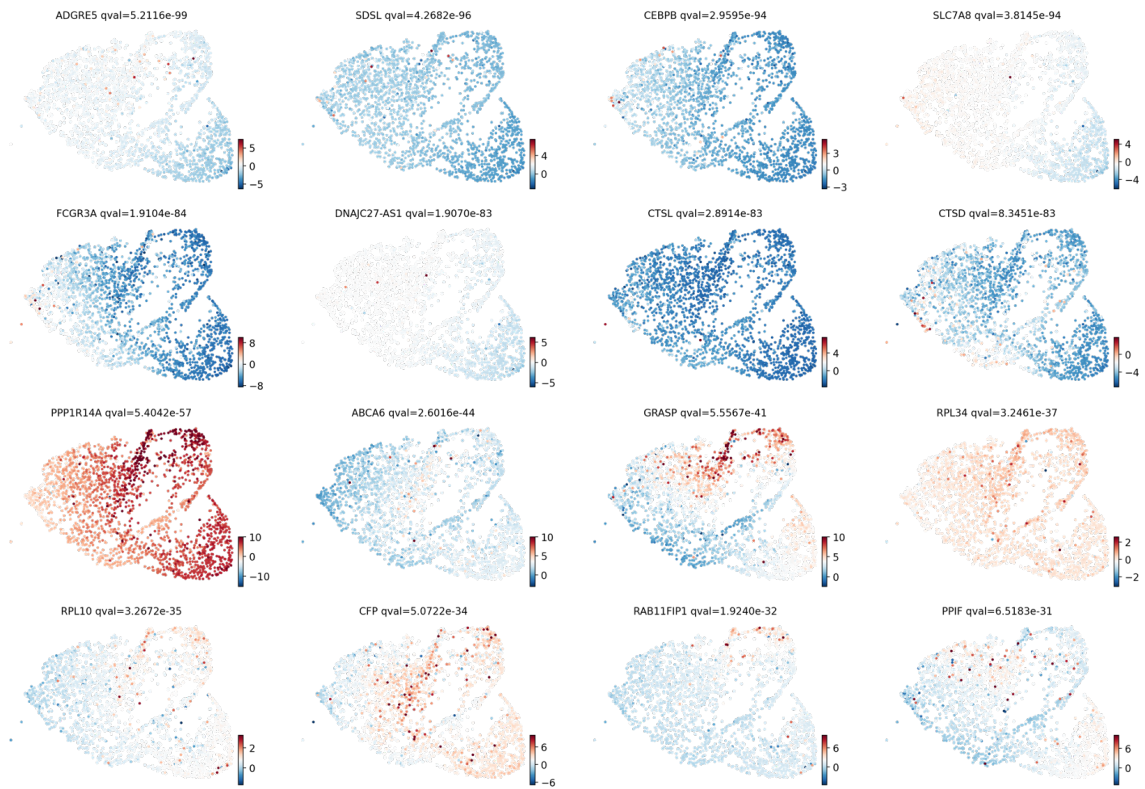


Figure A-17: UMAP feature plot of selected cDC3-fate driver genes inferred by *CytoTrace*. Benjamini Hochberg adjusted Spearman correlation p values. Color reflects the normalized expression levels.

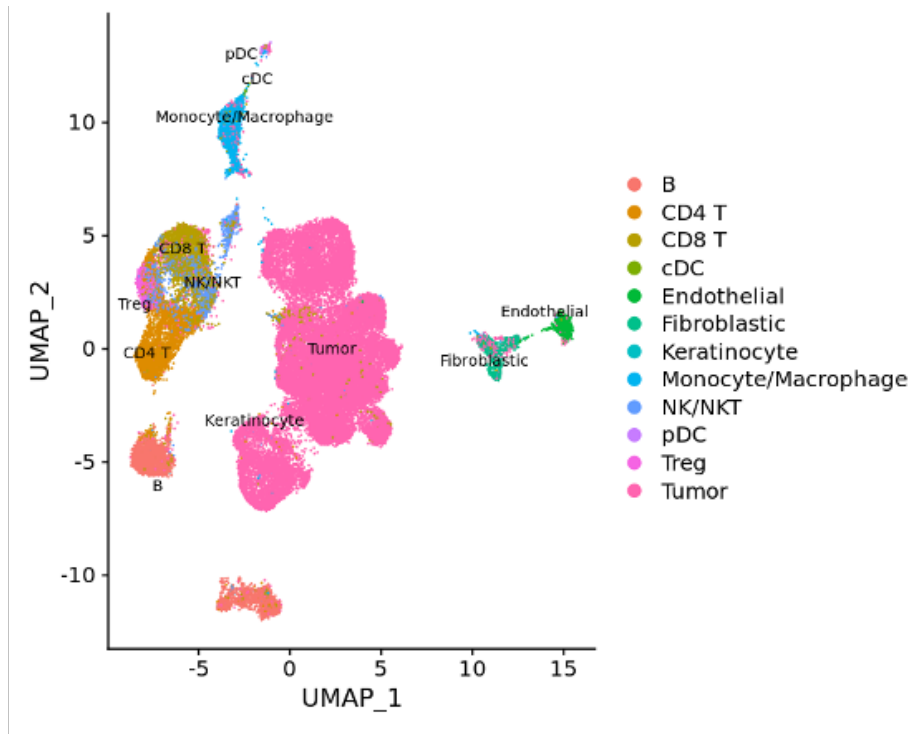


Figure A-18: Assignment of cell types in snATAC-seq dataset. UMAP plot includes 45,478 cells sequenced among 12 cell types.

Bibliography

- [1] “Melanoma targeted therapy: Targeted drugs for melanoma.,” April 2022 [online].
- [2] B. Switzer, I. Puzanov, J. J. Skitzki, L. Hamad, and M. S. Ernstoff, “Managing metastatic melanoma in 2022: A clinical review,” *JCO Oncology Practice*, pp. OP–21, 2022.
- [3] J.-D. Fumet, C. Truntzer, M. Yarchoan, and F. Ghiringhelli, “Tumour mutational burden as a biomarker for immunotherapy: Current data and emerging concepts,” *European Journal of Cancer*, vol. 131, pp. 40–50, 2020.
- [4] N. Riaz, J. J. Havel, V. Makarov, A. Desrichard, W. J. Urba, J. S. Sims, F. S. Hodi, S. Martín-Algarra, R. Mandal, W. H. Sharfman, S. Bhatia, W.-J. Hwu, T. F. Gajewski, C. L. Slingluff, D. Chowell, S. M. Kendall, H. Chang, R. Shah, F. Kuo, L. G. Morris, J.-W. Sidhom, J. P. Schneck, C. E. Horak, N. Weinhold, and T. A. Chan, “Tumor and microenvironment evolution during immunotherapy with nivolumab,” *Cell*, vol. 171, no. 4, pp. 934–949.e16, 2017.
- [5] “Melanoma skin cancer statistics,” April 2022 [online].
- [6] D. Kuk, A. N. Shoushtari, C. A. Barker, K. S. Panageas, R. R. Munhoz, P. Momtaz, C. E. Ariyan, M. S. Brady, D. G. Coit, K. Bogatch, M. K. Callahan, J. D. Wolchok, R. D. Carvajal, and M. A. Postow, “Prognosis of Mucosal, Uveal, Acral, Nonacral Cutaneous, and Unknown Primary Melanoma From the Time of First Metastasis,” *The Oncologist*, vol. 21, pp. 848–854, 06 2016.
- [7] D. Hanahan and R. A. Weinberg, “Hallmarks of cancer: the next generation,” *cell*, vol. 144, no. 5, pp. 646–674, 2011.
- [8] R. Dummer, P. A. Ascierto, P. Nathan, C. Robert, and D. Schadendorf, “Rationale for immune checkpoint inhibitors plus targeted therapy in metastatic melanoma: a review,” *JAMA oncology*, vol. 6, no. 12, pp. 1957–1966, 2020.
- [9] R. Baghban, L. Roshangar, R. Jahanban-Esfahlan, K. Seidi, A. Ebrahimi-Kalan, M. Jaymand, S. Kolahian, T. Javaheri, and P. Zare, “Tumor microenvironment complexity and therapeutic implications at a glance,” *Cell Communication and Signaling*, vol. 18, no. 1, pp. 1–19, 2020.

- [10] D. Hanahan, “Hallmarks of cancer: New dimensions,” *Cancer Discovery*, vol. 12, no. 1, pp. 31–46, 2022.
- [11] S. Venkatesan, C. Swanton, B. S. Taylor, and J. F. Costello, “Treatment-induced mutagenesis and selective pressures sculpt cancer evolution,” *Cold Spring Harbor perspectives in medicine*, vol. 7, no. 8, p. a026617, 2017.
- [12] A. J. Friedenstein, R. K. Chailakhyan, N. V. Latsinik, A. F. Panasyuk, and I. V. Keiliss-Borok, “Stromal cells responsible for transferring the microenvironment of the hemopoietic tissues: cloning in vitro and retransplantation in vivo,” *Transplantation*, vol. 17, no. 4, pp. 331–340, 1974.
- [13] L. Monteran and N. Erez, “The dark side of fibroblasts: cancer-associated fibroblasts as mediators of immunosuppression in the tumor microenvironment,” *Frontiers in immunology*, p. 1835, 2019.
- [14] H. Gonzalez, C. Hagerling, and Z. Werb, “Roles of the immune system in cancer: from tumor initiation to metastatic progression,” *Genes & development*, vol. 32, no. 19-20, pp. 1267–1284, 2018.
- [15] B. Maier, A. M. Leader, S. T. Chen, N. Tung, C. Chang, J. LeBerichel, A. Chudnovskiy, S. Maskey, L. Walker, J. P. Finnigan, *et al.*, “A conserved dendritic-cell regulatory program limits antitumour immunity,” *Nature*, vol. 580, no. 7802, pp. 257–262, 2020.
- [16] D. Sichien, B. Lambrecht, M. Guilliams, and C. Scott, “Development of conventional dendritic cells: from common bone marrow progenitors to multiple subsets in peripheral tissues,” *Mucosal immunology*, vol. 10, no. 4, pp. 831–844, 2017.
- [17] D. S. Chen and I. Mellman, “Oncology meets immunology: the cancer-immunity cycle,” *immunity*, vol. 39, no. 1, pp. 1–10, 2013.
- [18] K. Murphy and C. Weaver, *Janeway’s immunobiology*. Garland science, 2016.
- [19] T. Davoli, H. Uno, E. C. Wooten, and S. J. Elledge, “Tumor aneuploidy correlates with markers of immune evasion and with reduced response to immunotherapy,” *Science*, vol. 355, no. 6322, p. eaaf8399, 2017.
- [20] B. Nogrady, “Game-changing class of immunotherapy drugs lengthens melanoma survival rates,” *Nature*, vol. 580, no. 7804, pp. S14–S14, 2020.
- [21] “Fda approves opdualag for unresectable or metastatic melanoma.,” April 2022 [online].
- [22] W. H. Ward and J. M. Farma, “Cutaneous melanoma: etiology and therapy [internet],” 2017.

- [23] M. S. Carlino, J. Larkin, and G. V. Long, “Immune checkpoint inhibitors in melanoma,” *The Lancet*, vol. 398, no. 10304, pp. 1002–1014, 2021.
- [24] H. Ledford, H. Else, and M. Warren, “Cancer immunologists scoop medicine nobel prize,” *Nature*, vol. 562, no. 7725, pp. 20–22, 2018.
- [25] V. Petrova, I. Arkhypov, R. Weber, C. Groth, P. Altevogt, J. Utikal, and V. Umansky, “Modern aspects of immunotherapy with checkpoint inhibitors in melanoma,” *International Journal of Molecular Sciences*, vol. 21, no. 7, p. 2367, 2020.
- [26] R. K. Vaddepally, P. Kharel, R. Pandey, R. Garje, and A. B. Chandra, “Review of indications of fda-approved immune checkpoint inhibitors per nccn guidelines with the level of evidence,” *Cancers*, vol. 12, no. 3, p. 738, 2020.
- [27] J. D. Wolchok, V. Chiarion-Sileni, R. Gonzalez, P. Rutkowski, J.-J. Grob, C. L. Cowey, C. D. Lao, J. Wagstaff, D. Schadendorf, P. F. Ferrucci, *et al.*, “Overall survival with combined nivolumab and ipilimumab in advanced melanoma,” *New England Journal of Medicine*, vol. 377, no. 14, pp. 1345–1356, 2017.
- [28] Z. N. Willmore, R. J. Harris, S. Crescioli, K. Hussein, H. Kakkassery, D. Thapa, A. Cheung, J. Chauhan, H. J. Bax, A. Chenoweth, *et al.*, “B cells in patients with melanoma: implications for treatment with checkpoint inhibitor antibodies,” *Frontiers in Immunology*, p. 3560, 2021.
- [29] B. Domingues, J. M. Lopes, P. Soares, and H. Pópulo, “Melanoma treatment in review,” *ImmunoTargets and therapy*, vol. 7, p. 35, 2018.
- [30] B. Simon and U. Uslu, “Car-t cell therapy in melanoma: A future success story?,” *Experimental dermatology*, vol. 27, no. 12, pp. 1315–1321, 2018.
- [31] L. Zheng, S. Qin, W. Si, A. Wang, B. Xing, R. Gao, X. Ren, L. Wang, X. Wu, J. Zhang, *et al.*, “Pan-cancer single-cell landscape of tumor-infiltrating t cells,” *Science*, vol. 374, no. 6574, p. abe6474, 2021.
- [32] Y. L. Qiu, H. Zheng, A. Devos, H. Selby, and O. Gevaert, “A meta-learning approach for genomic survival analysis,” *Nature communications*, vol. 11, no. 1, pp. 1–11, 2020.
- [33] K. Litchfield, J. L. Reading, C. Puttick, K. Thakkar, C. Abbosh, R. Bentham, T. B. Watkins, R. Rosenthal, D. Biswas, A. Rowan, *et al.*, “Meta-analysis of tumor-and t cell-intrinsic mechanisms of sensitization to checkpoint inhibition,” *Cell*, vol. 184, no. 3, pp. 596–614, 2021.
- [34] M. Hong, S. Tao, L. Zhang, L.-T. Diao, X. Huang, S. Huang, S.-J. Xie, Z.-D. Xiao, and H. Zhang, “Rna sequencing: new technologies and applications in cancer research,” *Journal of hematology & oncology*, vol. 13, no. 1, pp. 1–16, 2020.

- [35] J. Lee, D. Hwang, *et al.*, “Single-cell multiomics: technologies and data analysis methods,” *Experimental & Molecular Medicine*, vol. 52, no. 9, pp. 1428–1442, 2020.
- [36] I. Tirosh, B. Izar, S. M. Prakadan, M. H. Wadsworth, D. Treacy, J. J. Trombetta, A. Rotem, C. Rodman, C. Lian, G. Murphy, *et al.*, “Dissecting the multicellular ecosystem of metastatic melanoma by single-cell rna-seq,” *Science*, vol. 352, no. 6282, pp. 189–196, 2016.
- [37] J. Wouters, Z. Kalender-Atak, L. Minnoye, K. I. Spanier, M. De Waegeneer, C. Bravo González-Blas, D. Mauduit, K. Davie, G. Hulselmans, A. Najem, *et al.*, “Robust gene expression programs underlie recurrent cell states and phenotype switching in melanoma,” *Nature Cell Biology*, vol. 22, no. 8, pp. 986–998, 2020.
- [38] L. Jerby-Arnon, P. Shah, M. S. Cuoco, C. Rodman, M.-J. Su, J. C. Melms, R. Leeson, A. Kanodia, S. Mei, J.-R. Lin, *et al.*, “A cancer cell program promotes t cell exclusion and resistance to checkpoint blockade,” *Cell*, vol. 175, no. 4, pp. 984–997, 2018.
- [39] R. Fang, S. Preissl, Y. Li, X. Hou, J. Lucero, X. Wang, A. Motamedi, A. K. Shiau, X. Zhou, F. Xie, *et al.*, “Comprehensive analysis of single cell atac-seq data with snapatac,” *Nature communications*, vol. 12, no. 1, pp. 1–15, 2021.
- [40] R. Leylek, M. Alcántara-Hernández, J. M. Granja, M. Chavez, K. Perez, O. R. Diaz, R. Li, A. T. Satpathy, H. Y. Chang, and J. Idoyaga, “Chromatin landscape underpinning human dendritic cell heterogeneity,” *Cell reports*, vol. 32, no. 12, p. 108180, 2020.
- [41] M. W. Fiers, L. Minnoye, S. Aibar, C. Bravo González-Blas, Z. Kalender Atak, and S. Aerts, “Mapping gene regulatory networks from single-cell omics data,” *Briefings in functional genomics*, vol. 17, no. 4, pp. 246–254, 2018.
- [42] D. Liu, B. Schilling, D. Liu, A. Sucker, E. Livingstone, L. Jerby-Arnon, L. Zimmer, R. Gutzmer, I. Satzger, C. Loquai, *et al.*, “Integrative molecular and clinical modeling of clinical outcomes to pd1 blockade in patients with metastatic melanoma,” *Nature medicine*, vol. 25, no. 12, pp. 1916–1927, 2019.
- [43] J. J. Havel, D. Chowell, and T. A. Chan, “The evolving landscape of biomarkers for checkpoint inhibitor immunotherapy,” *Nature Reviews Cancer*, vol. 19, no. 3, pp. 133–150, 2019.
- [44] S. Sun, L. Xu, X. Zhang, L. Pang, Z. Long, C. Deng, J. Zhu, S. Zhou, L. Wan, B. Pang, *et al.*, “Systematic assessment of transcriptomic biomarkers for immune checkpoint blockade response in cancer immunotherapy,” *Cancers*, vol. 13, no. 7, p. 1639, 2021.

- [45] M. I. Love, W. Huber, and S. Anders, “Moderated estimation of fold change and dispersion for rna-seq data with deseq2,” *Genome biology*, vol. 15, no. 12, pp. 1–21, 2014.
- [46] M. D. Robinson, D. J. McCarthy, and G. K. Smyth, “edger: a bioconductor package for differential expression analysis of digital gene expression data,” *Bioinformatics*, vol. 26, no. 1, pp. 139–140, 2010.
- [47] C. W. Law, Y. Chen, W. Shi, and G. K. Smyth, “voom: Precision weights unlock linear model analysis tools for rna-seq read counts,” *Genome biology*, vol. 15, no. 2, pp. 1–17, 2014.
- [48] A. Subramanian, P. Tamayo, V. K. Mootha, S. Mukherjee, B. L. Ebert, M. A. Gillette, A. Paulovich, S. L. Pomeroy, T. R. Golub, E. S. Lander, *et al.*, “Gene set enrichment analysis: a knowledge-based approach for interpreting genome-wide expression profiles,” *Proceedings of the National Academy of Sciences*, vol. 102, no. 43, pp. 15545–15550, 2005.
- [49] A. M. Newman, C. B. Steen, C. L. Liu, A. J. Gentles, A. A. Chaudhuri, F. Scherer, M. S. Khodadoust, M. S. Esfahani, B. A. Luca, D. Steiner, *et al.*, “Determining cell type abundance and expression from bulk tissues with digital cytometry,” *Nature biotechnology*, vol. 37, no. 7, pp. 773–782, 2019.
- [50] P. Therasse, E. Eisenhauer, and J. Verweij, “Recist revisited: a review of validation studies on tumour assessment,” *European journal of cancer*, vol. 42, no. 8, pp. 1031–1039, 2006.
- [51] L. A. Corchete, E. A. Rojas, D. Alonso-López, J. De Las Rivas, N. C. Gutiérrez, and F. J. Burguillo, “Systematic comparison and assessment of rna-seq procedures for gene expression quantitative analysis,” *Scientific reports*, vol. 10, no. 1, pp. 1–15, 2020.
- [52] L. Lefevre, H. Omeiri, L. Drougat, C. Hantel, M. Giraud, P. Val, S. Rodriguez, K. Perlemoine, C. Blugeon, F. Beuschlein, *et al.*, “Combined transcriptome studies identify aff3 as a mediator of the oncogenic effects of β -catenin in adrenocortical carcinoma,” *Oncogenesis*, vol. 4, no. 7, pp. e161–e161, 2015.
- [53] R. C. Osthus, B. Karim, J. E. Prescott, B. D. Smith, M. McDevitt, D. L. Huso, and C. V. Dang, “The myc target gene jpo1/cdca7 is frequently overexpressed in human tumors and has limited transforming activity in vivo,” *Cancer research*, vol. 65, no. 13, pp. 5620–5627, 2005.
- [54] P. R. Kumar, J. A. Moore, K. M. Bowles, S. A. Rushworth, and M. D. Moncrieff, “Mitochondrial oxidative phosphorylation in cutaneous melanoma,” *British Journal of Cancer*, vol. 124, no. 1, pp. 115–123, 2021.
- [55] J. L. McQuade and Y. Vashisht Gopal, “Counteracting oxidative phosphorylation-mediated resistance of melanomas to mapk pathway inhibition,” *Molecular & cellular oncology*, vol. 2, no. 3, p. e991610, 2015.

- [56] I. G. House, P. Savas, J. Lai, A. X. Chen, A. J. Oliver, Z. L. Teo, K. L. Todd, M. A. Henderson, L. Giuffrida, E. V. Petley, *et al.*, “Macrophage-derived cxcl9 and cxcl10 are required for antitumor immune responses following immune checkpoint blockade,” *Clinical Cancer Research*, vol. 26, no. 2, pp. 487–504, 2020.
- [57] P. M. Marcovecchio, G. Thomas, and S. Salek-Ardakani, “Cxcl9-expressing tumor-associated macrophages: new players in the fight against cancer,” *Journal for Immunotherapy of Cancer*, vol. 9, no. 2, 2021.
- [58] T. Zhou, W. Damsky, O.-E. Weizman, M. K. McGeary, K. P. Hartmann, C. E. Rosen, S. Fischer, R. Jackson, R. A. Flavell, J. Wang, *et al.*, “Il-18bp is a secreted immune checkpoint and barrier to il-18 immunotherapy,” *Nature*, vol. 583, no. 7817, pp. 609–614, 2020.
- [59] J. Fourcade, Z. Sun, J.-M. Chauvin, M. Ka, D. Davar, O. Pagliano, H. Wang, S. Saada, C. Menna, R. Amin, *et al.*, “Cd226 opposes tigit to disrupt tregs in melanoma,” *JCI insight*, vol. 3, no. 14, 2018.
- [60] Z. Ge, M. P. Peppelenbosch, D. Sprengers, and J. Kwekkeboom, “Tigit, the next step towards successful combination immune checkpoint therapy in cancer,” *Frontiers in Immunology*, vol. 12, 2021.
- [61] L. V. Gressot, T. Doucette, Y. Yang, G. N. Fuller, G. Manyam, A. Rao, K. Latha, and G. Rao, “Analysis of the inhibitors of apoptosis identifies birc3 as a facilitator of malignant progression in glioma,” *Oncotarget*, vol. 8, no. 8, p. 12695, 2017.
- [62] E. Tausch and S. Stilgenbauer, “Birc3 mutations in chronic lymphocytic leukemia—uncommon and unfavorable,” *haematologica*, vol. 105, no. 2, p. 255, 2020.
- [63] Y.-C. Wang, X. Wang, J. Yu, F. Ma, Z. Li, Y. Zhou, S. Zeng, X. Ma, Y.-R. Li, A. Neal, *et al.*, “Targeting monoamine oxidase a-regulated tumor-associated macrophage polarization for cancer immunotherapy,” *Nature communications*, vol. 12, no. 1, pp. 1–17, 2021.
- [64] M. Opyrchal, “T-cell receptor (tcr) engineered cells and their transition to the clinic,” in *Gene and Cellular Immunotherapy for Cancer*, pp. 251–266, Springer, 2022.
- [65] Y. Zhang, G. Parmigiani, and W. E. Johnson, “Combat-seq: batch effect adjustment for rna-seq count data,” *NAR genomics and bioinformatics*, vol. 2, no. 3, p. lqaa078, 2020.
- [66] G. Korotkevich, V. Sukhov, N. Budin, B. Shpak, M. N. Artyomov, and A. Sergushichev, “Fast gene set enrichment analysis,” *BioRxiv*, p. 060012, 2021.

- [67] A. Liberzon, A. Subramanian, R. Pinchback, H. Thorvaldsdóttir, P. Tamayo, and J. P. Mesirov, “Molecular signatures database (msigdb) 3.0,” *Bioinformatics*, vol. 27, no. 12, pp. 1739–1740, 2011.
- [68] G. Yu, L.-G. Wang, Y. Han, and Q.-Y. He, “clusterprofiler: an r package for comparing biological themes among gene clusters,” *Omics: a journal of integrative biology*, vol. 16, no. 5, pp. 284–287, 2012.
- [69] M. Sade-Feldman, K. Yizhak, S. L. Bjorgaard, J. P. Ray, C. G. de Boer, R. W. Jenkins, D. J. Lieb, J. H. Chen, D. T. Frederick, M. Barzily-Rokni, *et al.*, “Defining t cell states associated with response to checkpoint immunotherapy in melanoma,” *Cell*, vol. 175, no. 4, pp. 998–1013, 2018.
- [70] A. J. Schoenfeld and M. D. Hellmann, “Acquired resistance to immune checkpoint inhibitors,” *Cancer cell*, vol. 37, no. 4, pp. 443–455, 2020.
- [71] M. W. Pickup, J. K. Mouw, and V. M. Weaver, “The extracellular matrix modulates the hallmarks of cancer,” *EMBO reports*, vol. 15, no. 12, pp. 1243–1253, 2014.
- [72] J. W. Squair, M. Gautier, C. Kathe, M. A. Anderson, N. D. James, T. H. Hutson, R. Hudelle, T. Qaiser, K. J. Matson, Q. Barraud, *et al.*, “Confronting false discoveries in single-cell differential expression,” *Nature communications*, vol. 12, no. 1, pp. 1–15, 2021.
- [73] L. He, J. Davila-Velderrain, T. S. Sumida, D. A. Hafler, M. Kellis, and A. M. Kulminski, “Nebula is a fast negative binomial mixed model for differential or co-expression analysis of large-scale multi-subject single-cell data,” *Communications biology*, vol. 4, no. 1, pp. 1–17, 2021.
- [74] K. Araki, M. Morita, A. G. Bederman, B. T. Konieczny, H. T. Kissick, N. Sonnenberg, and R. Ahmed, “Translation is actively regulated during the differentiation of cd8⁺ effector t cells,” *Nature immunology*, vol. 18, no. 9, pp. 1046–1057, 2017.
- [75] H.-I. Aksoylar, N. M. Tijaro-Ovalle, V. A. Boussiotis, and N. Patsoukis, “T cell metabolism in cancer immunotherapy,” *Immunometabolism*, vol. 2, no. 3, 2020.
- [76] C. Li, Y. P. Phoon, K. Karlinsey, Y. F. Tian, S. Thapaliya, A. Thongkum, L. Qu, A. J. Matz, M. Cameron, C. Cameron, *et al.*, “A high oxphos cd8 t cell subset is predictive of immunotherapy resistance in melanoma patients,” *Journal of Experimental Medicine*, vol. 219, no. 1, p. e20202084, 2021.
- [77] S. J. Fleming, J. C. Marioni, and M. Babadi, “Cellbender remove-background: a deep generative model for unsupervised removal of background noise from scrna-seq datasets,” *BioRxiv*, p. 791699, 2019.

- [78] Y. Hao, S. Hao, E. Andersen-Nissen, W. M. Mauck III, S. Zheng, A. Butler, M. J. Lee, A. J. Wilk, C. Darby, M. Zager, *et al.*, “Integrated analysis of multimodal single-cell data,” *Cell*, vol. 184, no. 13, pp. 3573–3587, 2021.
- [79] I. Korsunsky, N. Millard, J. Fan, K. Slowikowski, F. Zhang, K. Wei, Y. Baglaenko, M. Brenner, P.-r. Loh, and S. Raychaudhuri, “Fast, sensitive and accurate integration of single-cell data with harmony,” *Nature methods*, vol. 16, no. 12, pp. 1289–1296, 2019.
- [80] D. E. Wagner and A. M. Klein, “Lineage tracing meets single-cell omics: opportunities and challenges,” *Nature Reviews Genetics*, vol. 21, no. 7, pp. 410–427, 2020.
- [81] V. Bergen, R. A. Soldatov, P. V. Kharchenko, and F. J. Theis, “Rna velocity—current challenges and future perspectives,” *Molecular systems biology*, vol. 17, no. 8, p. e10282, 2021.
- [82] B. V. Kumar, T. J. Connors, and D. L. Farber, “Human t cell development, localization, and function throughout life,” *Immunity*, vol. 48, no. 2, pp. 202–213, 2018.
- [83] S. M. Kaech, E. J. Wherry, and R. Ahmed, “Effector and memory t-cell differentiation: implications for vaccine development,” *Nature Reviews Immunology*, vol. 2, no. 4, pp. 251–262, 2002.
- [84] W. Jiang, Y. He, W. He, G. Wu, X. Zhou, Q. Sheng, W. Zhong, Y. Lu, Y. Ding, Q. Lu, *et al.*, “Exhausted cd8+ t cells in the tumor immune microenvironment: new pathways to therapy,” *Frontiers in Immunology*, vol. 11, p. 3739, 2021.
- [85] D. Krijgsman, M. Hokland, and P. J. Kuppen, “The role of natural killer t cells in cancer—a phenotypical and functional approach,” *Frontiers in immunology*, vol. 9, p. 367, 2018.
- [86] G. S. Gulati, S. S. Sikandar, D. J. Wesche, A. Manjunath, A. Bharadwaj, M. J. Berger, F. Ilagan, A. H. Kuo, R. W. Hsieh, S. Cai, *et al.*, “Single-cell transcriptional diversity is a hallmark of developmental potential,” *Science*, vol. 367, no. 6476, pp. 405–411, 2020.
- [87] L. Deconinck, R. Cannoodt, W. Saelens, B. Deplancke, and Y. Saeys, “Recent advances in trajectory inference from single-cell omics data,” *Current Opinion in Systems Biology*, vol. 27, p. 100344, 2021.
- [88] P. Angerer, L. Haghverdi, M. Büttner, F. J. Theis, C. Marr, and F. Büttner, “destiny: diffusion maps for large-scale single-cell data in r,” *Bioinformatics*, vol. 32, no. 8, pp. 1241–1243, 2016.
- [89] C. Trapnell, D. Cacchiarelli, J. Grimsby, P. Pokharel, S. Li, M. Morse, N. J. Lennon, K. J. Livak, T. S. Mikkelsen, and J. L. Rinn, “Pseudo-temporal ordering

- of individual cells reveals dynamics and regulators of cell fate decisions,” *Nature biotechnology*, vol. 32, no. 4, p. 381, 2014.
- [90] M. Lange, V. Bergen, M. Klein, M. Setty, B. Reuter, M. Bakhti, H. Lickert, M. Ansari, J. Schniering, H. B. Schiller, *et al.*, “Cellrank for directed single-cell fate mapping,” *Nature methods*, pp. 1–12, 2022.
- [91] D. Cibrián and F. Sánchez-Madrid, “Cd69: from activation marker to metabolic gatekeeper,” *European journal of immunology*, vol. 47, no. 6, pp. 946–953, 2017.
- [92] Z. Albakova and Y. Mangasarova, “The hsp immune network in cancer,” *Frontiers in immunology*, p. 5162, 2021.
- [93] K.-H. Song, S. J. Oh, S. Kim, H. Cho, H.-J. Lee, J. S. Song, J.-Y. Chung, E. Cho, J. Lee, S. Jeon, *et al.*, “Hsp90a inhibition promotes anti-tumor immunity by reversing multi-modal resistance and stem-like property of immune-refractory tumors,” *Nature communications*, vol. 11, no. 1, pp. 1–16, 2020.
- [94] M. Kurachi, “Cd8+ t cell exhaustion,” in *Seminars in immunopathology*, vol. 41, pp. 327–337, Springer, 2019.
- [95] Z.-W. Hu, L. Chen, R.-Q. Ma, F.-Q. Wei, Y.-H. Wen, X.-L. Zeng, W. Sun, and W.-P. Wen, “Comprehensive analysis of ferritin subunits expression and positive correlations with tumor-associated macrophages and t regulatory cells infiltration in most solid tumors,” *Aging (Albany NY)*, vol. 13, no. 8, p. 11491, 2021.
- [96] Y. Zhou, Y. Zhu, Y. Xie, and X. Ma, “The role of long non-coding rnas in immunotherapy resistance,” *Frontiers in oncology*, vol. 9, p. 1292, 2019.
- [97] S. E. Marsh, A. J. Walker, T. Kamath, L. Dissing-Olesen, T. R. Hammond, T. Y. de Soysa, A. M. Young, S. Murphy, A. Abdulraouf, N. Nadaf, *et al.*, “Dissection of artifactual and confounding glial signatures by single-cell sequencing of mouse and human brain,” *Nature Neuroscience*, vol. 25, no. 3, pp. 306–316, 2022.
- [98] G. Gorin, M. Fang, T. Chari, and L. Pachter, “Rna velocity unraveled,” *bioRxiv*, 2022.
- [99] G. La Manno, R. Soldatov, A. Zeisel, E. Braun, H. Hochgerner, V. Petukhov, K. Lidschreiber, M. E. Kastrioti, P. Lönnerberg, A. Furlan, *et al.*, “Rna velocity of single cells,” *Nature*, vol. 560, no. 7719, pp. 494–498, 2018.
- [100] S. Cheng, Z. Li, R. Gao, B. Xing, Y. Gao, Y. Yang, S. Qin, L. Zhang, H. Ouyang, P. Du, *et al.*, “A pan-cancer single-cell transcriptional atlas of tumor infiltrating myeloid cells,” *Cell*, vol. 184, no. 3, pp. 792–809, 2021.

- [101] A. Ladányi, J. Kiss, B. Somlai, K. Gilde, Z. Fejős, A. Mohos, I. Gaudi, and J. Tímár, “Density of dc-lamp+ mature dendritic cells in combination with activated t lymphocytes infiltrating primary cutaneous melanoma is a strong independent prognostic factor,” *Cancer Immunology, Immunotherapy*, vol. 56, no. 9, pp. 1459–1469, 2007.
- [102] G. M. Gerhard, R. Bill, M. Messemaker, A. M. Klein, and M. J. Pittet, “Tumor-infiltrating dendritic cell states are conserved across solid human cancers,” *Journal of Experimental Medicine*, vol. 218, 12 2020. e20200264.
- [103] C. S. Garris, S. P. Arlauckas, R. H. Kohler, M. P. Trefny, S. Garren, C. Piot, C. Engblom, C. Pfirschke, M. Siwicki, J. Gungabeesoon, *et al.*, “Successful anti-pd-1 cancer immunotherapy requires t cell-dendritic cell crosstalk involving the cytokines ifn- γ and il-12,” *Immunity*, vol. 49, no. 6, pp. 1148–1161, 2018.
- [104] J. Korbecki, S. Grochans, I. Gutowska, K. Barczak, and I. Baranowska-Bosiacka, “Cc chemokines in a tumor: A review of pro-cancer and anti-cancer properties of receptors ccr5, ccr6, ccr7, ccr8, ccr9, and ccr10 ligands,” *International Journal of Molecular Sciences*, vol. 21, no. 20, 2020.
- [105] B. Weide, N. Allgaier, A. Hector, A. Forschner, U. Leiter, T. K. Eigentler, C. Garbe, and D. Hartl, “Increased ccl17 serum levels are associated with improved survival in advanced melanoma,” *Cancer Immunology, Immunotherapy*, vol. 64, no. 9, p. 1075–1082, 2015.
- [106] M. Neumann, H.-W. Fries, C. Scheicher, P. Keikavoussi, K.-M. A., B. E.-B., E. Serfling, and K. E., “Differential expression of rel/nf-kb and octamer factors is a hallmark of the generation and maturation of dendritic cells,” *Blood*, vol. 95, no. 1, p. 277–285, 2000.
- [107] A. E. Vilgelm and A. Richmond, “Chemokines modulate immune surveillance in tumorigenesis, metastasis, and response to immunotherapy,” *Frontiers in Immunology*, vol. 10, 2019.
- [108] X. Ou, H. A. O’Leary, and H. E. Broxmeyer, “Implications of dpp4 modification of proteins that regulate stem/progenitor and more mature cell types,” *Blood*, vol. 122, no. 2, p. 161–169, 2013.
- [109] K. van de Ven and J. Borst, “Targeting the t-cell co-stimulatory cd27/cd70 pathway in cancer immunotherapy: rationale and potential,” *Immunotherapy*, vol. 7, no. 6, pp. 655–667, 2015. PMID: 26098609.
- [110] Q. Zhou, Y. Zhang, B. Wang, W. Zhou, Y. Bi, W. Huai, X. Chen, Y. Chen, Z. Liu, X. Liu, *et al.*, “Kdm2b promotes il-6 production and inflammatory responses through brg1-mediated chromatin remodeling,” *Cellular & molecular immunology*, vol. 17, no. 8, pp. 834–842, 2020.

- [111] N. Zacharopoulou, A. Tsapara, G. Kallergi, E. Schmid, P. N. Tsihchlis, S. C. Kampranis, and C. Stournaras, “The epigenetic factor *kdm2b* regulates cell adhesion, small rho gtpases, actin cytoskeleton and migration in prostate cancer cells,” *Biochimica et Biophysica Acta (BBA)-Molecular Cell Research*, vol. 1865, no. 4, pp. 587–597, 2018.
- [112] M. Efremova, M. Vento-Tormo, S. A. Teichmann, and R. Vento-Tormo, “Cellphonedb: Inferring cell–cell communication from combined expression of multi-subunit ligand–receptor complexes,” *Nature Protocols*, vol. 15, no. 4, p. 1484–1506, 2020.
- [113] D. Dimitrov, C. Boys, D. Turei, J. N. S., R. R. F. O., H. Kim, B. Szalai, I. C. G., A. Dugourd, A. Valdeolivas, and J. Saez-Rodriguez, “Comparison of resources and methods to infer cell-cell communication from single-cell rna data,” *BioRxiv*, 2021.
- [114] S. Aibar, C. B. González-Blas, T. Moerman, V. A. Huynh-Thu, H. Imrichova, G. Hulselmans, F. Rambow, J.-C. Marine, P. Geurts, J. Aerts, J. van den Oord, Z. K. Atak, J. Wouters, and S. Aerts, “Scenic: single-cell regulatory network inference and clustering,” *Nature methods*, vol. 14, p. 1083–1086, November 2017.
- [115] S. Stuart and Madad, “Single-cell chromatin state analysis with signac,” *Nat Methods*, vol. 18, pp. 1333–1341, 2021.
- [116] A. Asrir, C. Tardiveau, J. Coudert, R. Laffont, L. Blanchard, E. Bellard, K. Veerman, S. Bettini, F. Lafouresse, E. Vina, D. Tarroux, S. Roy, I. Girault, I. Molinaro, F. Martins, J.-Y. Scoazec, N. Ortega, C. Robert, and J.-P. Girard, “Tumor-associated high endothelial venules mediate lymphocyte entry into tumors and predict response to pd-1 plus ctla-4 combination immunotherapy,” *Cancer Cell*, vol. 40, no. 3, pp. 318–334.e9, 2022.